

---

## Fatigue Analysis of Floating Offshore Wind Turbine Tower in Composite Material

**Auteur :** Al-Ghuwaidi, Abdulelah Abdullah Saleh

**Promoteur(s) :** Rigo, Philippe

**Faculté :** Faculté des Sciences appliquées

**Diplôme :** Master : ingénieur civil mécanicien, à finalité spécialisée en "Advanced Ship Design"

**Année académique :** 2022-2023

**URI/URL :** <http://hdl.handle.net/2268.2/19333>

---

*Avertissement à l'attention des usagers :*

*Tous les documents placés en accès ouvert sur le site le site MatheO sont protégés par le droit d'auteur. Conformément aux principes énoncés par la "Budapest Open Access Initiative"(BOAI, 2002), l'utilisateur du site peut lire, télécharger, copier, transmettre, imprimer, chercher ou faire un lien vers le texte intégral de ces documents, les disséquer pour les indexer, s'en servir de données pour un logiciel, ou s'en servir à toute autre fin légale (ou prévue par la réglementation relative au droit d'auteur). Toute utilisation du document à des fins commerciales est strictement interdite.*

*Par ailleurs, l'utilisateur s'engage à respecter les droits moraux de l'auteur, principalement le droit à l'intégrité de l'oeuvre et le droit de paternité et ce dans toute utilisation que l'utilisateur entreprend. Ainsi, à titre d'exemple, lorsqu'il reproduira un document par extrait ou dans son intégralité, l'utilisateur citera de manière complète les sources telles que mentionnées ci-dessus. Toute utilisation non explicitement autorisée ci-avant (telle que par exemple, la modification du document ou son résumé) nécessite l'autorisation préalable et expresse des auteurs ou de leurs ayants droit.*

---



POLITÉCNICA



Universität  
Rostock



Traditio et Innovatio



SOLENT  
UNIVERSITY  
SOUTHAMPTON



Zachodniopomorski  
Uniwersytet  
Techniczny  
w Szczecinie



With the support of the  
Erasmus+ Programme  
of the European Union



BUREAU  
VERITAS

# Fatigue Analysis of Floating Offshore Wind Turbine Tower in Composite Materials

submitted on 27 August, 2023

by

**AL-GHUWAIDI Abdulelah**

4 Rue Duguay Trouin | 44800 Saint-Herblain | Nantes | France

abdulelah.abdullah@alumnos.upm.es

Student ID No.: S213350

## First Reviewer:

Prof. Yordan Garbatov

IST

Av. Rovisco Pais 1

1049-001 Lisbon

Portugal

## Second Reviewer:

Dr. Andrés Pastor Sánchez

UPM

Av. de la Memoria, 4

28040 Madrid

Spain

[This page is intentionally left blank]

# Contents

List of Figures . . . . .	v
List of Tables . . . . .	viii
DECLARATION OF AUTHORSHIP . . . . .	xi
ACKNOWLEDGEMENTS . . . . .	xii
ABSTRACT . . . . .	xiii
<b>1 INTRODUCTION . . . . .</b>	<b>1</b>
1.1 Background . . . . .	1
1.2 Motivation . . . . .	3
1.3 Objective . . . . .	4
<b>2 METHODOLOGY . . . . .</b>	<b>6</b>
2.1 Geometry . . . . .	6
2.1.1 FOWT . . . . .	6
2.1.2 FRP Tower . . . . .	6
2.1.3 Platform . . . . .	7
2.2 Materials . . . . .	8
2.3 Hydrodynamic Response . . . . .	10
2.3.1 FOWT platform mesh . . . . .	11
2.3.2 Radiation and diffraction . . . . .	13
2.3.3 Motions . . . . .	13
2.3.4 2nd order loads . . . . .	15
2.3.5 Transfer functions . . . . .	15
2.4 FOWT Global Response . . . . .	16
2.4.1 Site . . . . .	16
2.4.2 Floater . . . . .	17
2.4.3 Mooring lines . . . . .	19
2.4.4 Turbine . . . . .	20
2.4.5 Environment . . . . .	21
2.4.6 Assembly . . . . .	25
2.4.7 Analysis . . . . .	26
2.5 Analytical Formulation . . . . .	28
2.5.1 Global loads . . . . .	28
2.5.2 Line loads . . . . .	29
2.5.3 Model validation . . . . .	34



2.6	Macro-mechanical Analysis . . . . .	39
2.6.1	Fibre and resin characteristics . . . . .	39
2.6.2	Ply definition . . . . .	40
2.6.3	Laminate characteristics and analysis . . . . .	40
2.6.4	Laminate behaviour under global and local loads . . . . .	42
2.6.5	Python tool validation . . . . .	45
2.7	Fatigue Analysis . . . . .	49
2.7.1	Fatigue damage analysis . . . . .	50
2.7.2	Fatigue tool validation . . . . .	57
<b>3</b>	<b>RESULTS AND DISCUSSION . . . . .</b>	<b>60</b>
3.1	Hydrodynamic Response . . . . .	60
3.1.1	Radiation . . . . .	60
3.1.2	Diffraction . . . . .	62
3.1.3	Motions . . . . .	64
3.1.4	2nd order loads . . . . .	65
3.2	FOWT Global Response . . . . .	66
3.2.1	Model verification . . . . .	66
3.2.2	Global internal loads . . . . .	69
3.3	Macro-Mechanical Analysis . . . . .	71
3.3.1	Line loads . . . . .	71
3.4	Fatigue Analysis . . . . .	75
3.4.1	Ply stresses . . . . .	75
3.4.2	S-N curve linear interpolation and CFL diagram . . . . .	76
3.4.3	Summary . . . . .	78
3.5	Static Analysis . . . . .	79
3.5.1	Static loads . . . . .	79
3.5.2	Safety factors . . . . .	80
3.5.3	Results . . . . .	81
3.6	Tower Deflection . . . . .	82
3.7	Buckling . . . . .	84
3.8	Modal Analysis . . . . .	85
3.9	Summary . . . . .	87
<b>4</b>	<b>Design Optimization . . . . .</b>	<b>88</b>
4.1	Static and Fatigue Optimization . . . . .	88
4.2	Tower Deflection . . . . .	93
4.3	Buckling . . . . .	94
4.4	Modal Analysis . . . . .	95
4.5	Summary . . . . .	96

<b>5 CONCLUSION</b> . . . . .	<b>97</b>
<b>References</b> . . . . .	<b>100</b>
<b>A Appendix A</b> . . . . .	<b>102</b>
A.1 Torsion line load . . . . .	102
A.2 Bending line load . . . . .	102
A.3 Shear line load . . . . .	103
<b>B Appendix B</b> . . . . .	<b>104</b>
B.1 Buckling Modes . . . . .	104
B.1.1 Reference laminate . . . . .	104
B.1.2 4th Optimized laminate . . . . .	105
<b>C Appendix C</b> . . . . .	<b>106</b>
C.1 Mode shapes (Eigenmodes) . . . . .	106
C.1.1 Reference laminate . . . . .	106
C.1.2 4th Optimized laminate . . . . .	108

---

## List of Figures

1.1	Types of FOWT foundations. . . . .	1
1.2	W2Power FOWT turbine by Enerocean. . . . .	2
1.3	Main pillars of FibreGY project. . . . .	4
1.4	General methodology of this thesis. . . . .	5
2.1	FOWT 3D CAD model. . . . .	6
2.2	FRP tower 3D model. . . . .	7
2.3	Floating platform 3D model for HydroStar. . . . .	7
2.4	Carbon FRP Tower layout. . . . .	9
2.5	FOWT Degrees of Freedom. . . . .	10
2.6	HydroStar flowchart. . . . .	11
2.7	Platform mesh in HydroStar based on the work of. . . . .	11
2.8	Platform mesh in HydroStar used in this thesis. . . . .	12
2.9	Platform mesh check in HydroStar. . . . .	12
2.10	Radiation and diffraction (Hsrdf) module input file in HydroStar. . . . .	13
2.11	Mechanical (Hsmcn) module input file in HydroStar. . . . .	14
2.12	Platform mesh in HydroStar with Morison elements. . . . .	14
2.13	QTF (Hsqtf) module input file in HydroStar. . . . .	15
2.14	Transfer functions (Hsrao) module input file in HydroStar. . . . .	15
2.15	Site definition in OPERA. . . . .	16
2.16	Floating platform mesh in FEMAP. . . . .	17
2.17	Floater definition in OPERA. . . . .	17
2.18	Morison elements definition in OPERA. . . . .	19
2.19	Mooring lines definition in OPERA. . . . .	19
2.20	Mooring radius in OPERA. . . . .	20
2.21	Turbine definition in OPERA. . . . .	21
2.22	Wind time-series velocity. . . . .	22
2.23	Wind time-series thrust. . . . .	23
2.24	Wind velocity and pressure on the FOWT exposed surfaces. . . . .	23
2.25	JONSWAP spectrum. . . . .	24
2.26	JONSWAP spectrum time-series. . . . .	25
2.27	Assembly of FOWT in OPERA. . . . .	25
2.28	Kinematic tree of FOWT Assembly in OPERA. . . . .	26
2.29	3D post-process in OPERA. . . . .	27
2.30	Cylindrical tube section. . . . .	28
2.31	Cylindrical tube reference system and global loads. . . . .	29
2.32	Solid circular section. . . . .	32
2.33	FEMAP model geometry. . . . .	35

2.34	FEMAP model mesh. . . . .	35
2.35	Loads and boundary conditions. . . . .	36
2.36	FEMAP Axial line load ( $\zeta_z$ ) due to $F_z$ . . . . .	36
2.37	Bending line loads. . . . .	37
2.38	FEMAP model geometry for shear line loads. . . . .	37
2.39	FEMAP model mesh for shear line loads. . . . .	38
2.40	Shear line loads. . . . .	38
2.41	Reference axis system of a unidirectional layer. . . . .	39
2.42	reference system of a single fibre. . . . .	39
2.43	Individual layers position. . . . .	41
2.44	Individual layers orientation to the laminate global axis. . . . .	41
2.45	Laminate under forces and moments. . . . .	43
2.46	Fatigue analysis flowchart. . . . .	50
2.47	Fatigue life evaluation using UD S-N curves. . . . .	51
2.48	Rainflow algorithm. . . . .	52
2.49	Different stress ratios (R). . . . .	54
2.50	CFL diagram for wind turbine applications. . . . .	55
2.51	Intermediate ratio linear interpolation. . . . .	55
2.52	Ply fibre and matrix stresses. . . . .	57
2.53	CFL tension-compression regions . . . . .	58
2.54	CFL matrix. . . . .	59
2.55	CFL fibre. . . . .	59
3.1	Added mass in translation DoF. . . . .	61
3.2	Added mass in rotational DoF. . . . .	61
3.3	Radiation damping in translation DoF. . . . .	62
3.4	Radiation damping in rotational DoF. . . . .	62
3.5	First-order forces in translation DoF. . . . .	63
3.6	First-order moments in translation DoF. . . . .	63
3.7	Translational motions (RAOs) . . . . .	65
3.8	Rotational motions (RAOs) . . . . .	65
3.9	Regular wave signal in OPERA. . . . .	66
3.10	Pitch response verification against regular waves. . . . .	67
3.11	Vertical pre-tension at fairlead in OPERA. . . . .	67
3.12	Axial and horizontal pre-tensions at fairlead in Ariane. . . . .	68
3.13	Fairlead offset in the x-direction . . . . .	68
3.14	Schematic of the horizontal and vertical stiffnesses at the fairlead. . . . .	69
3.15	Global Forces time-series at tower base section. . . . .	69
3.16	Global Moments time-series at tower base section. . . . .	70
3.17	My at various sections of the tower. . . . .	70

---

3.18	Global frame system and internal loads in OPERA. . . . .	71
3.19	$N_x$ line loads variation in different radius angles. . . . .	72
3.20	$\zeta_{M_x}$ and $\zeta_{M_y}$ line loads with respect to radius angle $\theta$ . . . . .	72
3.21	$\zeta_{F_x}$ and $\zeta_{F_y}$ line loads with respect to radius angle $\theta$ . . . . .	73
3.22	Laminate axis in the tower. . . . .	73
3.23	In-plane forces $N_x$ and $N_{xy}$ with respect to radius angle $\theta$ . . . . .	74
3.24	$N_x$ time-series at $161.25^\circ$ . . . . .	74
3.25	$N_x$ time-series at $341.25^\circ$ . . . . .	75
3.26	Ply stresses time-series at $90^\circ$ ply. . . . .	75
3.27	Fibre and matrix stress history of $90^\circ$ ply. . . . .	76
3.28	S-N diagram linear interpolation example for the matrix $90^\circ$ ply. . . . .	76
3.29	Matrix CFL diagram for $90^\circ$ ply. . . . .	77
3.30	Fibre CFL diagram for $90^\circ$ ply. . . . .	77
3.31	Selection method of static optimization global internal loads. . . . .	79
3.32	Selection method of in-plane forces for static analysis. . . . .	80
3.33	Tower setup (left) Element size 200 mm (right) Element size 20 mm. . . . .	82
3.34	Material orientation in FEMAP. . . . .	83
3.35	Tower deflection in FEMAP. . . . .	83
3.36	First buckling mode of the tower (element size: 20mm). . . . .	84
3.37	FRP tower mesh in FEMAP. . . . .	86
3.38	First mode shape the FRP tower in FEMAP. . . . .	86
4.1	$1^{st}$ buckling mode of the FRP tower with the $4^{th}$ optimized laminate. . . . .	94
4.2	$1^{st}$ mode shape of the FRP tower with the $4^{th}$ optimized laminate. . . . .	95

## List of Tables

1.1	Comparison between different FOWT foundations. . . . .	2
2.1	Elastic coefficients (MPa) & Breaking stresses (MPa) . . . . .	8
2.2	Laminate location across tower height. . . . .	8
2.3	Specifications of the normal wave condition used in OPERA. . . . .	24
2.4	Loads definition on the FOWT. . . . .	27
2.5	Cylindrical tube specifications. . . . .	34
2.6	Axial and torsion line loads. . . . .	36
2.7	Fibre and resin mechanical properties. . . . .	45
2.8	UD Layer Characteristics. . . . .	45
2.9	UD Elastic Coefficients (MPa). . . . .	46
2.10	UD Breaking Stresses (MPa). . . . .	46
2.11	Laminate definition. . . . .	46
2.12	Laminate global results. . . . .	47
2.13	Ply stresses at its local axis (MPa). . . . .	48
2.14	Slope coefficients ( $m$ ) used for interpolation. . . . .	58
3.1	Fatigue damage of several plies at the tower base ( $\theta = 341.25^\circ$ ). . . . .	78
3.2	Fatigue damage of several plies at the tower base ( $\theta = 161.25^\circ$ ). . . . .	78
3.3	Criteria of the tower base reference laminate under static load ( $\theta = 341.25^\circ$ ). . . . .	81
3.4	Criteria of the tower base reference laminate under static load ( $\theta = 161.25^\circ$ ). . . . .	82
3.5	Deflection criteria of the tower with different meshes. . . . .	84
3.6	Buckling load factors for both tower mesh. . . . .	85
3.7	Eigenvalues (natural frequencies) of the FRP tower. . . . .	87
4.1	Criteria of the tower base 1 <sup>st</sup> optimization under static load ( $\theta = 341.25^\circ$ ). . . . .	88
4.2	Fatigue damage at the tower base with 1 <sup>st</sup> optimization ( $\theta = 341.25^\circ$ ). . . . .	89
4.3	Criteria of the tower base 2 <sup>nd</sup> optimization under static load ( $\theta = 341.25^\circ$ ). . . . .	89
4.4	Fatigue damage at the tower base with 2 <sup>nd</sup> optimization ( $\theta = 341.25^\circ$ ). . . . .	89
4.5	Criteria of the tower base 3 <sup>rd</sup> optimization under static load ( $\theta = 341.25^\circ$ ). . . . .	90
4.6	Fatigue damage at the tower base with 3 <sup>rd</sup> optimization ( $\theta = 341.25^\circ$ ). . . . .	90
4.7	Criteria of the tower base 4 <sup>th</sup> optimization under static load ( $\theta = 341.25^\circ$ ). . . . .	90
4.8	Fatigue damage at the tower base with 4 <sup>th</sup> optimization ( $\theta = 341.25^\circ$ ). . . . .	91
4.9	Criteria of the tower base 5 <sup>th</sup> optimization under static load ( $\theta = 341.25^\circ$ ). . . . .	91
4.10	Fatigue damage at the tower base with 5 <sup>th</sup> optimization ( $\theta = 341.25^\circ$ ). . . . .	91
4.11	Criteria of the tower base 6 <sup>th</sup> optimization under static load ( $\theta = 341.25^\circ$ ). . . . .	92
4.12	Fatigue damage at the tower base with 6 <sup>th</sup> optimization ( $\theta = 341.25^\circ$ ). . . . .	92
4.13	Criteria of the tower base 5 <sup>th</sup> optimization under static load ( $\theta = 161.25^\circ$ ). . . . .	92
4.14	Fatigue damage at the tower base with 5 <sup>th</sup> optimization ( $\theta = 161.25^\circ$ ). . . . .	93
4.15	Thickness reduction for each optimization iteration. . . . .	93

4.16	Deflection criteria of the FRP tower with the 5 <sup>th</sup> optimized laminate. . . .	93
4.17	Deflection criteria of the FRP tower with the 4 <sup>th</sup> optimized laminate. . . .	94
4.18	Buckling load factors with the 4 <sup>th</sup> optimized laminate. . . . .	95
4.19	Comparison of eigenvalues of the FRP tower with two laminates. . . . .	96

## **Nomenclature**

BV	Bureau Veritas
CFL	Constant Fatigue Life
CoG	Centre of Gravity
CSM	Chopped Standard Mat
FEM	Finite Element Methods
FOWT	Floating Offshore Wind Turbine
FRP	Fibre Reinforced Polymer
GBS	Gravity Base Structures
IEC	International Electrotechnical Commission
JONSWAP	Joint North Sea Wave Project
MD	Multi-Directional
MRE	Marine Renewable Energy
OWT	Offshore Wind Turbine
QTF	Quadratic Transfer Function
RAO	Response Amplitude Operator
SF	Safety Factor
UD	Uni-Directional
WR	Woven Roving
WSD	Working Stress Design



[This page is intentionally left blank]

---

## DECLARATION OF AUTHORSHIP

I, **Abdulelah Al-Ghuwaidi** declare that this thesis and the work presented in it are my own and have been generated by me as the result of my own original research.

Where I have consulted the published work of others, this is always clearly attributed.

Where I have quoted from the work of others, the source is always given. With the exception of such quotations, this thesis is entirely my own work.

I have acknowledged all main sources of help.

Where the thesis is based on work done by myself jointly with others, I have made clear exactly what was done by others and what I have contributed myself.

This thesis contains no material that has been submitted previously, in whole or in part, for the award of any other academic degree or diploma.

I cede copyright of the thesis in favour of the Technical University of Madrid (UPM) and University of Liege (ULiege).

**Date:** August 27, 2023

**Signature:** *Abdulelah*

[This page is intentionally left blank]

---

# ACKNOWLEDGEMENTS

First and foremost, I thank Allah for blessing me with this milestone. I humbly dedicate this thesis to my beloved parents who always supported me along my academic journey, may you be proud of me.

My master thesis experience in Bureau Veritas Marine & Offshore was exceptional. First, I would like to thank my friends in the composite section research department for making me feel welcomed, namely, COLLIER Benjamin and DEYDIER Maxime. Special thanks to my master thesis manager, PABOEUF Stéphane, head of the composite materials section, for giving me an opportunity to learn. He is with no doubt a unique well-rounded person both professionally and personally. Lastly, but most importantly, I would like to express my gratitude to my thesis supervisor PETITEAU Jean Christophe, for all his effort and time he gave to support me. He is indeed one of the few intellectual and kind people I have met. The amount of knowledge he gave me, can not be replaced.

Another big thanks for WUILLAUME Pierre-Yves for helping me with HydroStar. I am thankful for OPERA team for their continuous support, namely, PINEAU Jean-Philippe and DAMIEN COACHE. More particularly for MARTIN Sebastien for investing his time and effort for helping me. I sincerely appreciate the help of Vincent ARNAL for sharing his knowledge and support whenever I needed.

I would like to thank Prof. Philippe RIGO for his dedication towards EMship students. He gave us an opportunity to learn and grow. My gratitude extends to EMship coordinator at UPM Simone SAETTONE for his invaluable assistance during our time in Madrid.

Finally, thanks to all my family, friends and EMship colleagues. EMship was a challenging journey for us, but at the end, we prevailed!

---

[This page is intentionally left blank]

---

# ABSTRACT

The expansion in the offshore wind industry is growing rapidly due the substantial amount of energy it can generate. Floating Offshore Wind Turbines (FOWT) have high potential in the energy market for sites with deep water depths. However, these FOWT's platforms are subjected to high dynamic coupling loads which can lead to fatigue in their substructures. The superior properties of FRP materials including better corrosion-resistance, strength-to-weight ratio and fatigue performance make them better candidates compared to steel. As the size of structures increases, the advantages of steel diminish. However, the lack of design guidelines and rules along with technological limitations highlight a research gap for the use of FRP materials in the offshore renewable industry. Unlike other aspects of FOWTs such as foundations, the tower linking the turbine and foundation has not been a primary focus of innovation. The FibreGY project aims to enable the use FRP materials in the marine renewable sector particularly in large offshore wind and tidal platforms. In this thesis, the fatigue analysis of a semi-submersible twin-turbine FOWT tower made with composite materials will be performed. Bureau Veritas (BV) software HydroStar will be used for the FOWT hydrodynamic response. The newly in-house software OPERA developed within the research department of BV Marine and Offshore will be used for the FOWT global response under environmental loads. The stresses within the FRP tower will be obtained by using the analytical model developed in this thesis in a Python script. BV fatigue guidelines will be used to assess the fatigue life of the FRP tower. Design optimization of the FRP tower will be carried out using the developed Python tools for the fatigue life and BV ComposeIT software for the static analysis. FEMAP software will be used for FOWT modelling, static analysis, buckling and modal analysis. The results show that the fatigue damage of the FRP tower using carbon fibre and epoxy resin is very low and sufficient for 20 years design life. The design optimization of the FRP tower shows a reduction of nearly 66% in weight compared to the original total weight with the reference laminates. The optimized FRP tower is able to withstand static loads and fatigue damage while respecting the deflection and buckling criteria.

---

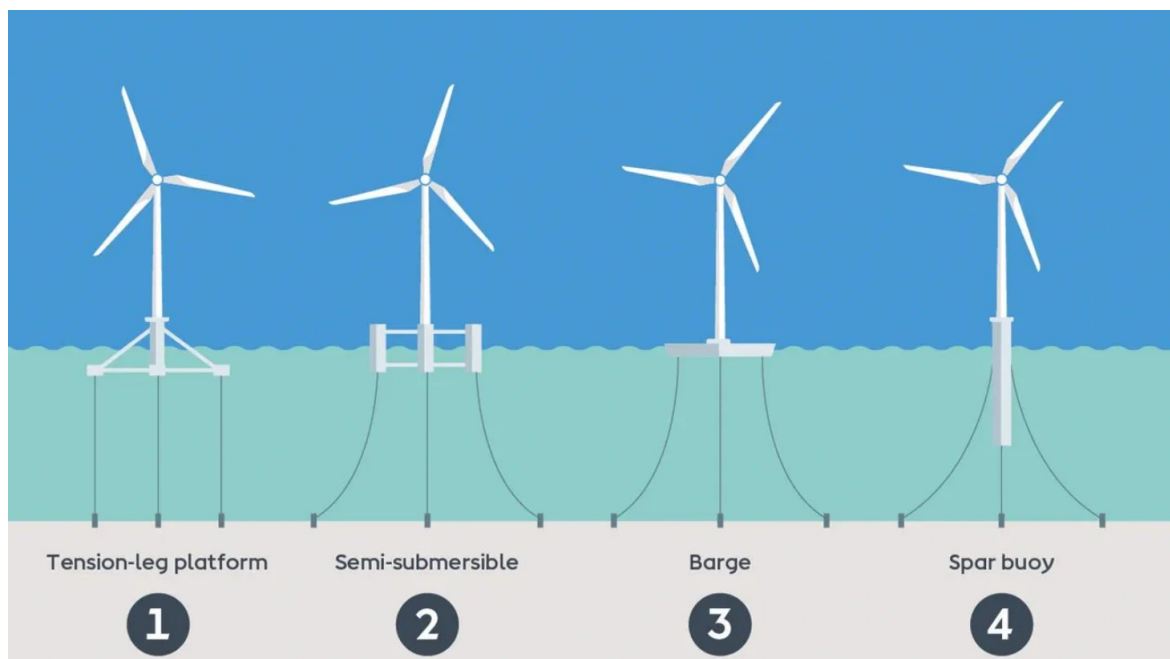
# 1. INTRODUCTION

This thesis is about fatigue analysis of Floating Offshore Wind Turbine (FOWT) Tower made of composite materials. In this section, the background and motivation of the thesis will be presented. Lastly, the objective of the thesis will also be addressed.

## 1.1. Background

Marine Renewable Energies (MRE) has exhibited huge potential in recent years, with more expansion to the open sea [1]. In 2016, the estimated generated electricity from offshore wind, waves, tides and currents was about 42 GWh. Offshore wind alone contributed with 41 GWh [2]. The offshore wind industry advancement in the recent years was promising and cost-effective and this led to the emergence of new technologies such as the use of FOWT platforms [1]. By using FOWT, a huge potential in harvesting wind energy will be unlocked for sites with deeper water depth (more than 50m) [3].

At the moment, majority of OWT are installed in water depths up to 50 meters using fixed-substructures such as jackets, monopiles, gravity base structures (GBS) and tripods [4]. However, due to the attractive advantages of sites in the open sea (water depth more than 50 meters) including less visual impact, less noise mitigation requirements and more steady wind [4], FOWT technologies are gaining some attention. Figure 1.1 shows different types of FOWT foundations [5]. Table 1.1 shows some comparisons of each type of FOWT foundation [6].

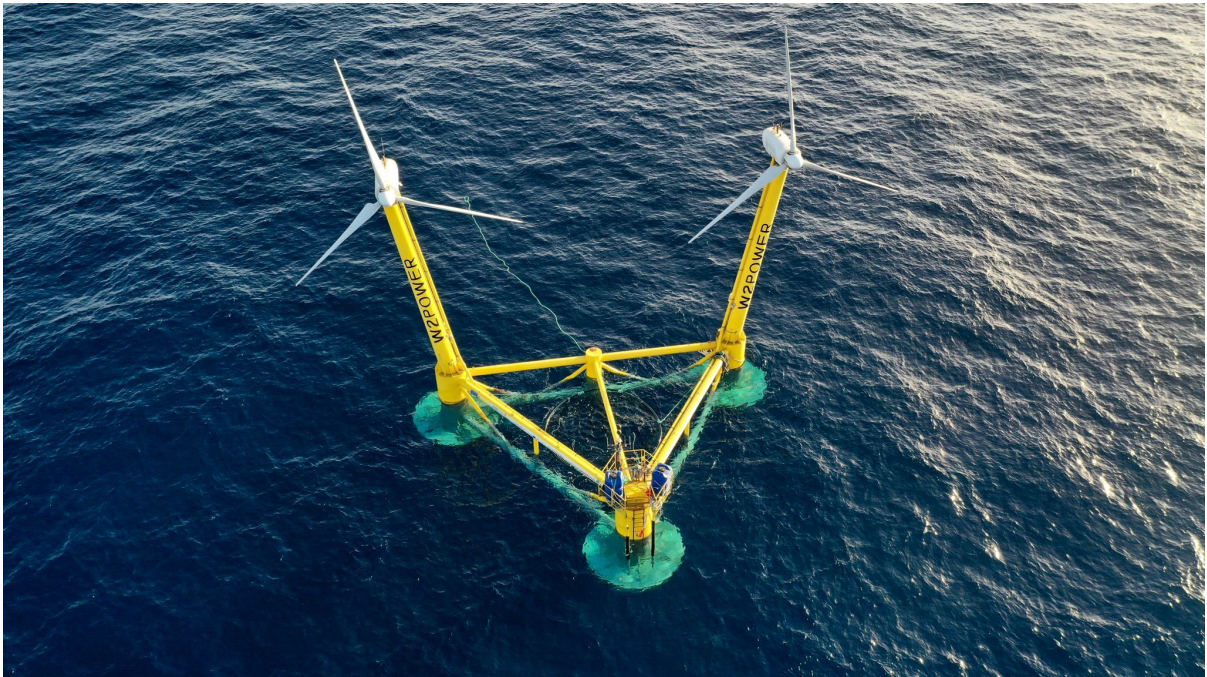


**Figure 1.1:** Types of FOWT foundations.

**Table 1.1:** Comparison between different FOWT foundations.

Platform	Structure	Stability	Station Keeping	T & I	Turbine Installation
Semi-submersible	Complex Large size	Less stable	Simple mooring system Low cost	Towing and low cost	Harbour
SPAR	Simple, Large size	Good	Simple mooring system, Low cost	Complex, Expensive with HLV vessels.	Offshore
TLP	Small	High frequency dynamic loads.	Complex tendons, high cost	Towing, low cost	Harbour

In this thesis, the semi-submersible twin-turbine FOWT designed by Enerocean [7] will be used for the fatigue analysis of the FOWT composite tower. The W2Power FOWT tower in steel will be replaced by Fibre Reinforced Polymer (FRP) towers within the framework of FibreGY project. Figure 1.2 shows the model scale W2Power FOWT [7].

**Figure 1.2:** W2Power FOWT turbine by Enerocean.



The technical feasibility of deploying offshore platforms was demonstrated in the oil and gas industry. However, there are technical challenges for using FOWT in deep waters due to dynamics coupling of the platform and wind turbine [8]. FOWT has a typical design life of 20 to 25 years. During its life time, the different types of structure in the FOWT will be under environmental loads which would lead to cumulative damage at hot-spot elements. In order to evaluate the fatigue damage, different design environmental load cases need to be performed [9].

The offshore wind industry has undergone remarkable growth in recent decades, particularly concerning fixed-bottom structures with cylindrical steel tube towers. Despite significant advancements, the industry is encountering practical limitations in terms of construction techniques for large offshore wind turbines (OWTs) [10]. This highlights a room for improvement using novel support structure concepts.

Unlike other aspects of OWTs such as foundations, the tower linking the turbine and foundation has not been a primary focus of innovation. The practical upper limit of 6-8 meters in diameter for steel towers and monopiles has been recently adopted for transport, manufacturing, and offshore operations [10]. The fast-pace development in the OWT sector has slowed down attempts to seek alternative types of support structures.

This huge growth in the market in terms of water depths, tower heights and turbine mass and size needs to be re-evaluated with a focus on the what type of support structure is most suitable [10]. As the size of structures increases, the advantages of steel diminish. The self weight of steel bring out a new design driver for large OWT structure [10].

## 1.2. Motivation

Since the open sea has extreme environmental conditions, the offshore installation's maintenance costs is effected. Around 60% of the maintenance cost is allocated for corrosion due the enormous amount of steel that is used in the FOWT structures. Fibre Reinforced Polymers (FRP) has better corrosion-resistance and fatigue performance compared to steel. However, at the moment, there are no existing FOWT concepts which is made of FRP materials. This is due to the technological gaps and the absence of design rules and guidelines to showcase the FRP materials workability in the offshore wind industry.

The FibreGY project [11] aims to showcase the feasibility of using FRP materials in the marine renewable sector particularly in large offshore wind and tidal platforms. Figure 1.3 shows the main pillars followed in FibreGY project [11]. The work in this thesis falls within the work package (WP4) that deals with engineering and design guidelines.

---

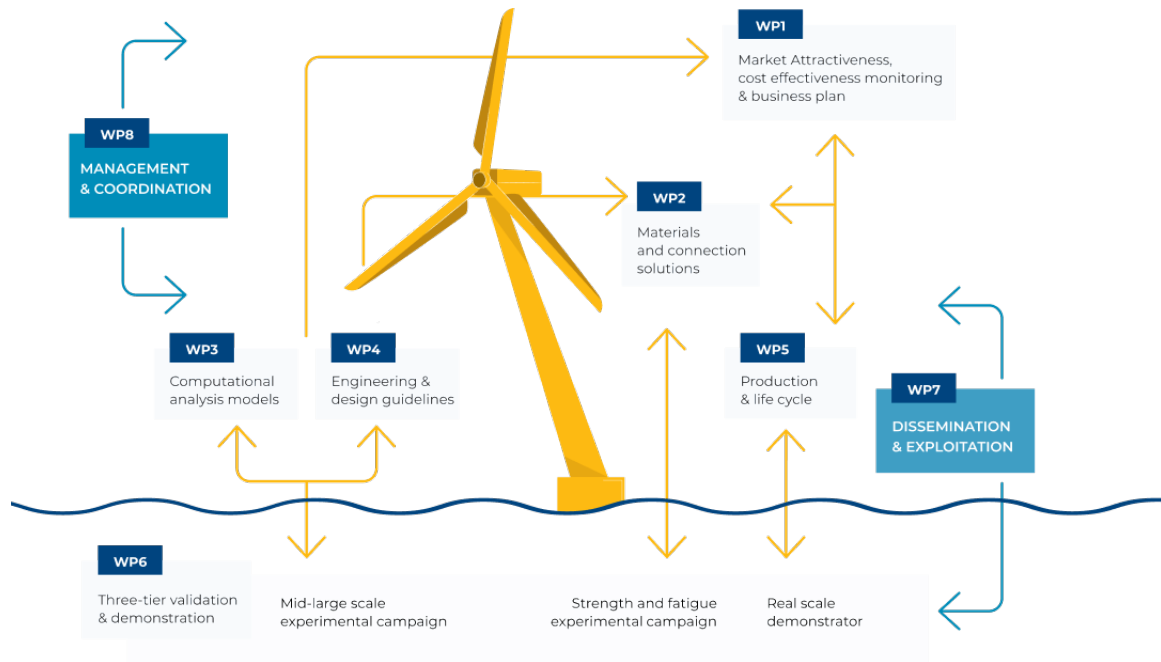


**Figure 1.3:** Main pillars of FibreGY project.

As an alternative to steel, composite materials using carbon and glass fibres offer attractive properties to be used in the offshore environments including [10]:

- Reduced weight to optimize operational efficiency and lower costs.
- Enhanced fatigue performance and resistance to corrosion.
- Long-lasting performance supported by dimensional stability.
- Better durability through a favorable strength-to-weight ratio
- Potential for consolidating multiple components and decreased maintenance requirements.
- Noise reduction for a quieter operational atmosphere

### 1.3. Objective

The objective of this thesis is to perform fatigue analysis of the W2Power FOWT tower made in composite materials. The fatigue methodology developed in [12] by P. Pathak for the FRP tower will be followed with some adjustments. The recommendations stated in [12] will also be addressed. Figure 1.4 shows the general methodology followed in the thesis. In the work of [12], the assessment of stresses in the FRP tower was carried out using FEMAP [13]. However, this was replaced in this thesis using the analytical model coded in a python script for a quicker stress assessment. The analytical model allows fast computation of the ply stresses and fatigue life of the FRP tower. By using the developed python scripts, the design optimization of the different sections of the tower with several

FRP materials is possible to obtain the design safety factors. Due to confidentiality, several data will not be shown throughout the thesis.

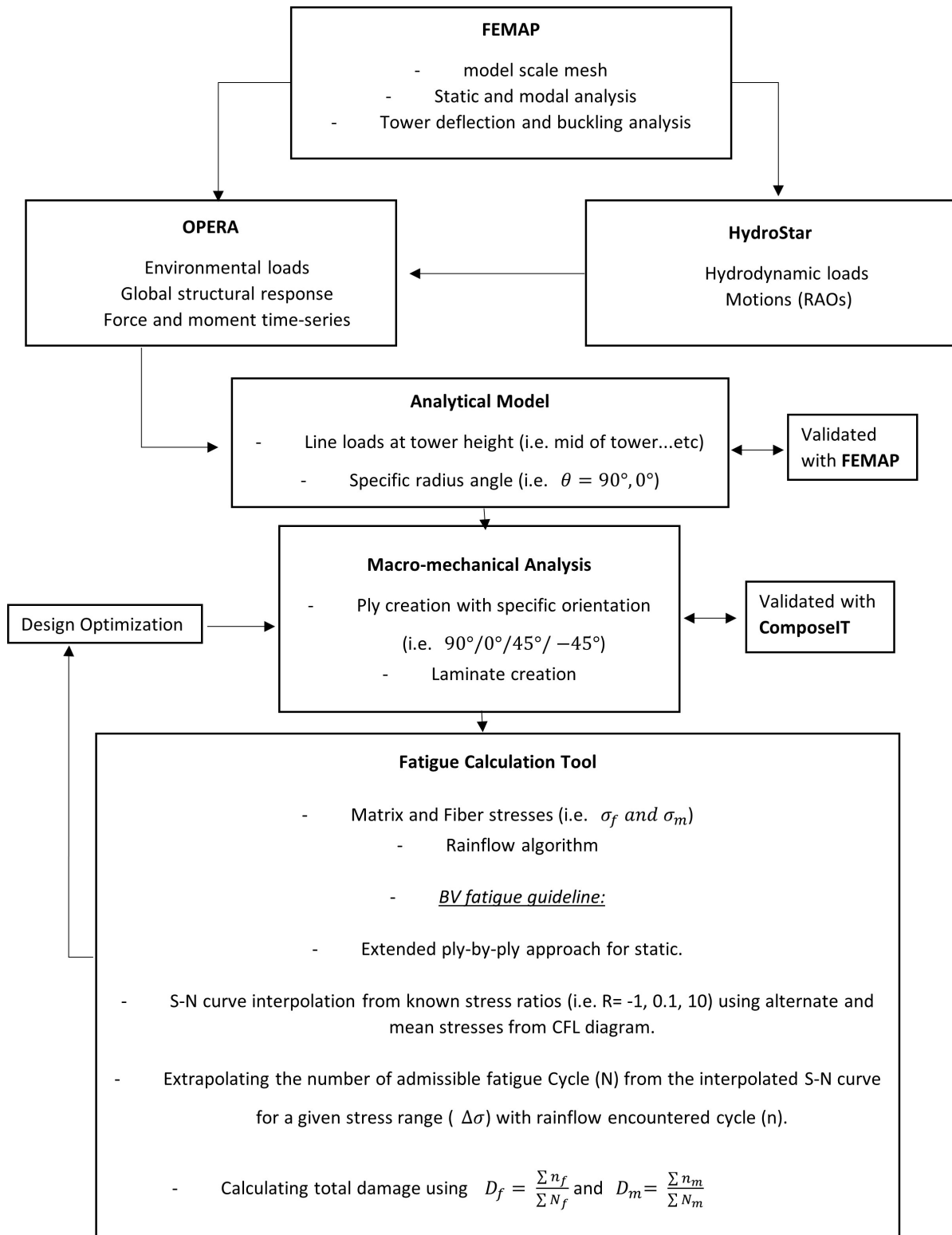


**Figure 1.4:** General methodology of this thesis.

## 2. METHODOLOGY

This section demonstrates the methodology used in this thesis. The section starts with the geometry definition of W2P FOWT, Tower and platform. The steps defining the FRP materials, Hydrodynamic response and global response of the FOWT will be shown. Lastly, the development and validation of the analytical model and fatigue tool will be demonstrated.

### 2.1. Geometry

#### 2.1.1. FOWT

The 3D CAD model of the W2P FOWT was provided by FibreGY partners (Figure 2.1). This model served as the reference for the dimensions and re-modeling needed in further analysis along with other drawings.

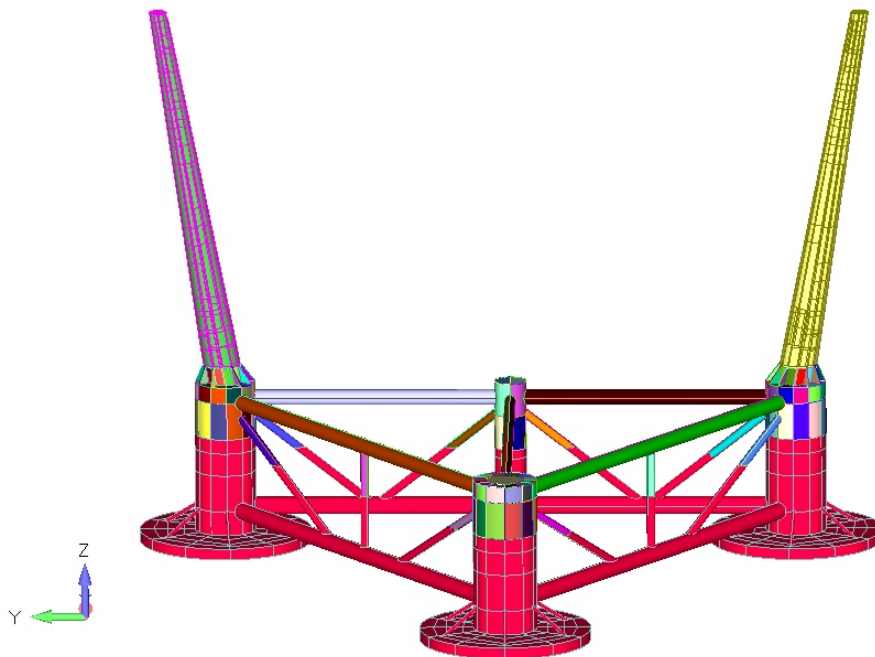


**Figure 2.1:** FOWT 3D CAD model.

#### 2.1.2. FRP Tower

The composite tower was modeled in FEMAP [13] using the drawings provided by FibreGY partners [10]. Figure 2.2 shows the geometry of the FRP tower in FEMAP which will be used for the static (validation) and modal analysis.

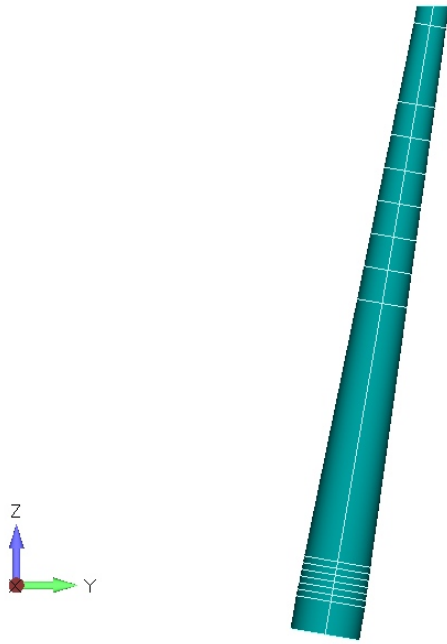


**Figure 2.2:** FRP tower 3D model.

### 2.1.3. Platform

The floating platform was modeled in FEMAP (only the submerged part of the FOWT, Figure 2.3). It will be used as an input mesh for the hydrodynamic analysis with HydroStar [14].

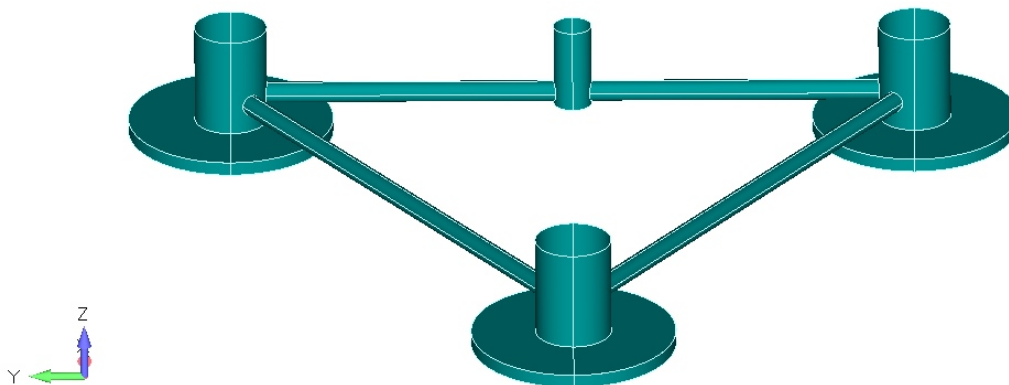


**Figure 2.3:** Floating platform 3D model for HydroStar.

## 2.2. Materials

In this thesis, the material used for the FRP towers is carbon fibre with epoxy resin. The carbon/epoxy plies and laminates were created using BV software ComposeIT [15] which uses the characteristics and calculations provided by BV rules NR546 [16].

The mechanical characteristics, elastic coefficients and breaking stresses for carbon/epoxy Uni-directional (UD) ply are shown in Table 2.1. Two UD plies were created one with 600 mass/m<sup>2</sup> of fibre (0.6 mm thickness) and the other with 300 mass/m<sup>2</sup> of fibre (0.3 mm thickness). The density is 1.56 for both layers. Both layers have the same mechanical characteristics as shown in Table 2.1.

**Table 2.1:** Elastic coefficients (MPa) & Breaking stresses (MPa)

Orientation	E1	E2	G12	G13	G23	$\nu_{12}$	$\nu_{21}$
UD	135731	6621	4416	4416	3091	0.271	0.013
Orientation	$\sigma_{brt1}$	$\sigma_{brc1}$	$\sigma_{brt2}$	$\sigma_{brc2}$	$\tau_{12}$	$\tau_{IL1}$	$\tau_{IL2}$
UD	1628.77	1153.72	66.21	152.29	70.66	58.73	70.66

Referring to Figure 2.2, the composite tower was made with variable laminates across its height with more layers at its base and less at the hub. The tower lay up sequence and number of layers were provided by FibreGY partners. The laminate across the tower was created using the UD plies in Table 2.1.

**Table 2.2:** Laminate location across tower height.

Laminate	Location (m)
N1-Full	L
N5	0.06L
N10	0.07L
N15	0.08L
N20	0.09L
N25	0.1L
N30	0.11L
N8	0.49L
N12	0.54L
N14	0.59L
N16	0.64L
N19	0.69L
N22	0.74L
N23	0.84L

Figure 2.4 shows the sections where the tower thickness varies from the tower base till the top. The laminates locations are shown in Table 2.2 The removed layers are labeled by the index next the N letter which has different orientation and thicknesses depending on the section.

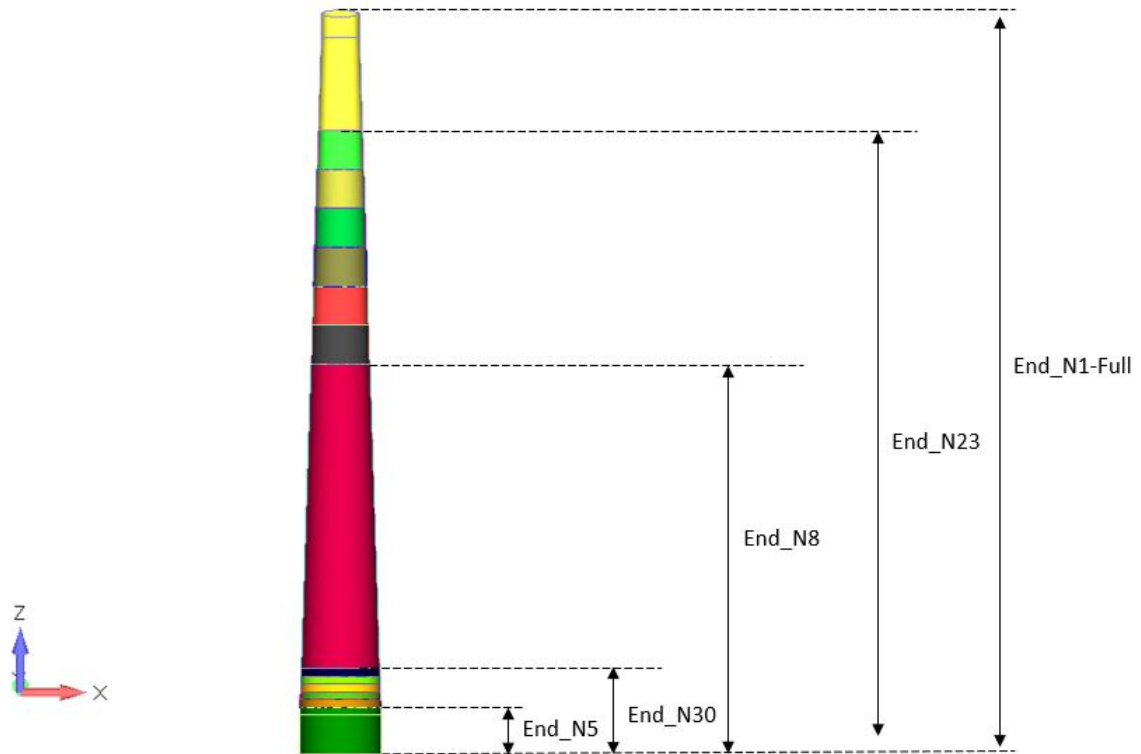


**Figure 2.4:** Carbon FRP Tower layout.

### 2.3. Hydrodynamic Response

FOWTs are designed considering the hydrodynamic response against incident waves to ensure the platform's natural periods do not coincide with normal wave periods typically ranging from 5 to 25 seconds [17]. If the waves period match the platforms natural period a phenomena called resonance will occur which will ultimately lead to the platforms instability. A floating platform has six Degrees of Freedom (DOF). Figure 2.5 shows the FOWT DOF including three translational (surge, sway and heave) and three rotational (roll, pitch and yaw).

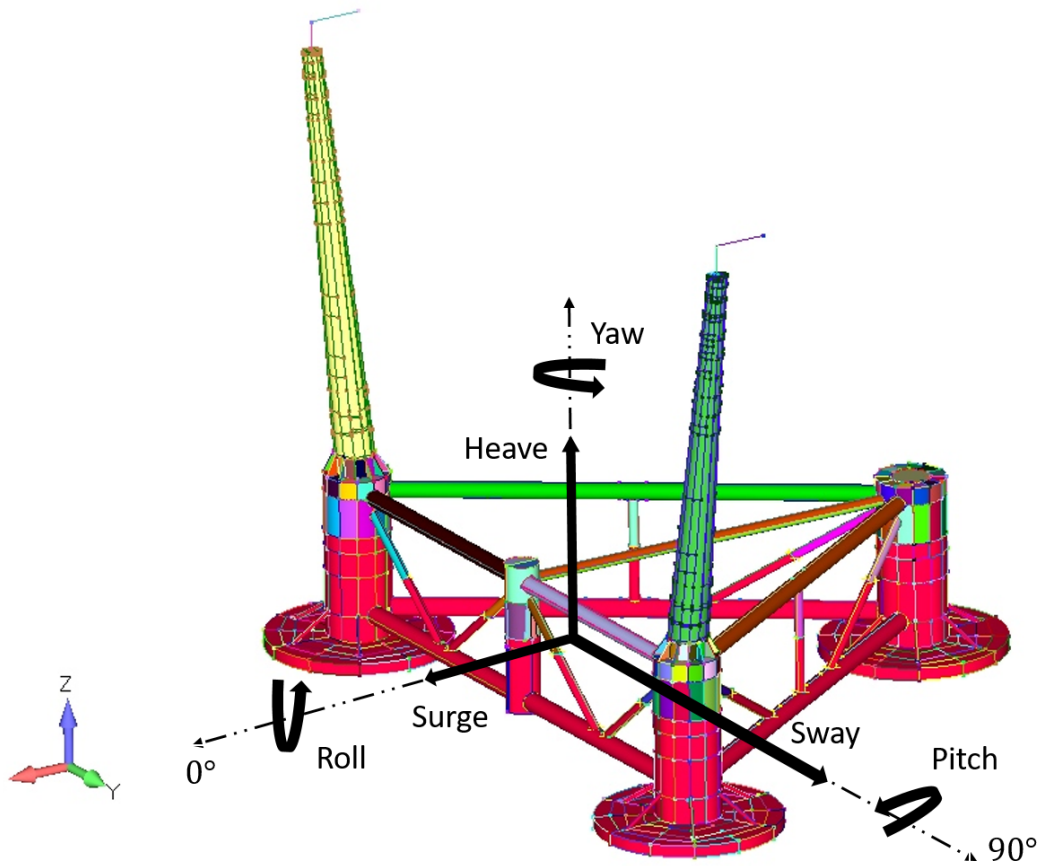


**Figure 2.5:** FOWT Degrees of Freedom.

To evaluate the hydrodynamic response of the platform, BV HydroStar [14] software is used. HydroStar was developed since 1991 in BV which calculates loads and motions of ships and floating units using diffraction and radiation first order problem and the Quadratic Transfer Function (QTF) second order low frequency wave loads [14]. Figure 2.6 shows the flowchart of the steps followed in HydroStar to compute the loads and motions of the FOWT. The following subsections will describe the steps shown in Figure 2.6 with more details.



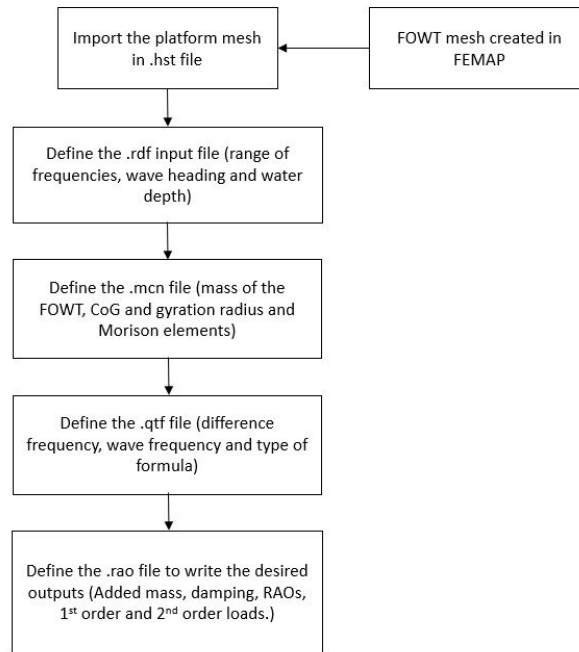


**Figure 2.6:** HydroStar flowchart.

### 2.3.1. FOWT platform mesh

In HydroStar, only the submerged part of the FOWT platform is used. Using FEMAP [13], the platform is modeled considering the draft part only. In the work of [12], the platform was modeled with the thin braces connecting the cylindrical columns, Figure 2.7. However, HydroStar is a diffraction radiation solver that works with big structures suited to the wave length.

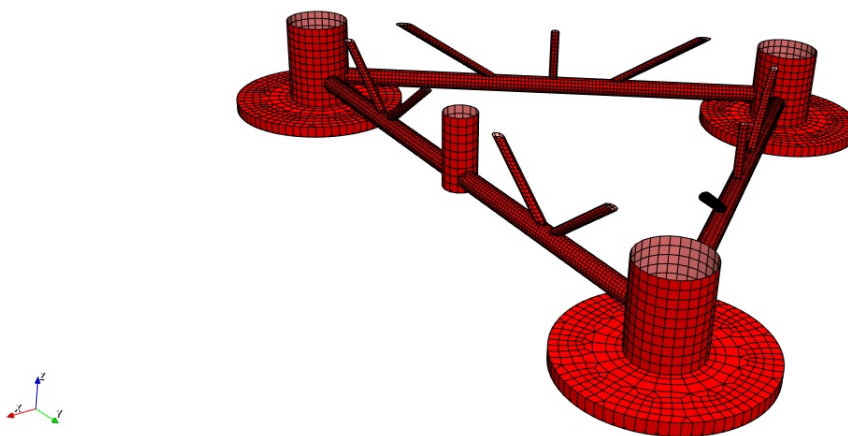


**Figure 2.7:** Platform mesh in HydroStar based on the work of.

Offshore structures like FOWT platforms are made of thin structures that connects large structures. These thin structures have low response under diffraction-radiation loads [14]. In case of thin structures with respect to the wave length, Morison equation is used instead of radiation-diffraction approach. In this thesis, to accurately model the platform, the braces are removed and for the motions input file in HydroStar they are added as Morison elements. Figure 2.8 shows the platform model used for the hydrodynamic response of the platform in HydroStar.

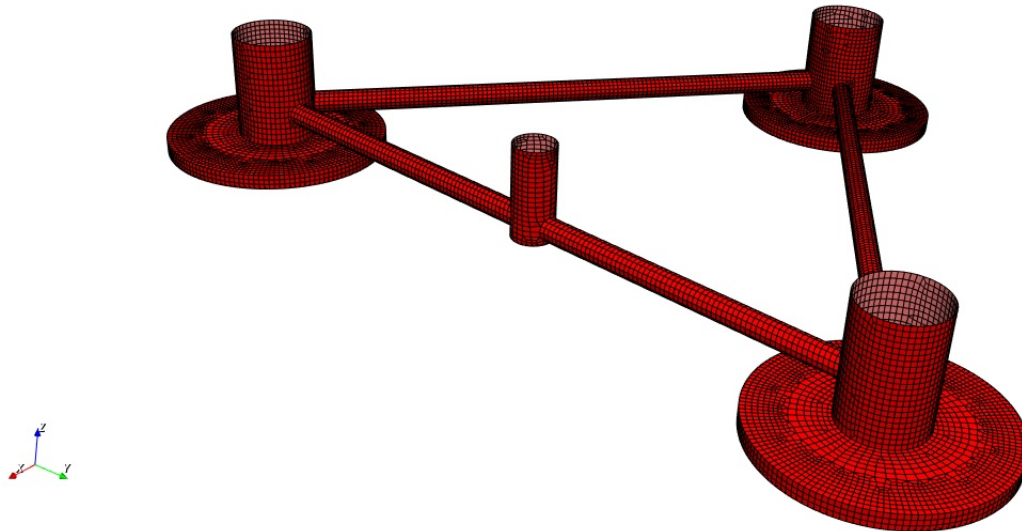


**Figure 2.8:** Platform mesh in HydroStar used in this thesis.

It can be seen that the mesh is finer in general compared to Figure 2.7 particularly for the heave plates thickness as it is recommended to have at least three elements across the thickness of the heave plates. Only half of the platform is meshed in FEMAP and it is exported to HydroStar using symmetrical bodies to reduce the the number of elements and hence the overall simulation time.

```

... Consistence checking finished.
... Superposition checking finished.

... Neighborhood checking finished.

```

```

In total: nb of zero-area panels      = 0
          nb of panels over free surface = 0
          nb of panels at free surface = 0
          nb of superpositions        = 0
          nb of inconsistencies       = 0
          nb of neighbor-absences     = 0
          nb of symmetry problem      = 0

```

**Figure 2.9:** Platform mesh check in HydroStar.

Before running the simulation in HydroStar radiation and diffraction module, the mesh convergence is checked to ensure there are no issues with the mesh such as inconsistency of the elements, number of panels over the free surface and elements normal directions etc. Figure 2.9 shows the summary of the mesh check in HydroStar.

### 2.3.2. Radiation and diffraction

After the successful check of the mesh, the radiation and diffraction module was executed with range of frequencies starting from 0.05 rad/s to 2 rad/s with a step of 0.05 rad/s. The choice of a small frequency step is for better visualization of the results especially around the natural periods/frequency of the FOWT's platform. The wave heading considered here is  $0^\circ$  according to Figure 2.5. The water depth needs to be defined, due to confidentiality it is not stated here. Figure 2.10 shows the input file for the radiation and diffraction module.

```
FILENAME platform

FREQUENCY TYPE 2
WMIN 0.05
WMAX 2.0
WSTP 0.05
ENDFREQUENCY

HEADINGS TYPE 1
0.0
ENDHEADINGS

#SPEEDS TYPE 0
#1 0.0
#ENDSPEEDS

WATERDEPTH Confidential

ENDFILE
```

**Figure 2.10:** Radiation and diffraction (Hsrdf) module input file in HydroStar.

Radiation and diffraction module computes the radiation and diffraction components in terms of added mass, and the first order wave loads. The output file from this module is an input to mechanical module.

### 2.3.3. Motions

The mechanical module computes the FOWT's platform motions. In the mechanical input file, we need to define the FOWT's mass, Centre of Gravity (CoG), radius of gyration and Morison elements. Figure 2.11 shows the mechanical input file definition.

```

FILENAME platform

MASS_BODY 1 confidential
COGPOINT_BODY 1 confidential
GYRADIUS_BODY 1 confidential

MORISON
1 CIRC x1 y1 z1 x2 y2 z2 D Cm Cd Nseg
ENDMORISON

WAVEAMPLITUDE 1

ENDFILE

```

**Figure 2.11:** Mechanical (Hsmcn) module input file in HydroStar.

The FOWT CoG is calculated using the the following equation:

$$CoG_i = \frac{W_k \times (CoG_k)_i}{\text{Total weight}} \quad (1)$$

where  $i$  is the reference axis ( $x$ ,  $y$  and  $z$ ) and  $k$  is the item index that has mass ( $W_k$ ) on the platform (i.e. turbine and platform etc.). The total weight is the summation of every item on the platform. The radius of gyration is provided by FibreGY partners.

To add a Morison element in HydroStar, a circular beam is defined with its coordinates at both extremity, the diameter, user-defined drag and mass coefficients and number of segments along the beam. For FOWT's platform used in this thesis, 10 Morison elements are added to consider the braces connecting the cylindrical columns of the platform. Figure 2.12 shows the FOWT platform mesh with Morison elements.

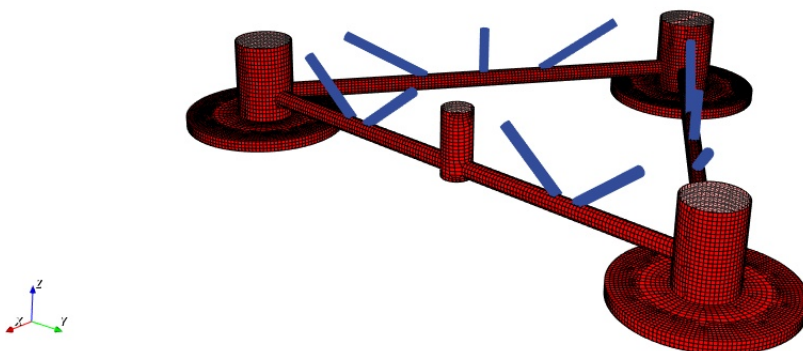


**Figure 2.12:** Platform mesh in HydroStar with Morison elements.

### 2.3.4. 2nd order loads

The second order potential is solved using the full QTF calculation. In HydroStar the QTF calculation is done in two steps, pre-processor and calculation step by the QTF input file (low or difference frequency) [14]. Figure 2.13 shows the input file for 2nd order loads (QTF).

```
DIFFERENCE 0.0 0.1 0.1
WAVFREQUENCY 0.1 2.0 0.1
TYPEFORMULE NEAR-FIELD

ENDFILE
```

**Figure 2.13:** QTF (Hsqtf) module input file in HydroStar.

HydroStar gives the option of choosing the formulation either near-field and middle field, only one can be chosen. First order waves and motions need to be evaluated for the near field formulation.

### 2.3.5. Transfer functions

After performing the simulations, the transfer functions module in HydroStar is used to construct some outputs including Response Amplitude Operators (RAOs), added mass, damping matrices and wave diffraction loads (1st order loads), drift loads and QTFs low and high frequency. Figure 2.14 shows the definition of Transfer functions input file.

```
CM FILE adm.dat TERM 11 22 33 44 55 66
CA FILE dmp.dat TERM 11 22 33 44 55 66

GSURGE BODY 1 FILE surge.rao AMP
GSWAY BODY 1 FILE sway.rao AMP
GHEAVE BODY 1 FILE heave.rao AMP
GROLL BODY 1 FILE roll.rao AMP
GPITCH BODY 1 FILE pitch.rao AMP
GYAW BODY 1 FILE yaw.rao AMP

FXF1ST FILE fxf1st.rao AMP
FYF1ST FILE fyf1st.rao AMP
FZF1ST FILE fzf1st.rao AMP
MXF1ST FILE mxf1st.rao AMP
MYF1ST FILE myf1st.rao AMP
MZF1ST FILE mzf1st.rao AMP

DRIFTFX BODY 1 FILE drift_fx.qtf PRE
DRIFTFY BODY 1 FILE drift_fy.qtf PRE
DRIFTFZ BODY 1 FILE drift_fz.qtf PRE
DRIFTFX BODY 1 FILE drift_fxff.qtf MOM
DRIFTFY BODY 1 FILE drift_fyff.qtf MOM
DRIFTMZ BODY 1 FILE drift_mzff.qtf MOM
```

**Figure 2.14:** Transfer functions (Hsrao) module input file in HydroStar.

The output from HydroStar will be used as inputs for the global response of the FOWT in OPERA software [18].

## 2.4. FOWT Global Response

To assess the global response of the FOWT under environmental loads (i.e. wind, waves, current), BV software OPERA is used. OPERA is an in-house multi-physics software developed in the research department at BV marine and offshore [18]. By multi-physics it accounts for the interaction between the hydrodynamic, aerodynamic, mooring and mechanical aspects.

In this thesis, OPERA will be used to assess the global response of the FOWT and obtain the global internal loads on the tower. This section explains the steps followed in OPERA to compute the global response.

### 2.4.1. Site

In OPERA, the first step is to define seabed connectors (anchor positions in the seabed) and the water depth. Although the water depth for each anchor position is different, in this thesis, an average water depth for the three anchor points is used to ensure uniform seabed. A global connector is also defined here at the water surface to be used later in the assembly. Figure 2.15 shows the site definition in OPERA with the three anchors connectors at seabed and global connector at the water free surface.

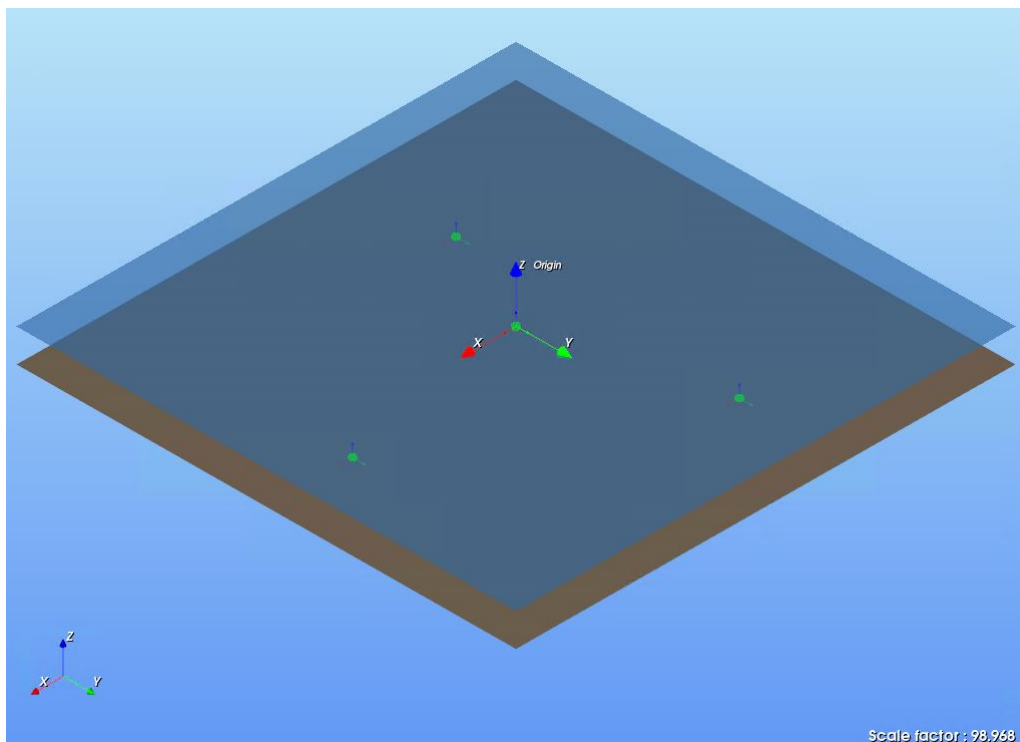


**Figure 2.15:** Site definition in OPERA.

### 2.4.2. Floater

The next step in OPERA is to define the floater (floating platform). The floater 3D model is imported from FEMAP as shown in Figure 2.16.

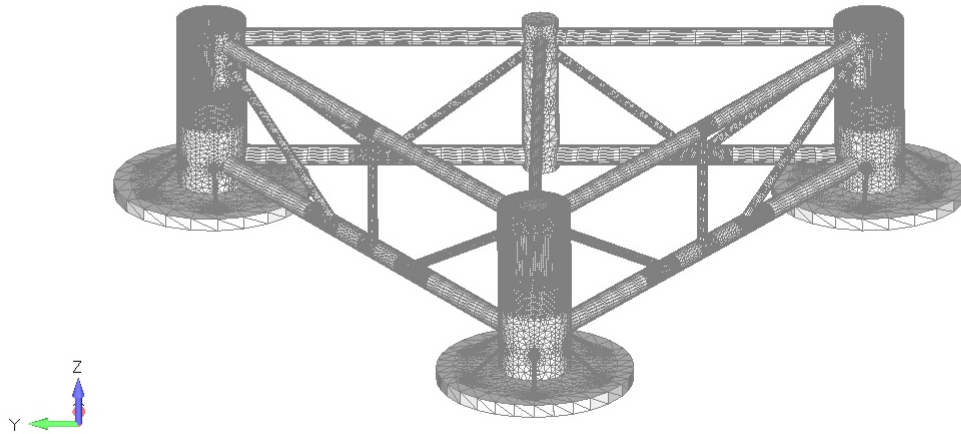


**Figure 2.16:** Floating platform mesh in FEMAP.

In OPERA, the floater 3D model is used only for rendering. Number of connectors need to be defined here. First, a global connector at the water free surface to be assembled later with the site global connector. A fairlead connector at the bottom of the heave plate and two connectors for the turbines base. Figure 2.17 shows the floater defined in OPERA with all the connectors.

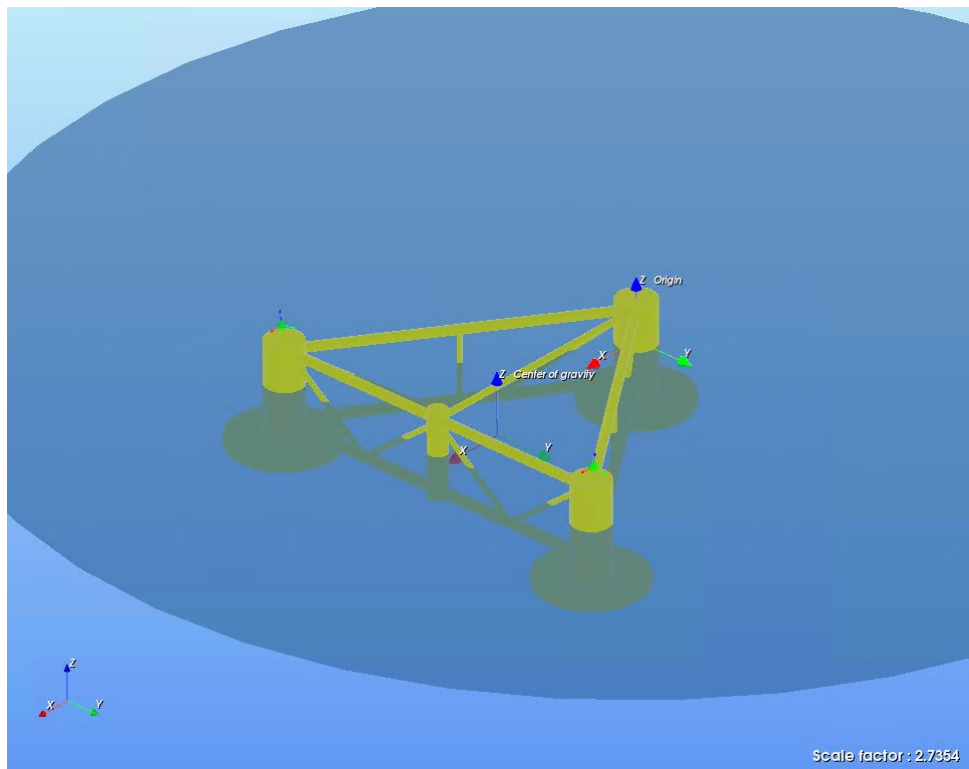


**Figure 2.17:** Floater definition in OPERA.



In the floater section, a load case needs to be created. The loading components for a load case includes the following:

- **Inertia**

The floater CoG ( $x$ ,  $y$  and  $z$ ) in  $m$ , displacement in  $m^3$ , mass in  $kg$  and the coefficients of the inertia matrix [18] in  $kg.m^2$  expressed as:

$$I_{rot} = \begin{Bmatrix} I_{xx} & 0 & 0 \\ 0 & I_{yy} & 0 \\ 0 & 0 & I_{zz} \end{Bmatrix} = \begin{Bmatrix} M \times R_{xx}^2 & 0 & 0 \\ 0 & M \times R_{yy}^2 & 0 \\ 0 & 0 & M \times R_{zz}^2 \end{Bmatrix} \quad (2)$$

where  $R_{xx}$ ,  $R_{yy}$  and  $R_{zz}$  are the radius of gyration of the floater at each axes.  $M$  is the floater mass.

The mass of the floater is used to obtain the gravity load of the floater. The floater displacement  $\Delta$  in  $m^3$  is used to compute Archimedes load defined as:

$$\text{Archimedes Load} = \rho \times g \times \Delta \quad (3)$$

where  $\rho$  is the sea water density in  $kg/m^3$  and  $g$  is the gravity in  $m/s^2$ .

- **Hydrodynamics**

In this part, we need to define the hydrodynamic characteristics of the floater. The added mass, radiation damping, hydrostatics, first-order motions and loads and the second order QTF load. All these are imported from the results obtained in HydroStar software for the Hydrodynamic response explained in Section 2.3. It should be noted that motions are only used for post-processing in OPERA [18].

- **Wind**

The wind acting on the floater was defined using a wind coefficient. The value of the coefficient was provided by the FibreGY partners [10]. In addition, the transverse and longitudinal areas (in  $m^2$ ) of the floater were added as inputs to compute the wind drag force acting on the floater.

- **Morison elements**

Morison elements are defined in OPERA to be used later for the Morison elements load to account their drag load. The information needed to define Morison elements in OPERA are the same as in HydroStar in Figure 2.11. It should be noted that only the drag coefficient is taken into account in OPERA since the added mass were already computed in HydroStar. The whole submerged part therefore need to be defined except the heave plates. Figure 2.18 shows a visualization of the Morison elements considered in OPERA.



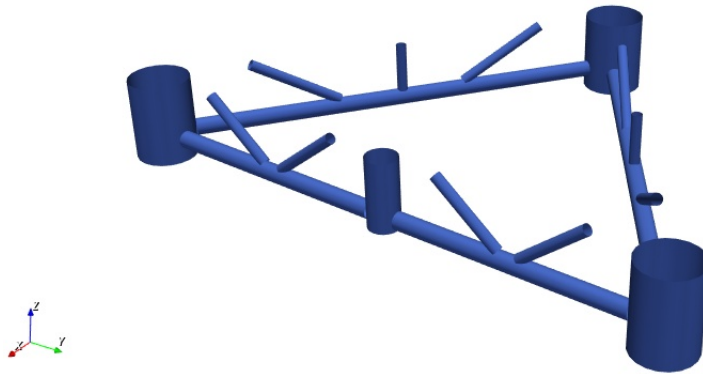


**Figure 2.18:** Morison elements definition in OPERA.

- **Heave plate elements**

Heave plates were defined to account for their heave plate elements drag load. The coordinates, diameters and thicknesses of each of the three heave plates were used as input.

### 2.4.3. Mooring lines

The FOWT platform is moored with three mooring lines connected to the same fairlead at the bottom of the heave plate. In OPERA, the mooring lines were defined by the segments they consist of. The length, diameter and mechanical properties in air and fluid need to be defined. The mooring lines properties and characteristics were provided by FibreGY partners [10]. Figure 2.19 shows the mooring line definition in OPERA.

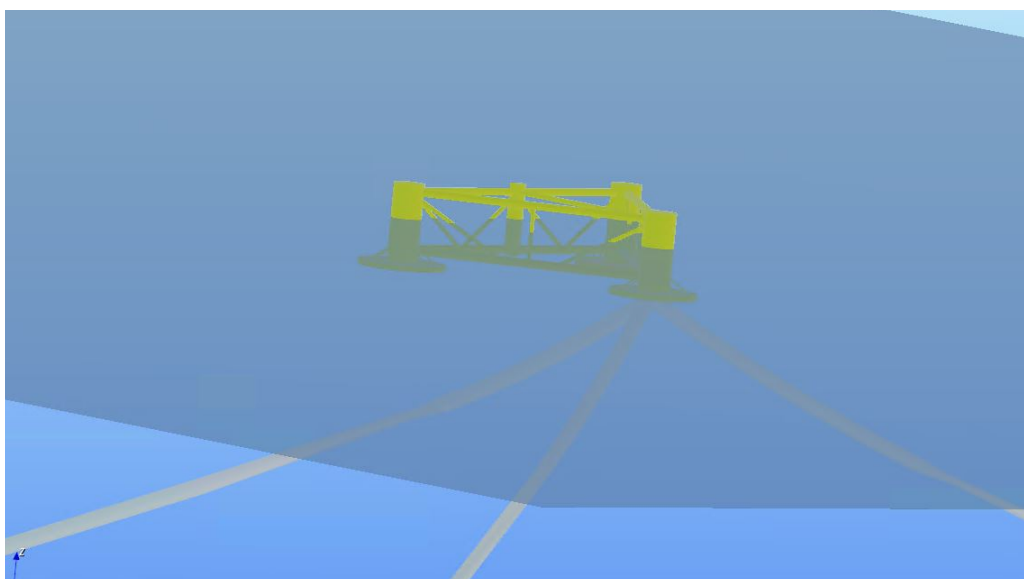


**Figure 2.19:** Mooring lines definition in OPERA.

The mooring radius between the three anchors is shown in Figure 2.20. As mentioned before, the footprint or mooring radius is assumed to be the same for the three mooring lines.

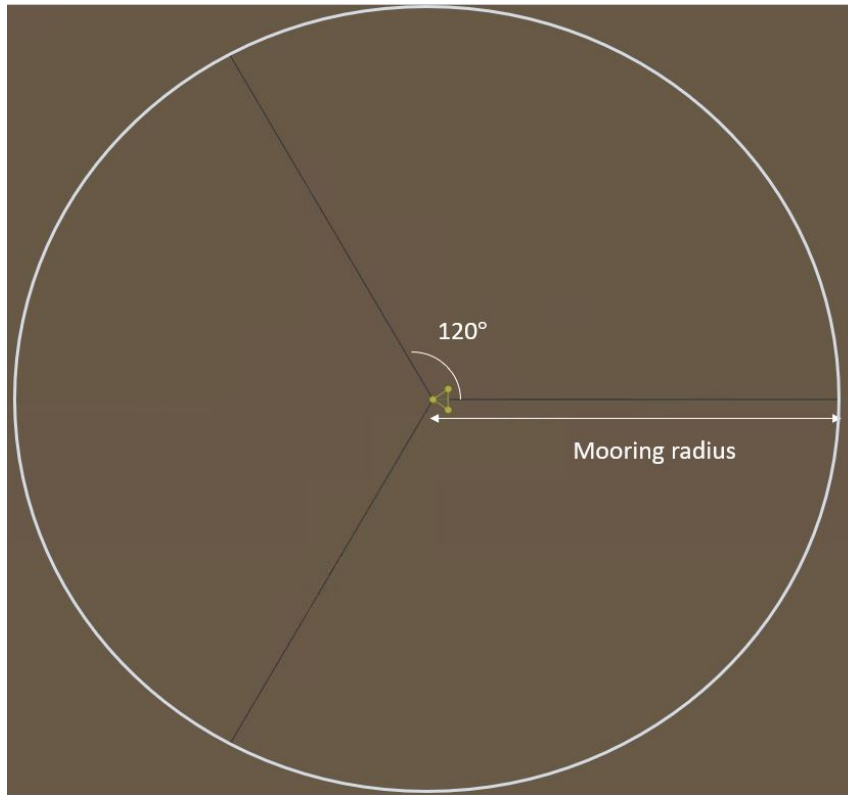


**Figure 2.20:** Mooring radius in OPERA.

#### 2.4.4. Turbine

The FOWT platform has two turbines as shown in Figure 1.2. In OPERA, the turbine was defined based on its components. The followings are the turbine components defined individually.

- **Tower**

In order to define the tower geometry, we need to specify its length, inner and outer radius. The mechanical properties of the tower needs to be defined such as the linear mass, Young modulus, poisson ratio and stiffnesses (shear, axial, bending and torsional). In this thesis, the tower is assumed to be rigid.

- **Blade**

The blades were modeled using the unconstrained profile of a reference blade due to lack of information from the blade manufacturer. The blade mass was provided by FibreGY partners and therefore the linear mass of the blade was defined to yield the same mass. Similar to the tower, the blade was assumed to be rigid.

- **Other components**

The mass of the nacelle and tower and their CoG were provided by FibreGY partners. There were no data provided for the controller, generator and shaft. Figure 2.21 shows the turbine definition in OPERA.



**Figure 2.21:** Turbine definition in OPERA.

#### 2.4.5. Environment

In OPERA, the environment conditions are defined in this section. Regular waves, wave spectrum, wind spectrum, wind function, wind time series, in-flow wind velocity and current can be defined. In the FibreGY project [10], the only environmental conditions that will be considered are wave and wind.

- **Wind**

According to FibreGY project [10], the design condition selected for fatigue assessment is power production under normal operation. The design load cases were selected based on IEC 61400-2 [19].

As part of the assumptions set in the FibreGY project, only a time-series thrust acting along the x-axis direction at the hub will be considered. Due to lack of information on the operation of the turbine, the steady wind thrust is computed according to [19] using the following expression:

$$F_x = \frac{1}{2} C_T \rho_{air} V^2 \pi R^2 \quad (4)$$

where  $C_T$  is the thrust coefficient provided by FibreGY partners according to [19],  $\rho_{air}$  is the air density,  $\pi R^2$  is the rotor swept area and  $V$  is the steady wind velocity plus an extreme operating gust. The wind velocity in Eq. 4 will be computed based on the following equation:

$$V(t) = \begin{cases} V(z) - 0.37V_{gustN} \sin \frac{3\pi t}{T} (1 - \cos \frac{2\pi t}{T}) & \text{for } 0 \leq t \leq T \\ V(z) & \text{for } t < 0 \text{ and } t > T \end{cases}$$

where  $V(z)$  is taken here as the steady wind velocity at the hub ( $V_{hub}$ ) and  $V_{gustN}$  is the gust velocity calculated according to Eq. 12 in [19].  $T$  is 10.5 s for  $N = 1$  and  $t$  is the time. Figure 2.22 shows the time-series velocity at the hub.

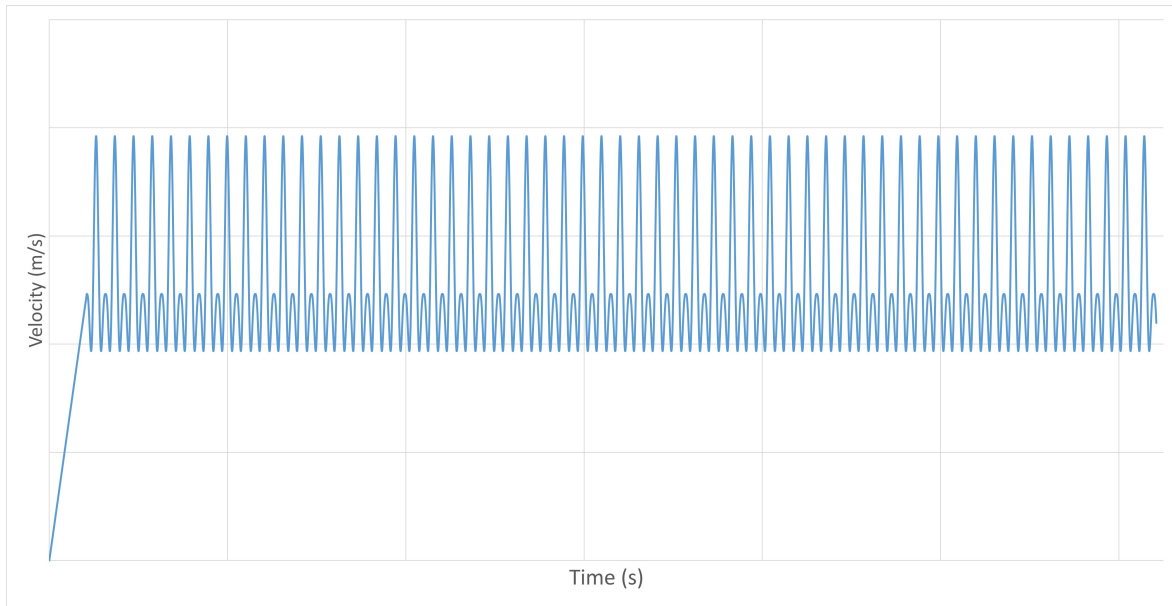


**Figure 2.22:** Wind time-series velocity.

Referring to Figure 2.22, there is a linear transition interval of velocity before the  $V(t)$  is used. This is used to avoid sudden oscillation due to high wind velocity. This transition interval will not be taken into account when evaluating the fatigue damage of the FRP tower. The thrust load at the hub, obtained using Eq. 4 is plotted in Figure 2.23.

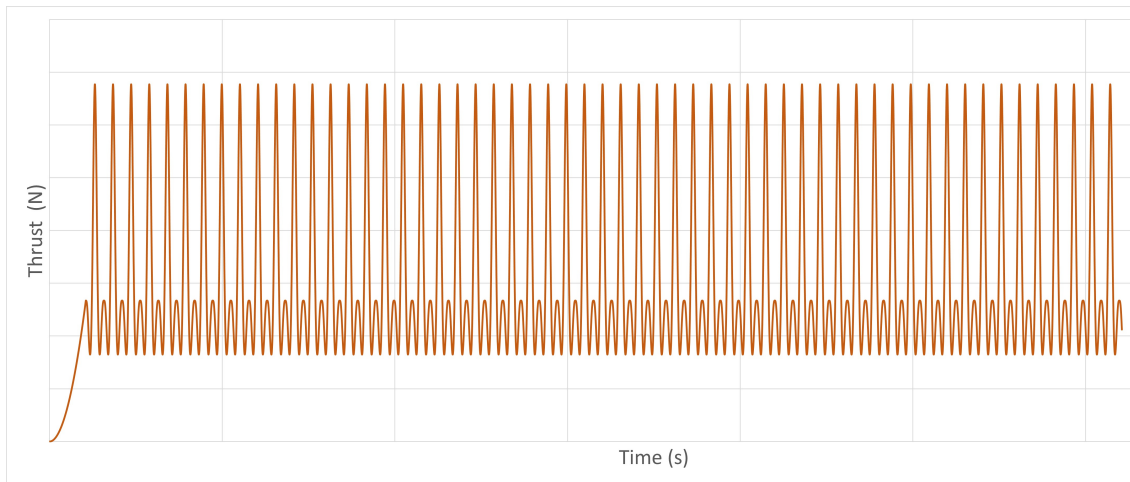


**Figure 2.23:** Wind time-series thrust.

Beside the time-series thrust load applied at the hub, an equivalent pressure will be applied to exposed surfaces to wind that is the tower and platform. The following expression is used to compute the wind pressure on the tower and platform:

$$P = \frac{1}{2} C_f \rho_{air} V_a^2 \quad (5)$$

where  $C_f$  is taken based on Table 3 in [19],  $V_a$  is the wind profile at each elevation. It is expressed as:

$$V_a = V_{hub} \left( \frac{Z_a}{Z_{hub}} \right)^{0.2} \quad (6)$$

where  $Z_a$  is the elevation in  $m$  at which  $V_a$  is acting on and  $Z_{hub}$  is the hub elevation from the water free surface. Figure 2.24 shows the wind profile and pressure from the free surface up to the hub.

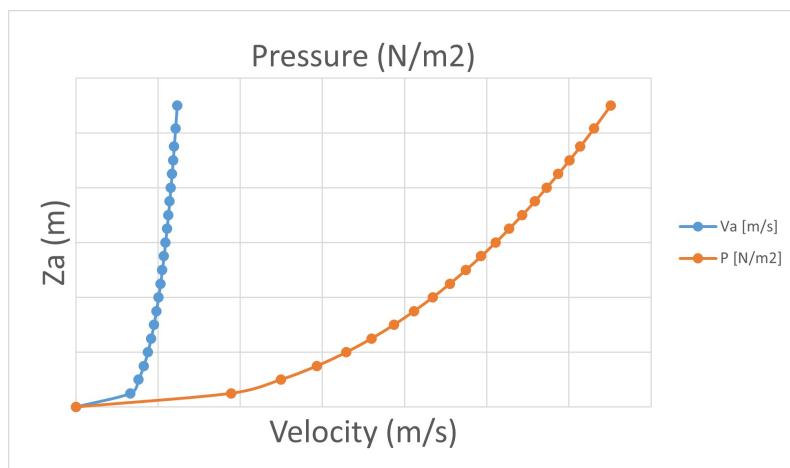


**Figure 2.24:** Wind velocity and pressure on the FOWT exposed surfaces.

Eq. 5 is added in OPERA as a wind function for the tower wind pressure and the  $C_f$  coefficient is added for the platform in the floater section.

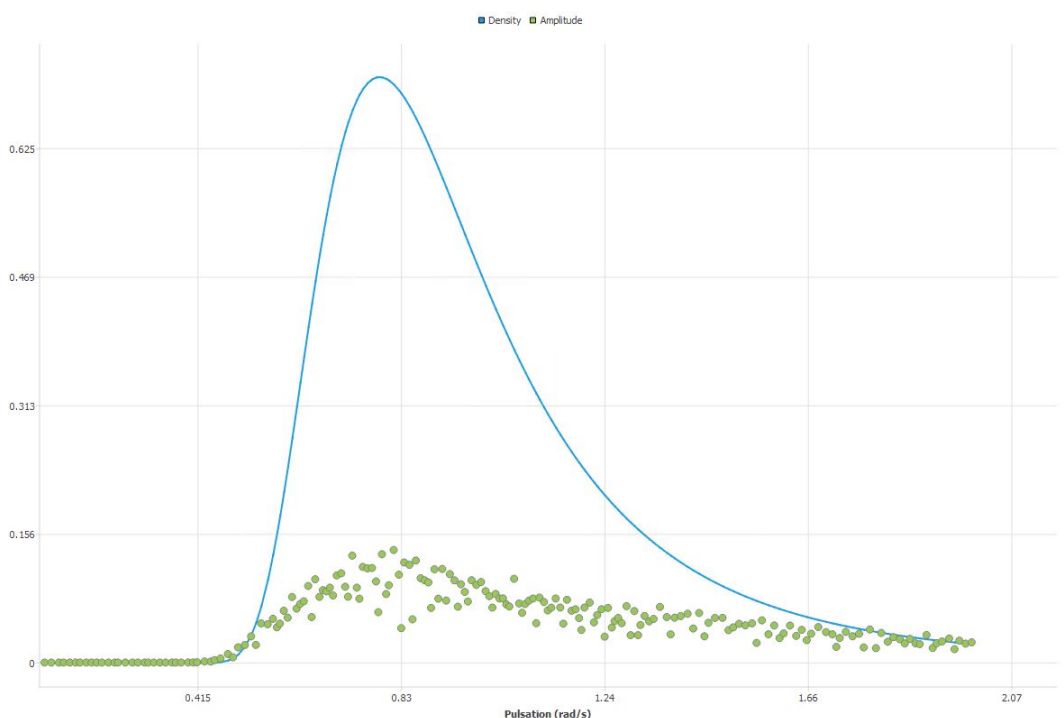
- **Wave**

For fatigue assessment, the normal design load case for waves was considered. The normal wave conditions correspond to the wave height related to the normal design wind speed, according to [20]. Based on the meta-ocean data gathered in the specific site for the FOWT as reported in [10], the normal wave condition was defined from the most frequent peak periods combined with biggest wave height. Table 2.3 shows the normal wave condition specifications used for fatigue assessment.

**Table 2.3:** Specifications of the normal wave condition used in OPERA.

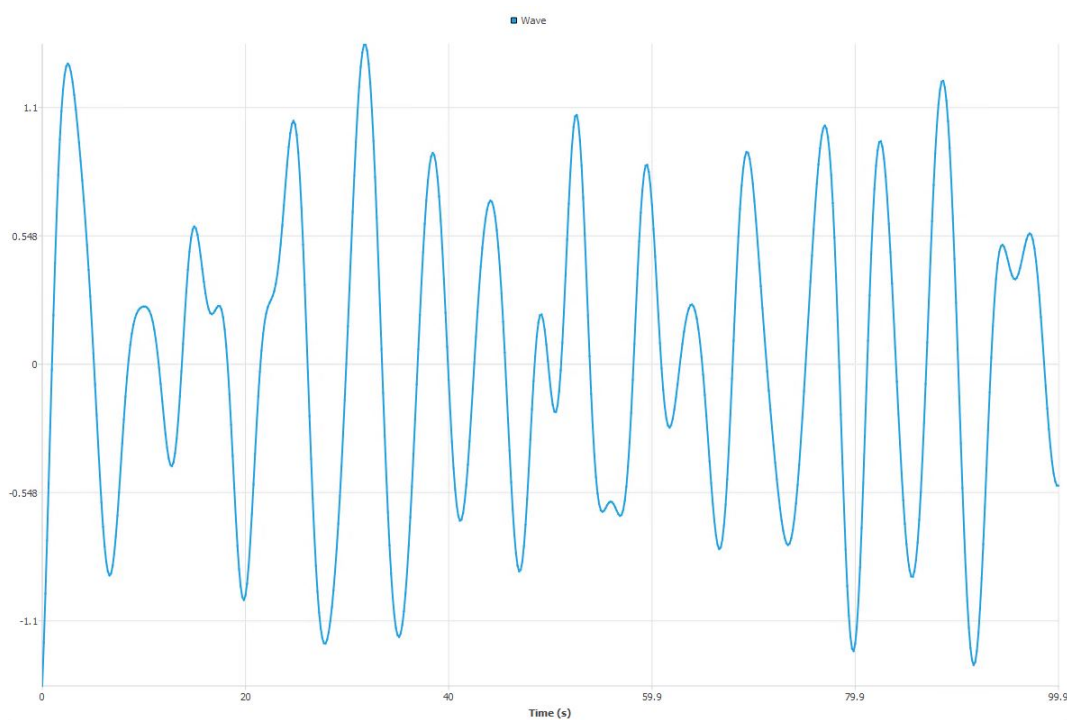
Wave spectrum	JONSWAP
$H_s$	2.5 m
$T_p$	8 s
$\gamma$	1
Wave heading	0°

Figure 2.25 shows the JONSWAP spectrum.



**Figure 2.25:** JONSWAP spectrum.

Figure 2.26 shows the time-series plot of JONSWAP spectrum using the data in Table 2.3



**Figure 2.26:** JONSWAP spectrum time-series.

#### 2.4.6. Assembly

In this section, all the FOWT components defined above were assembled. Figure 2.27 shows the assembly of the FOWT in OPERA.

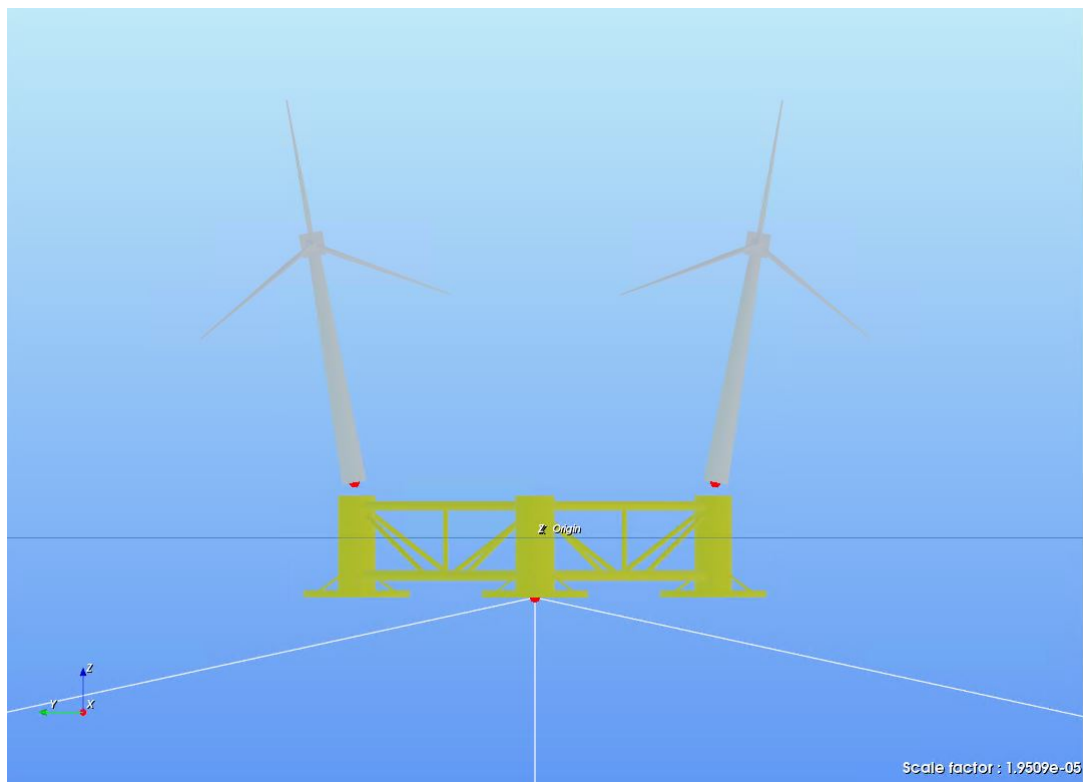


**Figure 2.27:** Assembly of FOWT in OPERA.

From Figure 2.27, the base of both turbines were connected to the floater using kinematic connection with clamped boundary condition.

The fairlead at the bottom of the heave plate was connected to the anchors through lines connection with free boundary condition.

The site and floater global connectors were assembled together with kinematic connection with free boundary condition. Figure 2.28 summarizes the assembly of the FOWT components with their boundary conditions.

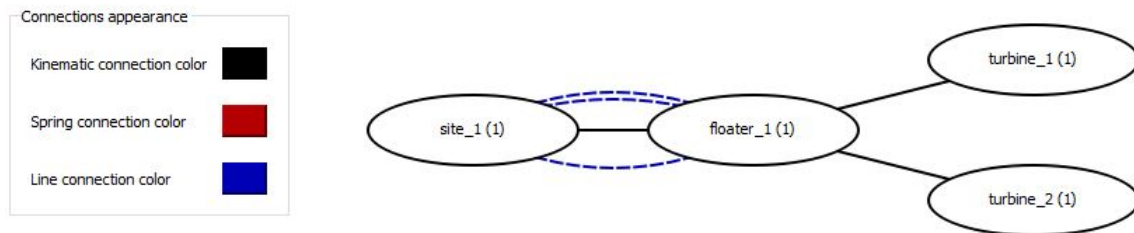


**Figure 2.28:** Kinematic tree of FOWT Assembly in OPERA.

#### 2.4.7. Analysis

The simulation duration, time step, starting time and scheme are defined here. The physical parameter of the environment like water and air density and gravity acceleration are specified.

The loads acting on the different components of the FOWT need to be selected in this section. Table 2.4 shows the considered loads for the floater.

Beside the simulation time and loads definition, the calculation options need to be defined. The tower and blades were set to be rigid. The mooring lines were computed using the quasi-static analysis. The mooring lines were set to be free in motion. The floater and turbine joints were clamped. The wave spectrum and wind function were selected as defined in Table 2.3 and Figure 2.22.

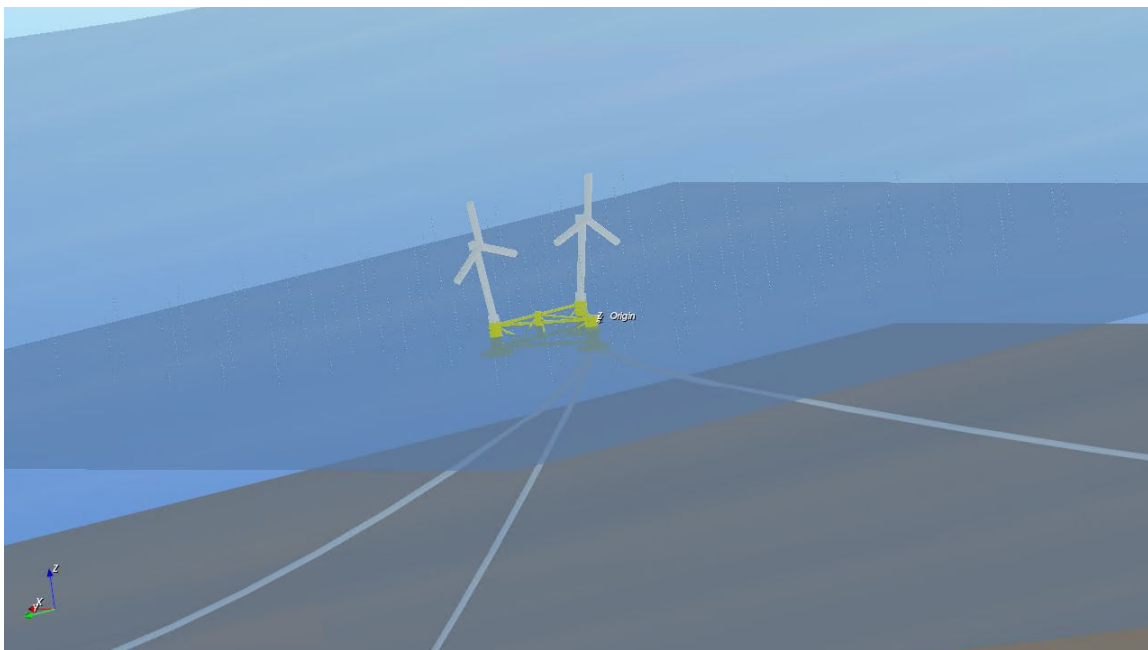
The output of OPERA simulation was saved in H5 file. The global internal loads at each section of the tower were obtained and sorted. To assess the stresses in each section of the tower and eventually the fatigue life of the FRP tower, the global internal loads were used as inputs for the developed analytical model presented in the following section.



**Table 2.4:** Loads definition on the FOWT.

Component	Load type	Remark
Floater	Gravity load	Using the floater mass
	Maneuverability load	Using the input data
	Archimedes load	Using the floater displacement
	Linear hydrostatic load	Loaded from HydroStar
	Morison elements load	Using Morison elements
	Heave plate elements load	Using heave plate elements
	First order wave load	Loaded from HydroStar
	2nd order wave load (QTF)	Loaded from HydroStar
	Linear damping load	Using damping coefficients
	Quadratic damping load	Using damping coefficients
	Relative wind drag load	Using the wind pressure on the floater
Tower	Gravity load	Using the tower mass
	Wind drag-lift load	Using the wind pressure on the tower
Blades	Gravity load	Using the blade mass
Hub	Time-series thrust	Using the time-series wind
Nacelle	Gravity load	Using the nacelle mass
Mooring lines	Gravity load	Using the mooring line mass

In OPERA, the simulation can be visualized in the post-process section in 2D and 3D. Figure 2.29 shows the FOWT platform under environmental loading. The results from the simulation will be discussed in Chapter 3.

**Figure 2.29:** 3D post-process in OPERA.

## 2.5. Analytical Formulation

This section explains the analytical formulation of a short span cylindrical tube model under global loading. The aim is to have an analytical tool to transfer the global loads from the center of the tube to the edges as line loads. These line loads will be used to obtain the stresses in the composite plies.

The cylindrical tube section considered for the analytical formulation is shown in Figure 2.30. This will allow to apply these line loads across different thicknesses along the span of a tower typically made of composite laminates. The analytical model is intended for a circular floating offshore wind turbine (FOWT) tower made in composite materials.

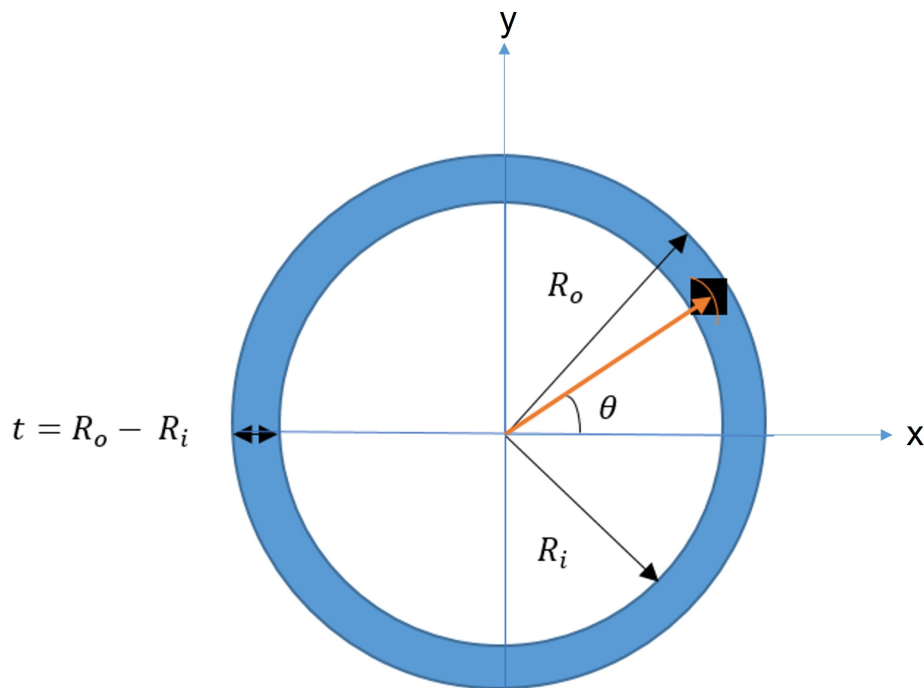


**Figure 2.30:** Cylindrical tube section.

### 2.5.1. Global loads

In this model, the global loads (see Figure 2.31) are considered to act on the center of each section of the tower as global internal loads. The load vector is expressed as:

$$\begin{Bmatrix} F_x \\ F_y \\ F_z \\ M_x \\ M_y \\ M_z \end{Bmatrix} \quad (7)$$

where:

- $F_z$  is the axial force (N).
- $F_x$  and  $F_y$  are the shear forces in (N).
- $M_z$  is the torsion in (N.mm).
- $M_x$  and  $M_y$  are the bending moments in (N.mm).

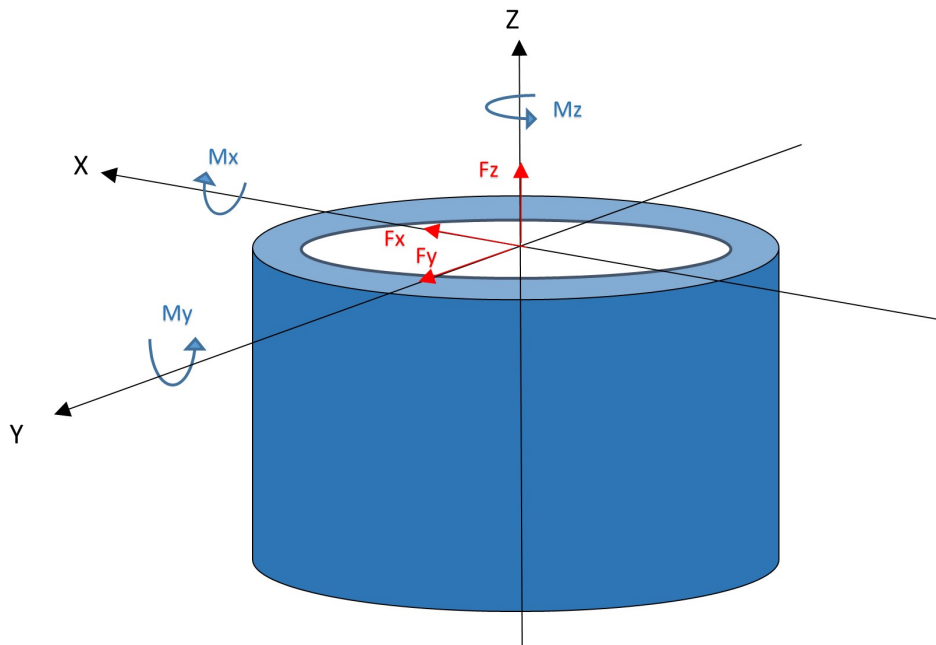


**Figure 2.31:** Cylindrical tube reference system and global loads.

### 2.5.2. Line loads

Line loads are obtained by transferring the loads from the tube center to the edges. This can be done by re-formulating the governing equation of the load with the help of mechanics of materials.

- **Axial Force:**

The axial load  $F_z$  is transferred to the edge as a line load ( $\zeta_z$ ) from the well-known normal stress ( $\sigma_{axial}$ ) formula:

$$\begin{aligned}
\sigma_{axial} &= \frac{F_z}{A} \\
\sigma_{axial} &= \frac{F_z}{\frac{\pi}{4} \times (D_o^2 - D_i^2)} \\
\sigma_{axial} &= \frac{F_z}{\frac{\pi}{4} \times (D_o - D_i) \times (D_o + D_i)} \\
\sigma_{axial} &= \frac{F_z}{\frac{\pi}{4} \times 2t \times (D_o + D_i)} \\
\sigma_{axial} \times t &= \zeta_{F_z} = \frac{2F_z}{\pi \times (D_o + D_i)}
\end{aligned} \tag{8}$$

Where:

- $A$  is the cross-sectional area of a cylindrical tube in (mm<sup>2</sup>).
- $D_o$  and  $D_i$  are the outer and internal diameters of the tube in (mm).
- $t$  is the thickness of the tube in (mm).
- $\zeta_{F_z}$  is the axial line load in (N/mm) acting on the mid-plane of the tube thickness due to the axial load  $F_z$ .

From Eq.8, it can be noted that the line load ( $\zeta_z$ ) will be constant across the cylindrical edge. In other words, the edge position with respect to the radius angle ( $\theta$ ) will have the same line load magnitude.

### • Bending Moment

The tower is subjected to global bending moments  $M_x$  and  $M_y$ . These bending moments are converted to line loads acting on the tube edge. It is known that the bending moment is maximum at the furthest point from the Neutral Axis (NA) and zero at NA. This implies that the bending stress will vary depending on the location of the studied point from the NA. To formulate this variation, the bending stress ( $\sigma_b$ ) equation is used:

$$\begin{aligned}
\sigma_b &= \frac{M_i \times y}{I} \\
\sigma_b &= \frac{M_i \times r_o \sin \theta}{\frac{\pi}{64} \times (D_o^4 - D_i^4)} \\
\sigma_b &= \frac{64 \times M_i \times D_o \sin \theta}{2 \times \pi \times (D_o^4 - D_i^4)} \\
\sigma_b \times t &= \zeta_{M_i} = \frac{32 \times M_i \times D_o \sin \theta \times t}{\pi \times (D_o^4 - D_i^4)}
\end{aligned} \tag{9}$$

Where:

- $M_i$  is the bending moment in (N.mm).
- $y$  is the vertical distance from the NA of the tube to the desired point of study in (mm).
- $i$  is the axis which the bending moment is acting about (i.e.  $M_i = M_x$  and  $M_y$ ).
- $\theta$  is the radius angle measured from the positive x-axis to the desired point at the tube edge in (degree and radian).
- $I$  is the second moment of area in (mm<sup>4</sup>).
- $\zeta_{M_i}$  is the line load due to the bending moments ( $M_x$  and  $M_y$ ).

From Eq. 9, the line load ( $\zeta_{M_i}$ ) will vary across the tube edge as a function of the radius angle ( $\theta$ ).

#### • Torsion

At each section, the tower is also under global torsion loading. To formulate this load, the cylindrical tube model is subjected to pure torsion applied at the tube center. Mathematically, the well-known shear stress ( $\tau$ ) equation is used:

$$\begin{aligned}
 \tau &= \frac{M_z \times c}{J} \\
 \tau &= \frac{M_z \times \frac{D_o + D_i}{4}}{\frac{\pi}{32} \times (D_o^4 - D_i^4)} \\
 \tau &= \frac{32 \times M_z \times (D_o + D_i)}{4 \times \pi \times (D_o^4 - D_i^4)} \\
 \tau &= \frac{8 \times M_z \times (D_o + D_i)}{\pi \times (D_o^4 - D_i^4)} \\
 \tau \times t &= \zeta_{M_z} = \frac{8 \times M_z \times (D_o + D_i) \times t}{\pi \times (D_o^4 - D_i^4)}
 \end{aligned} \tag{10}$$

Where:

- $c$  is the radius at the mid-plane of the cylinder wall thickness in (mm).
- $J$  is the second polar moment of area in (mm<sup>4</sup>).
- $\zeta_{M_z}$  is the line load due to the torsional moment ( $M_z$ ) in (N/mm).

It can be seen from Eq. 10 that the line load ( $\zeta_{M_z}$ ) will be constant across the tube edge as it does not depend on the radius angle ( $\theta$ ).

- **Shear Forces**

The global shear forces ( $F_x$  and  $F_y$ ) acting on the tower hub needs to be transferred to the edge as line loads. To derive the formula, the transverse shear stress ( $\tau_v$ ) formula is used:

$$\tau_v = \frac{V \times Q}{I \times b} = \frac{F_i \times Q}{I \times b} \quad (11)$$

Where:

- $V$  is the transverse shear force which in this case is  $F_i = F_x$  or  $F_y$  in (N).
- $Q$  is the first moment of area between the location where shear equals zero and the considered point in ( $\text{mm}^3$ ).
- $I$  second moment of area of the section defined in Eq. 9.
- $b$  is the width of the section considered at a given location in (mm).

In order to find  $Q$  and  $b$  for a tube section, the following formulation of a solid circular section is used with respect to Figure 2.32.

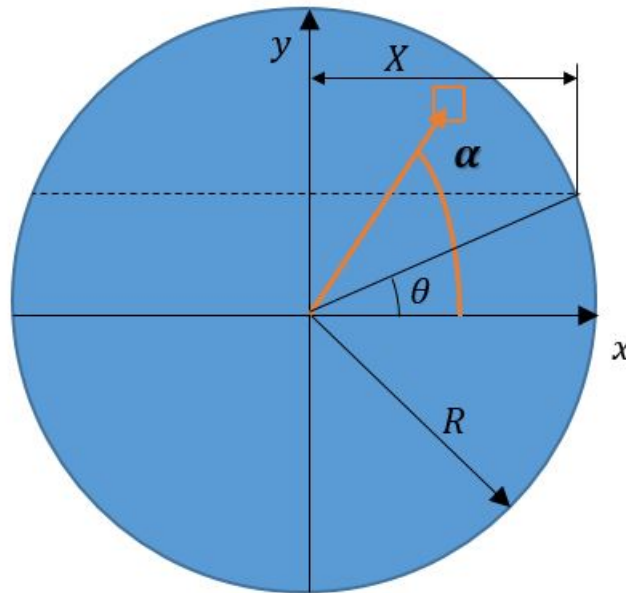


**Figure 2.32:** Solid circular section.

The first moment of area is expressed as:

$$Q = \int_S y \, ds = 2 \int_0^X \int_{R \sin \theta}^{y_{max}} y \, dy \, dx$$

$$Q = 2 \int_0^X \frac{y^2}{2} \Big|_{R \sin \theta}^{y_{max}} dx$$

With  $x = R \cos \alpha$ ,  $dx = -R \sin \alpha \, d\alpha$

$$Q = R^3 \int_0^X (\sin^2 \alpha - \sin^2 \theta) \sin \alpha \, d\alpha \quad (12)$$

With  $\sin^3 \alpha = 3 \sin \alpha - \sin 3\alpha$

And  $\cos \theta = \cos \alpha = 0 \rightarrow \theta = \alpha$

$$Q = R^3 \int_0^\theta (\sin^2 \alpha - \sin^2 \theta) \sin \alpha \, d\alpha$$

$$Q = R^3 \left( \frac{3}{4} \cos \theta - \frac{\cos 3\theta}{12} - \sin^2 \theta \cos \theta \right)$$

Similarly, the section width ( $b$ ) is computed for the solid circular section as:

$$b = 2R \cos \theta \quad (13)$$

For the tube section, Eq. 12 and 13 can be re-written in terms of the inner ( $R_i$ ) and outer radius ( $R_o$ ) and their respective inner ( $\theta_i$ ) and outer ( $\theta_o$ ) angles. Therefore, for the cylindrical tube section, the  $Q$  and  $b$  are expressed as:

$$Q = R_o^3 \left( \frac{3 \cos \theta_o}{4} - \frac{\cos 3\theta_o}{12} - \sin^2 \theta_o \cos \theta_o \right) - R_i^3 \left( \frac{3 \cos \theta_i}{4} - \frac{\cos 3\theta_i}{12} - \sin^2 \theta_i \cos \theta_i \right) \quad (14)$$

Where:

$$\begin{aligned} \theta_o &= \arcsin\left(\frac{y}{R_o}\right) \\ \theta_i &= \arcsin\left(\frac{y}{R_i}\right) \end{aligned} \quad (15)$$

And,

$$b = 2(R_o \cos \theta_o - R_i \cos \theta_i) \quad (16)$$

Now, the shear line load ( $\zeta F_i$ ) for the tube section is written in Eq. 17 by substituting Eq. 14 and 16 (assuming  $t = b/2$ ):

$$\begin{aligned}
\tau_v \times t = \zeta_{F_i} &= \frac{F_i \times Q \times t}{I \times b} \\
\zeta_{F_i} &= \frac{F_i \times Q \times b}{2I \times b} \\
\zeta_{F_i} &= \frac{F_i \times Q}{2I}
\end{aligned} \tag{17}$$

To verify Eq. 17, a point is taken at the mid-section of the cylindrical tube where the transverse shear stress is maximum. This point corresponds to ( $y = 0$  and  $\theta_o = \theta_i = 0$ ). Assuming that  $t \ll R_o$ , we obtain  $(R_o^3 - R_i^3) \rightarrow 3R^2t$  and Eq. 18 is simplified to:

$$\begin{aligned}
\tau_v &= \frac{V \times Q}{I \times b} \\
\tau_v &= \frac{\frac{4}{3}V(R_o^3 - R_i^3)}{\pi(R_o^4 - R_i^4) \times (R_o - R_i)} \\
\tau_v &= \frac{4VR^2t}{\pi(R_o^2 - R_i^2) \times (2R^2t)} \\
\tau_v &= \frac{2V}{A}
\end{aligned} \tag{18}$$

### 2.5.3. Model validation

This section demonstrates the validity of the proposed model with a case study of a short span cylindrical tube subjected to global loads. The model will be solved using the analytical formulations developed in 2.5 and validated by comparison with FEMAP software [13]. The specifications of the cylindrical tube is shown in Table 2.5 which is close to a FOWT tower application.

**Table 2.5:** Cylindrical tube specifications.

Thickness ( $t$ )	15	mm
Outer Diameter ( $D_o$ )	1015	mm
Inner Diameter ( $D_i$ )	985	mm
Span ( $H$ )	100	mm
2nd moment of area ( $I$ )	5.89E+09	mm <sup>4</sup>
2nd Polar moment of area ( $J$ )	1.18E+10	mm <sup>4</sup>
Torsion radius ( $c$ )	500	mm

The FEMAP model geometry is shown in Figure 2.33. Figure 2.34 shows the mesh of the tube model.





**Figure 2.33:** FEMAP model geometry.

The global loads in (N) defined in Eq.7 are set to the following values:

$$\begin{Bmatrix} F_x \\ F_y \\ F_z \\ M_x \\ M_y \\ M_z \end{Bmatrix} \rightarrow \begin{Bmatrix} 8000 \\ 5000 \\ 10000 \\ 15000 \\ 20000 \\ 10000 \end{Bmatrix} \quad (19)$$

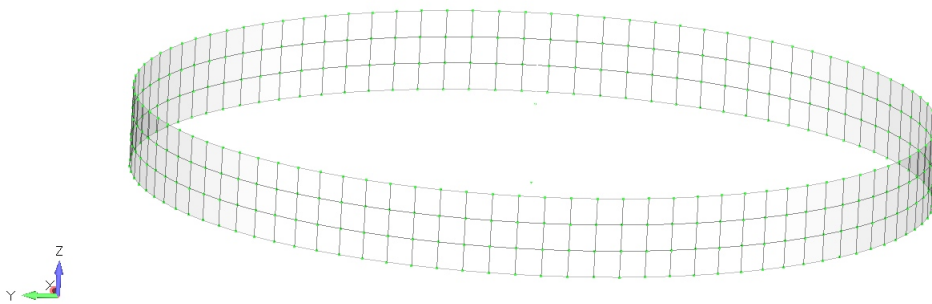


**Figure 2.34:** FEMAP model mesh.

The loads are applied separately on a middle node that is connected to the nodes at the tube edge by rigid body element (RBE3). The tube base is fixed. Figure 2.35 shows the load ( $F_z$ ) applied on the mid node and the boundary conditions at the base.

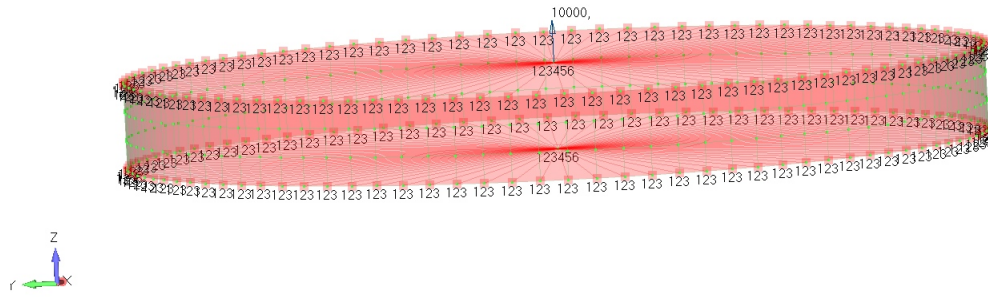


**Figure 2.35:** Loads and boundary conditions.

The values in Table 2.5 and Eq. 19 are substituted in Eq. 8, 9 and 10 and used also for in the FEMAP model. For demonstration, the axial load case will be used to showcase the results in the FEMAP model. Other line loads are shown in Appendix A. Figure 2.36 shows the line loads values in the FEMAP model for the axial load ( $F_z$ )

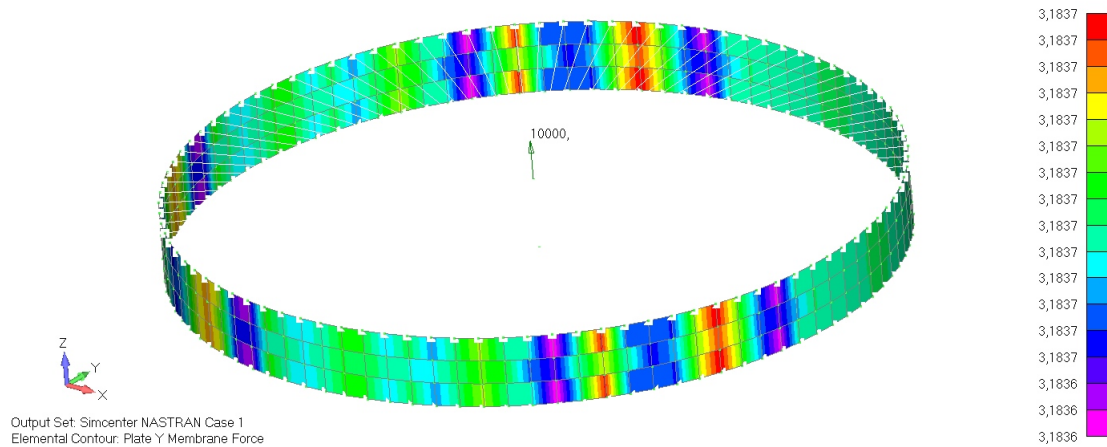


**Figure 2.36:** FEMAP Axial line load ( $\zeta_z$ ) due to  $F_z$ .

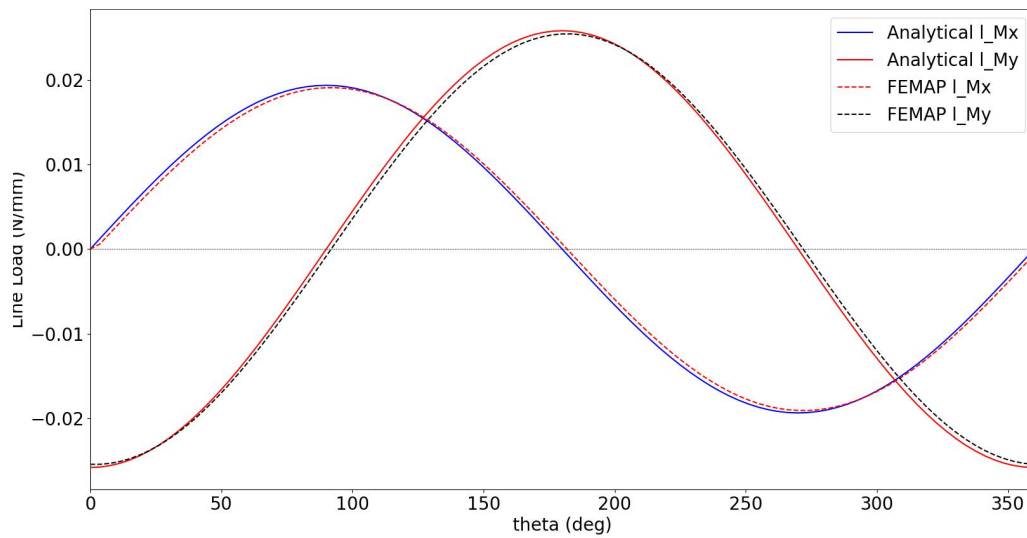
The values for the constant line loads ( $\zeta_z$  and  $\zeta_{Mz}$ ) are shown in Table 2.6. It can be seen that the analytical model is in good agreement with the FEMAP model with maximum difference of 0.07%.

**Table 2.6:** Axial and torsion line loads.

Load	Analytical (N/mm)	FEMAP (N/mm)	Difference (%)
$\zeta_{Fz}$	3.1831	3.1837	0.02
$\zeta_{Mz}$	0.006365	0.006369	0.07

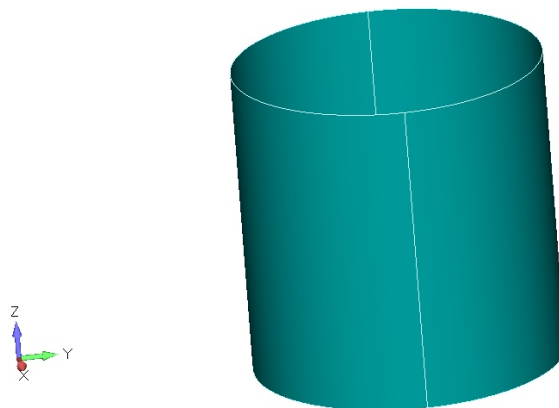
For bending ( $\zeta_{Fi}$ ) and shear ( $\zeta_{Mi}$ ) line loads, there is variation in magnitude with respect to the radius angle ( $\theta$ ).

Figure 2.37 and 2.40 show the line load variation across the tube radius angle. The bending line load for the analytical model yielded the same values as the FEMAP model with being more conservative at the maximum angles and their reverse ( $90^\circ$  for  $M_x$ ) and ( $180^\circ$  for  $M_y$ ). These results are logical from mechanics of materials point of view where the maximum bending stress occurs at the point further from the Neutral Axis (NA) and zero at the NA which corresponds to angles ( $0^\circ$ ,  $180^\circ$  and  $360^\circ$ ) for  $M_x$  and shifted  $90^\circ$  for  $M_y$ .



**Figure 2.37:** Bending line loads.

In order to validate the shear line loads, the FEMAP model in Figure 2.33 is modified. The height of the cylindrical tube is scaled 10 times to ensure the load obtained on the element at the mid section are due to the influence of the shear forces ( $F_x$  and  $F_y$ ) only without boundary conditions effects. The top of the cylinder is fixed to ensure there is no displacement in the Z direction. Figure 2.38 shows the model after modification.



**Figure 2.38:** FEMAP model geometry for shear line loads.

The mesh, shear loads and boundary conditions are shown in Figure 2.39. The FEMAP simulation results for the shear forces ( $F_x$  and  $F_y$ ) are shown in Appendix A.

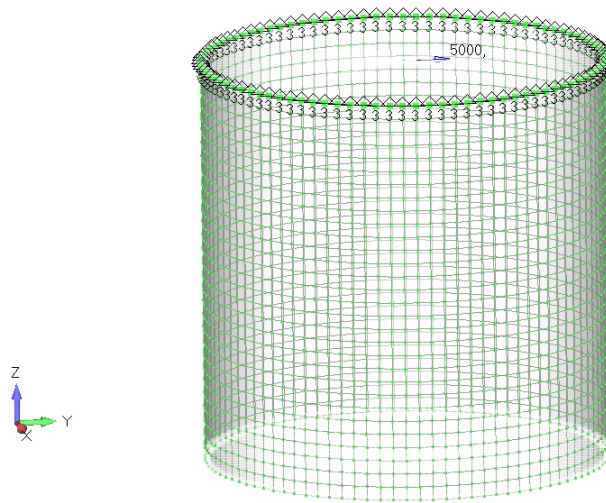


**Figure 2.39:** FEMAP model mesh for shear line loads.

The analytical shear line loads are in agreement with FEMAP results as shown in Figure 2.40 with the analytical model being slightly more conservative. For  $\zeta_{F_x}$ , the maximum value will occur at the NA which correspond to  $90^\circ$  and  $270^\circ$  angles where the first moment of area  $Q$  is maximum. Similarly  $\zeta_{F_y}$  has the maximum value at  $0^\circ$  and  $180^\circ$ . There is a discontinuity when the line loads cross zero axis, this is due to the way  $Q$  is computed in Eq. 14. When  $R_i$  in Eq. 15 reaches an angle  $\theta_i$  where it is more than or equal the value of  $y$ , the value of  $\theta_i$  become not defined. This point is where  $Q$  reaches zero with small value of shear line loads.

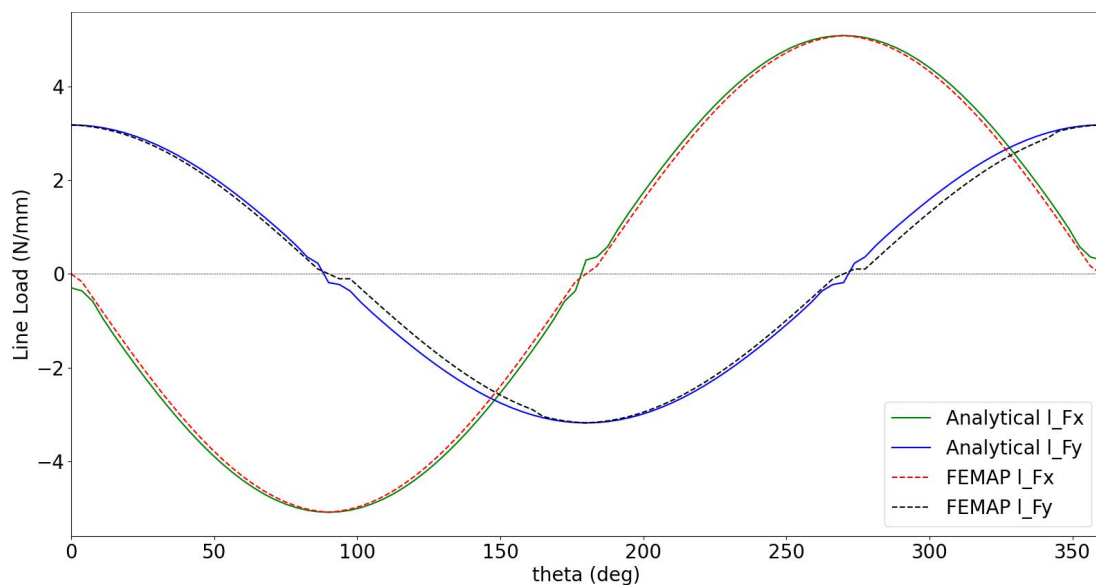
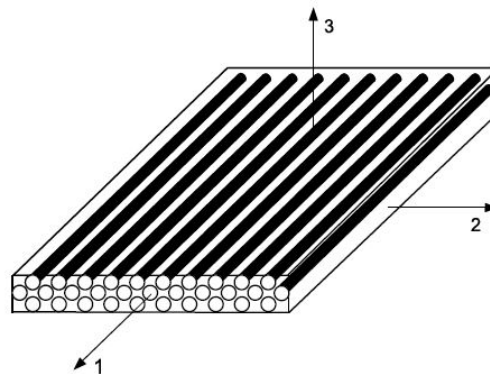


**Figure 2.40:** Shear line loads.

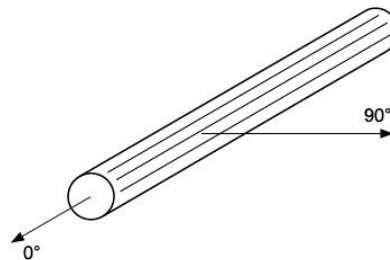
## 2.6. Macro-mechanical Analysis

A composite laminate is made of a combination of several layers stacked to each other. Each individual layer (lamina) has a specific material, angle of orientation with respect to a global axes and location across its thickness. BV-NR-546 [16] is followed to develop the macro-mechanical analysis of the laminate in Python script. Figure 2.41 shows the reference axis system of a unidirectional layer and Figure 2.42 the reference system of a single fibre [16]. In this thesis our interest will be focused on unidirectional fibre plies for further analysis in upcoming sections.



- 1 : Axis parallel to the fibre direction
- 2 : Axis perpendicular to the fibre direction
- 3 : Axis normal to the plane containing axes 1 and 2, leading to the direct reference axis system.

**Figure 2.41:** Reference axis system of a unidirectional layer.



- 0° : Longitudinal axis of the fibre
- 90° : Transverse axis of the fibre.

**Figure 2.42:** reference system of a single fibre.

### 2.6.1. Fibre and resin characteristics

The raw material properties for various types of fibres and resins are used as inputs to the python script according to Table 1 and 2, section 4 in BV-NR-546 [16]. The resin and fibre elastic coefficients are calculated at each axes for a unidirectional fibre ply according to Figure 2.41. In addition, the elastic coefficients are computed for other types of fibres including woven roving (WR) and chopped standard mat (CSM). The breaking stresses and strains are computed.

### 2.6.2. Ply definition

A ply is defined by the type of resin and fibre used, percentage of fibre in volume or mass, type of ply whether it is (UD), (CSM) or (WR) and the orientation of the fibres. Other characteristics are computed and it can be found in details referring to section 5 in BV-NR-546 [16].

- **In-plane rigidity of a ply**

The aim of our analysis is to obtain the stresses at the local plane in each ply. These ply stresses are computed using the following expression:

$$[\sigma]_{1,2} = [\bar{R}] [\varepsilon]_{1,2} \quad (20)$$

$$\begin{pmatrix} \sigma_1 \\ \sigma_2 \\ \tau_{12} \end{pmatrix} = \begin{pmatrix} \bar{R}_{11} & \bar{R}_{12} & 0 \\ \bar{R}_{21} & \bar{R}_{22} & 0 \\ 0 & 0 & \bar{R}_{33} \end{pmatrix} \begin{pmatrix} \varepsilon_1 \\ \varepsilon_2 \\ \gamma_{12} \end{pmatrix} \quad (21)$$

Where:

- $[\sigma]_{1,2}$  is the vector of in-plane stresses.
- $[\bar{R}]$  is the in-plane rigidity matrix where  $R_{11}$ ,  $R_{22}$ ,  $R_{12}$ ,  $R_{21}$  and  $R_{33}$  are computed according to Table 3, section 5 in BV-NR-546 [16]
- $[\varepsilon]_{1,2}$  is the vector of in-plane strains.

Moreover, the in-plane theoretical individual layer breaking stresses are computed according to section 5.5 in BV-NR-546 [16]. The values of coefficients needed in their computation are imported as inputs to the Python script.

### 2.6.3. Laminate characteristics and analysis

This section outlines the process for calculating the characteristics of a laminate, including its geometric parameters and elastic coefficients. This involves determining the position and orientation of each individual layer in relation to the overall laminate, as well as calculating the laminate's global elastic coefficients and mechanical characteristics. External loads applied to the panel are also taken into account. The laminate's median plane deformations, strains, and stresses are then calculated for each individual layer in both the panel's global axes and the layer's own local axes.

The characteristics considered are based on the properties of each layer, its position within the laminate thickness, and its orientation with respect to the global axes of the laminate. The position of each layer is shown in Figure 2.43 [16], with reference to the median plane of the laminate ( $AP$ ), the overall thickness of the laminate ( $th$ ), the thickness of

each individual layer ( $e_k$ ), and the distance between the median plane and the interfaces between adjacent layers ( $Z_k$  and  $Z_{k-1}$ ).

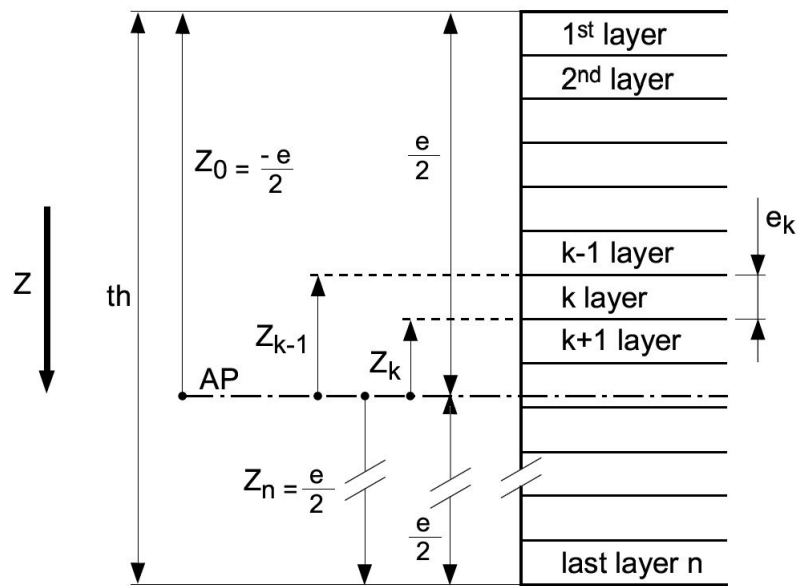


**Figure 2.43:** Individual layers position.

Figure 2.44 defines the orientation between the local axes of each individual layer and the global axes of the laminate [16]. The global axes of the laminate are usually chosen to be similar to the reference axes of the ship or any panel, with the X axis being the longitudinal axis and the Y axis being perpendicular to the longitudinal axis in the laminate plane. The angle  $\theta$  is considered positive from the global axes to the local axes, as illustrated in Figure 2.44.

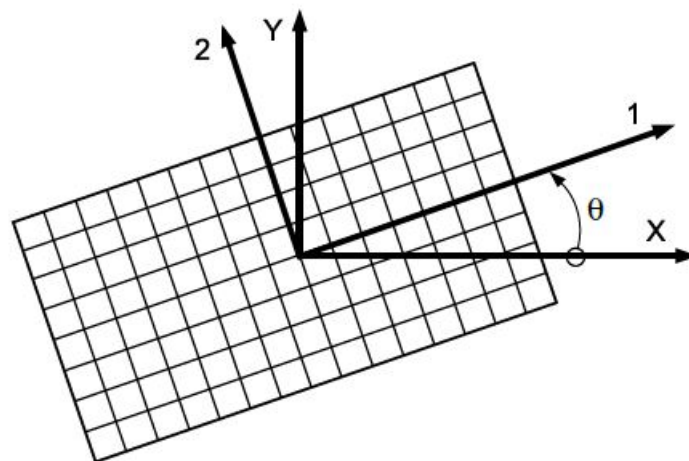


**Figure 2.44:** Individual layers orientation to the laminate global axis.

The rigidity matrix  $[R]$  defined in Eq. 21 is oriented to the global laminate axes using the following expression:

$$\{R\}_K = \begin{Bmatrix} R_{XX} & R_{XY} & R_{XZ} \\ R_{YX} & R_{YY} & R_{YZ} \\ R_{ZX} & R_{ZY} & R_{ZZ} \end{Bmatrix}_k = T [\bar{R}]_k T^{-1} \quad (22)$$

where  $T$  is the transformation matrix and  $T^{-1}$  is the transpose of the inverse of  $T$ . Those matrices are defined in [16]. Other characteristics that define a laminate like the laminate weight, elastic coefficients and Poisson ratios, laminate neutral axis position and laminate bending rigidity are calculated in the Python script according to section 6.2 in BV-NR-546 [16]. The [ABBD] global rigidity matrix is defined as follows:

$$\begin{Bmatrix} A & B \\ B & D \end{Bmatrix} = \begin{Bmatrix} A_{ij} & B_{ij} \\ B_{ij} & D_{ij} \end{Bmatrix} \quad (23)$$

Where:

- $A_{ij}$  is the tensile rigidity matrix with size of  $[3 \times 3]$ . Defined as:

$$A_{ij} = \sum_1^n (R_{ij})_k \cdot e_k \quad (24)$$

- $B_{ij}$  is the tensile and bending coupling effect matrix with size of  $[3 \times 3]$ . In case the laminate has symmetrical layers this matrix has zero values.

$$B_{ij} = \frac{1}{2} \cdot \sum_1^n (R_{ij})_k \cdot (Z_k^2 - Z_{k-1}^2) \quad (25)$$

- $D_{ij}$  is the bending rigidity matrix with size of  $[3 \times 3]$ .

$$D_{ij} = \frac{1}{3} \cdot \sum_1^n (R_{ij})_k \cdot (Z_k^3 - Z_{k-1}^3) \quad (26)$$

Therefore, the reverse global rigidity matrix is defined as:

$$\begin{Bmatrix} A & B \\ B & D \end{Bmatrix}^{-1} = \begin{Bmatrix} A' & B' \\ B' & D' \end{Bmatrix} \quad (27)$$

#### 2.6.4. Laminate behaviour under global and local loads

This section outlines the behavior of a laminate and the distribution of strains and stresses in each layer under bending moments ( $M_i$ ), shear forces ( $T_i$ ), and in-plane forces ( $N_i$ ), as depicted in Figure 2.45 [16]. It is worthy to note that the bending moments ( $M_i$ ) are local bending moments and not the global bending moments defined in Section 2.5.1.



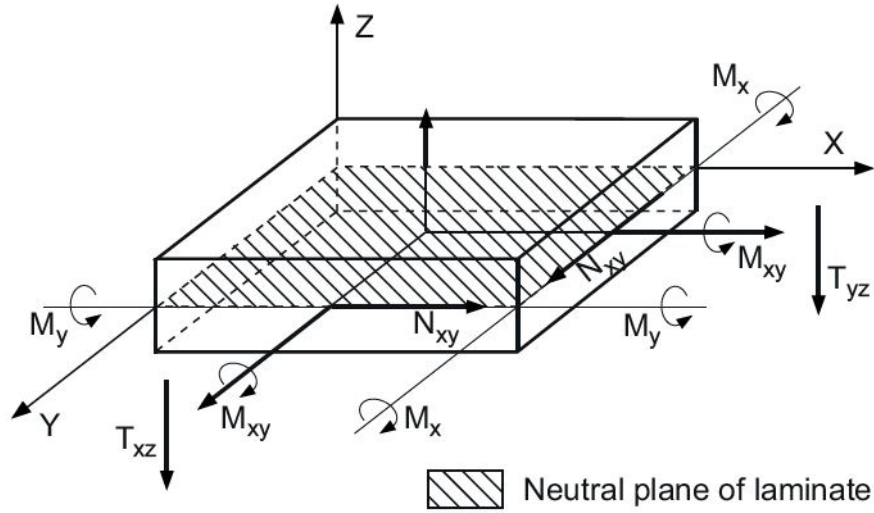


**Figure 2.45:** Laminate under forces and moments.

Bending moments ( $M_x$ ) and ( $M_y$ ) result from local loads applied perpendicularly to the laminate plane, while bending moment ( $M_{xy}$ ) results from a local torsional moment around axes parallel to the laminate plane, which is generally zero [16]. Shear forces ( $T_{xz}$ ) and ( $T_{yz}$ ) arise from local loads applied perpendicular to the laminate plane. In-plane tensile or compression forces, ( $N_x$ ) and ( $N_y$ ), and in-plane shear force ( $N_{xy}$ ) arise from global hull girder longitudinal loads or from global transverse loads [16].

In this thesis, ( $N_x$ ), ( $N_y$ ) and ( $N_{xy}$ ) are the line loads developed in Section 2.5.2. They arise due to the internal global loads at the FOWT tower sections as defined in Section 2.5.1. If the laminate is evaluated under local external pressure only,  $N_x$ ,  $N_y$ , and  $N_{xy}$  are considered zero [16]. The line loads are summed based on their direction of application as in-plane line loads expressed as:

$$N_x = \zeta_{M_x} + \zeta_{M_y} + \zeta_{F_z} \quad (28)$$

$$N_{xy} = \zeta_{F_x} + \zeta_{F_y} + \zeta_{M_z} \quad (29)$$

- **Laminate global deformation**

The deformations of the laminate median plane are obtained using the following expression:

$$\begin{pmatrix} \varepsilon_x^0 \\ \varepsilon_y^0 \\ \varepsilon_{xy}^0 \\ K_x \\ K_y \\ K_{xy} \end{pmatrix} = \begin{pmatrix} A & B \\ B & D \end{pmatrix}^{-1} \begin{pmatrix} N_x \\ N_y \\ N_{xy} \\ M_x \cdot 10^{-3} \\ M_y \cdot 10^{-3} \\ M_{xy} \cdot 10^{-3} \end{pmatrix} \quad (30)$$

where:

- $\varepsilon_x^0$  and  $\varepsilon_y^0$  are compression or tensile strains of the laminate mid-plane in X and Y directions, respectively.
- $\gamma_{xy}^0$  is the shear strain in the XY plane at the laminate mid-plane.
- $K_x$  and  $K_y$  are the curved deformations of the laminate mid-plane around X and Y axis, respectively.
- $K_{xy}$  is the twist deformation of the laminate mid-plane around X and Y axis.
- $N_i$  and  $M_i$  are the line loads in-plane forces and bending moments, respectively.

- **Layer deformation in global axes**

The global deformations of the laminate defined in Eq. 30 is used to obtain the local strains in each individual layer at the layer mid thickness in the laminate global reference system X and Y. The following formula shows the relation:

$$\begin{pmatrix} \varepsilon_x \\ \varepsilon_y \\ \gamma_{xy} \end{pmatrix}_k = \begin{pmatrix} \varepsilon_x^0 \\ \varepsilon_y^0 \\ \gamma_{xy}^0 \end{pmatrix} + \begin{pmatrix} K_x \\ K_y \\ K_{xy} \end{pmatrix} \cdot \frac{Z_k + Z_{k-1}}{2} \quad (31)$$

where  $\varepsilon_x$ ,  $\varepsilon_y$  and  $\gamma_{xy}$  are the in-plane strains of each ply.

- **Layer deformation and stresses in local axes**

For each layer, the in-plane strains  $\varepsilon_1$ ,  $\varepsilon_2$  and  $\gamma_{12}$  are obtained at the layer mid-thickness in the local reference system of the layer as follows:

$$\begin{pmatrix} \varepsilon_1 \\ \varepsilon_2 \\ \gamma_{12} \end{pmatrix}_k = T'^{-1} \cdot \begin{pmatrix} \varepsilon_x \\ \varepsilon_y \\ \gamma_{xy} \end{pmatrix}_k \quad (32)$$

where  $T'^{-1}$  is defined in [16]. The local stresses  $\sigma_1$ ,  $\sigma_2$  and  $\tau_{12}$  are computed at the layer mid-thickness for each ply as follows:

$$\begin{Bmatrix} \sigma_1 \\ \sigma_2 \\ \tau_{12} \end{Bmatrix}_k = [\bar{R}] \cdot \begin{Bmatrix} \varepsilon_1 \\ \varepsilon_2 \\ \gamma_{12} \end{Bmatrix}_k \quad (33)$$

where  $[\bar{R}]$  is the in-plane rigidity matrix of a ply as defined in Eq. 21.

### 2.6.5. Python tool validation

The macro-mechanical analysis in Section 2.6 is coded in a Python script to obtain the stresses at each layer. The Python tool then is checked with BV ComposeIT software [15] to ensure the validity of the Python tool. In this section a case study is shown to demonstrate the validity of the Python tool which is intended to be used in upcoming sections for the fatigue analysis of the FOWT tower.

The python tool uses the line loads developed in Section 2.5.2 as an input and the type of fibre and resin chosen to be studied. In this demonstration, the fibre type will chosen as HS carbon and the resin type is Epoxy with mechanical properties shown in Table 2.7. Other parameters are taken from Section 4 in BV-NR-546 [16] for the ply calculation.

**Table 2.7:** Fibre and resin mechanical properties.

	Epoxy	HS Carbon
$\rho$	1.25	1.79
$E$ (N/mm <sup>2</sup> )	3100	$E_{0^\circ} = 238000$ $E_{90^\circ} = 15000$
$G$ (N/mm <sup>2</sup> )	1500	50000
$\nu$	0.39	0.3

A Carbon-Epoxy unidirectional ply is created in the Python tool and in ComposeIT software with a fibre volume fraction of 60%. Table 2.8 shows the UD layer characteristics.

**Table 2.8:** UD Layer Characteristics.

	ComposeIT	Python	Difference (%)
Fibre mass/m <sup>2</sup> (g/m <sup>2</sup> )	300	299.646	0.1
Resin mass/m <sup>2</sup> (g/m <sup>2</sup> )	139.66	139.5	0.1
Mass/m <sup>2</sup> (g/m <sup>2</sup> )	439.66	439.146	0.1
Thickness (mm)	0.279	0.279	0.0
Density	1.574	1.574	0.0

The elastic coefficients for the UD individual layer are computed in both software and shown in Table 2.9.

**Table 2.9:** UD Elastic Coefficients (MPa).

	ComposeIT	Python	Difference (%)
E1	144040	144040	0
E2	7198	7198	0
E3	7198	7198	0
G12	4858	4858	0
G13	4858	4858	0
G23	3400	3400	0
$\nu_{12}$	0.269	0.269	0
$\nu_{21}$	0.013	0.013	0

In addition, the breaking stresses for the UD ply is shown in Table 2.10.

**Table 2.10:** UD Breaking Stresses (MPa).

	ComposeIT	Python	Difference (%)
$\sigma_{brt1}$	1728.48	1728.48	0
$\sigma_{brc1}$	1224.34	1224.34	0
$\sigma_{brt2}$	71.98	71.98	0
$\sigma_{brc2}$	165.55	165.55	0
$\tau_{br12}$	77.72	77.72	0
$\tau_{IL1}$	64.61	64.61	0
$\tau_{IL2}$	77.72	77.72	0

In order to validate the laminate properties, a laminate of 4 plies is created. Table 2.11 shows the definition of the laminate used in both ComposeIT and Python.

**Table 2.11:** Laminate definition.

Layer	Type	Angle (°)	Thickness (mm)
1	UD	0	0.28
2	UD	90	0.28
3	UD	90	0.28
4	UD	0	0.28

The laminate global results are shown in Table 2.12.

**Table 2.12:** Laminate global results.

	ComposIT	Python	Difference (%)
Thickness (mm)	1.12	1.116	0.36
$E_x$ (MPa)	75843	75843	0.00
$E_y$ (MPa)	75843	75843	0.00
$G_{xy}$ (MPa)	4858	4858	0.01
$EI_x$ (N.mm <sup>2</sup> /mm)	14790	14738	0.35
$EI_y$ (N.mm <sup>2</sup> /mm)	2832	2822	0.35
$\nu_x$	0.026	0.026	0.00
$\nu_y$	0.026	0.026	0.00
Weight (kg/m <sup>2</sup> ):	1.759	1.757	0.14
Density (g/cm <sup>3</sup> ):	1.57	NA	-
Resin weight (kg/m <sup>2</sup> ):	0.559	NA	-
Fibre weight (kg/m <sup>2</sup> ):	1.2	NA	-
$V_x$ (mm):	0.559	-	-
$V_y$ (mm):	0.559	-	-

where  $V_x$  and  $V_y$  are the laminate neutral axis positions and  $EI_x$  and  $EI_y$  are the laminate bending rigidity in X and Y directions, respectively.

Finally, the [ABBD] matrix defined in Eq. 23 is computed in the both software and compared and are shown in Eq. 34 for ComposeIT and Eq. 35 for Python.

$$\begin{Bmatrix} A & B \\ B & D \end{Bmatrix} = \begin{pmatrix} 84797 & 2170 & 0 & 0 & 0 & 0 \\ 2170 & 84797 & 0 & 0 & 0 & 0 \\ 0 & 0 & 5427 & 0 & 0 & 0 \\ 0 & 0 & 0 & 14808 & 226 & 0 \\ 0 & 0 & 0 & 226 & 2835 & 0 \\ 0 & 0 & 0 & 0 & 0 & 565 \end{pmatrix} \quad (34)$$

$$\begin{Bmatrix} A & B \\ B & D \end{Bmatrix} = \begin{pmatrix} 84697 & 2167 & 0 & 0 & 0 & 0 \\ 2167 & 84697 & 0 & 0 & 0 & 0 \\ 0 & 0 & 5421 & 0 & 0 & 0 \\ 0 & 0 & 0 & 14756 & 225 & 0 \\ 0 & 0 & 0 & 225 & 2825 & 0 \\ 0 & 0 & 0 & 0 & 0 & 563 \end{pmatrix} \quad (35)$$

Referring to Eq. 34 and Eq. 35, the maximum deviation of the values is around 0.48% mainly due to the rounding errors which shows the validity of the developed Python tool.

Moreover, as expected, the B matrix in Eq. 34 and Eq. 35 has zero values due to symmetry of the composite layers.

To obtain the stresses in each ply as defined in Eq. 33, Eq. 30 needs to be solved. To demonstrate the validity of the python tool, the values of the line load vector is assigned as follows:

$$\begin{pmatrix} N_x \\ N_y \\ N_{xy} \\ M_x \cdot 10^{-3} \\ M_y \cdot 10^{-3} \\ M_{xy} \cdot 10^{-3} \end{pmatrix} = \begin{pmatrix} 0 \\ 1000 \\ 0 \\ 0 \\ 0 \\ 0 \end{pmatrix} \quad (36)$$

where  $N_y$  is in N/mm or KN/m. Assigning the line load vector defined in Eq. 36 in Python tool and ComposeIT, Eq. 30 is solved by substituting the ABBD matrix defined in Eq. 35 and Eq. 34 and the stresses at each ply are computed and compared. Table 2.13 shows the results of the ply stresses at its local axis obtained from ComposeIT and Python.

**Table 2.13:** Ply stresses at its local axis (MPa).

Layer	ComposeIT	Python	Difference (%)
$\sigma_1$			
1	-20.7	-20.8	0.28
2	1705	1707	0.14
3	1706	1707	0.08
4	-20.7	-20.8	0.28
$\sigma_2$			
1	84.7	84.8	0.07
2	20.7	20.8	0.28
3	20.7	20.8	0.28
4	84.7	84.8	0.07
$\tau_{12}$			
1	0	0	0
2	0	0	0
3	0	0	0
4	0	0	0

Referring to Table 2.13,  $\sigma_1$  has negative value in the first and last layer ( $\theta = 0^\circ$ ) which implies the fibres are in compression since they are perpendicular to the line load ( $N_y$ ). However, for the second and third layers, the fibres are taking the load since they are

facing the line load direction (parallel to load direction). For  $\sigma_2$ , the opposite is happening since the fibres are transverse to the load in the first and last layer, hence, the load is taken by the resin. Also, the values in the mid layers are less, since the load is taken by the fibre. For the in-plane shear stress ( $\tau_{12}$ ), the values are zero since the laminate is loaded only with in-plane tensile line load ( $N_y$ ). The python tool was also validated using more complex laminates with  $45^\circ/-45^\circ/0^\circ/90^\circ$  plies. However, the results are not demonstrated in the thesis. The results were also in agreement with ComposeIT [15].

## 2.7. Fatigue Analysis

In this section, the analytical formulation developed in Section 2.5 and the macro-mechanical analysis in Section 2.6 will be used. The aim is to obtain the ply stresses at their local axis ( $\sigma_1$ ,  $\sigma_2$  and  $\tau_{12}$ ) with respect to time.

The global loads defined in Section 2.5.1 are coming from the multi-physics software OPERA [18]. The outputs from OPERA are forces ( $F_x$ ,  $F_y$  and  $F_z$ ) and moments ( $M_x$ ,  $M_y$  and  $M_z$ ) spectra dependent on time at a given section (i.e. at the tower base). This will make the line loads vector defined in Section 2.5.2 dependent on time as well.

Since the line loads vector in Eq. 30 now is dependent on time, the global deformations all the way to the ply stresses will also be a function of time. The matrix size of the ply stresses depends on the number of plies at the studied tower section and the time step used in the global load history from OPERA. The matrix size of the ply stresses at its local axis will be  $[k \times 3n]$ .

Where:

- $k$  is the number of plies at the tube section.
- $n$  is the time vector size.
- 3 for 3 ply stresses ( $\sigma_1$ ,  $\sigma_2$  and  $\tau_{12}$ ) at each time step ( $\Delta t$ ).

The Python tool developed in Section 2.6.5 will be extended to include time-dependent line loads. This is done by changing the line load vector in Eq. 30 to a matrix where its columns indicate the line loads at each time step.

The analytical formulation in Section 2.5 is coded in Python script. The Python code reads the global forces and moments load spectra and convert them to time-dependent line loads. The Python script is customized to create line loads matrix depends on the desired number of plies and radius angle of interest. This allows creation of multiple load cases which each is evaluated using Eq. 30 and eventually obtaining the ply time-dependent

stresses. The process can be repeated for different sections at the tower span to obtain different global loads from OPERA. Figure 2.46 shows the proposed methodology flow chart for the fatigue analysis.

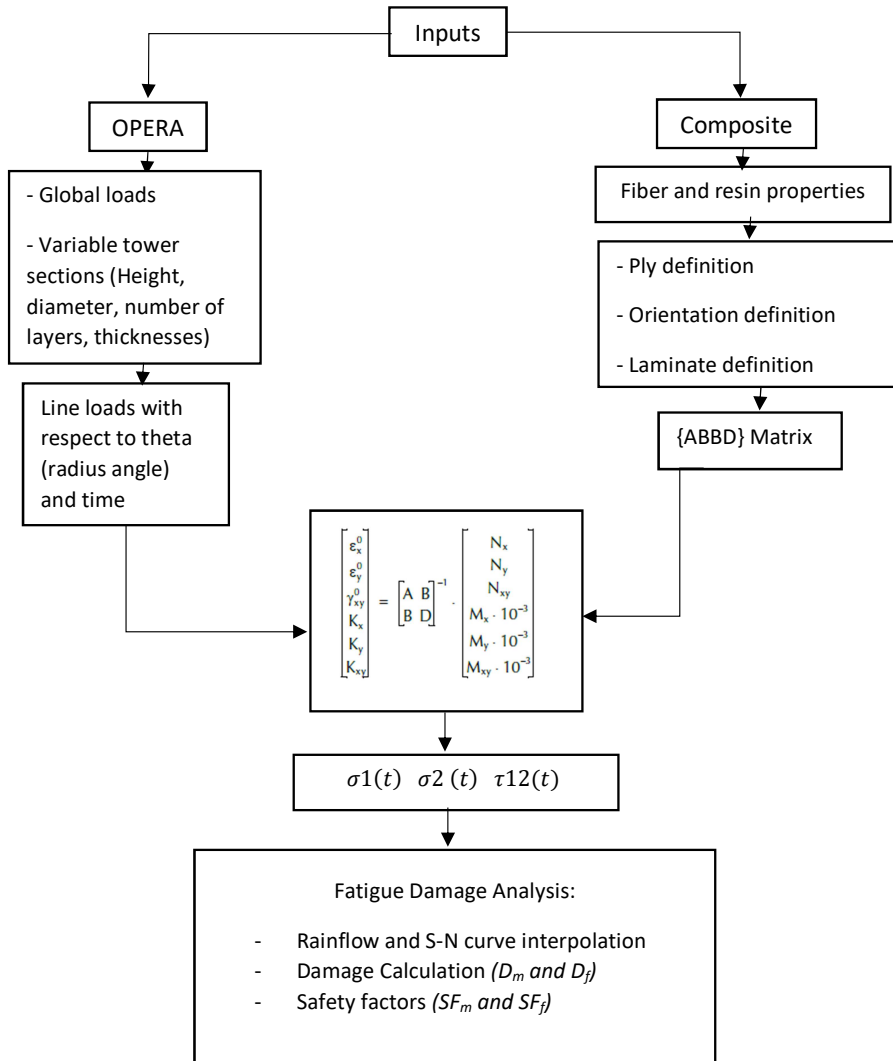


**Figure 2.46:** Fatigue analysis flowchart.

The stress history for the ply  $\sigma_1(t)$ ,  $\sigma_2(t)$  and  $\tau_{12}(t)$  are studied for the fatigue damage using BV-Composite fatigue Guidelines [21].

### 2.7.1. Fatigue damage analysis

In this section, the fatigue methodology of BV-Composite fatigue guidelines [21] is presented. The aim of this guideline is to offer instructions on how to evaluate the fatigue of composites materials and propose a method for calculating their fatigue life. The focus is on polymer matrix composites that are reinforced with continuous fibres. The guidance outlines recommendations for fatigue analysis using S-N curves and a Constant Fatigue Life (CFL)



diagram, but only when cracks are not taken into account.

In this methodology, a detailed ply-by-ply analysis is required for static calculations as defined in Section 2.6 according to NR546 BV Rules for Composite Materials. Figure 2.47 shows the methodology flowchart of BV-Composite fatigue guidelines [21]. The process involves determining the local stress state of each layer, denoted as  $\sigma = [\sigma_1, \sigma_2, \tau_{12}]$ . The direction 1, 2, and 3 are defined in Figure 2.41, and the terms  $\sigma_1, \sigma_2$  and  $\tau_{12}$  represent the stress in the fibre direction, stress in the direction perpendicular to the fibre, and in-plane shear stress, respectively. These ply local stresses are extended to be time-dependent.

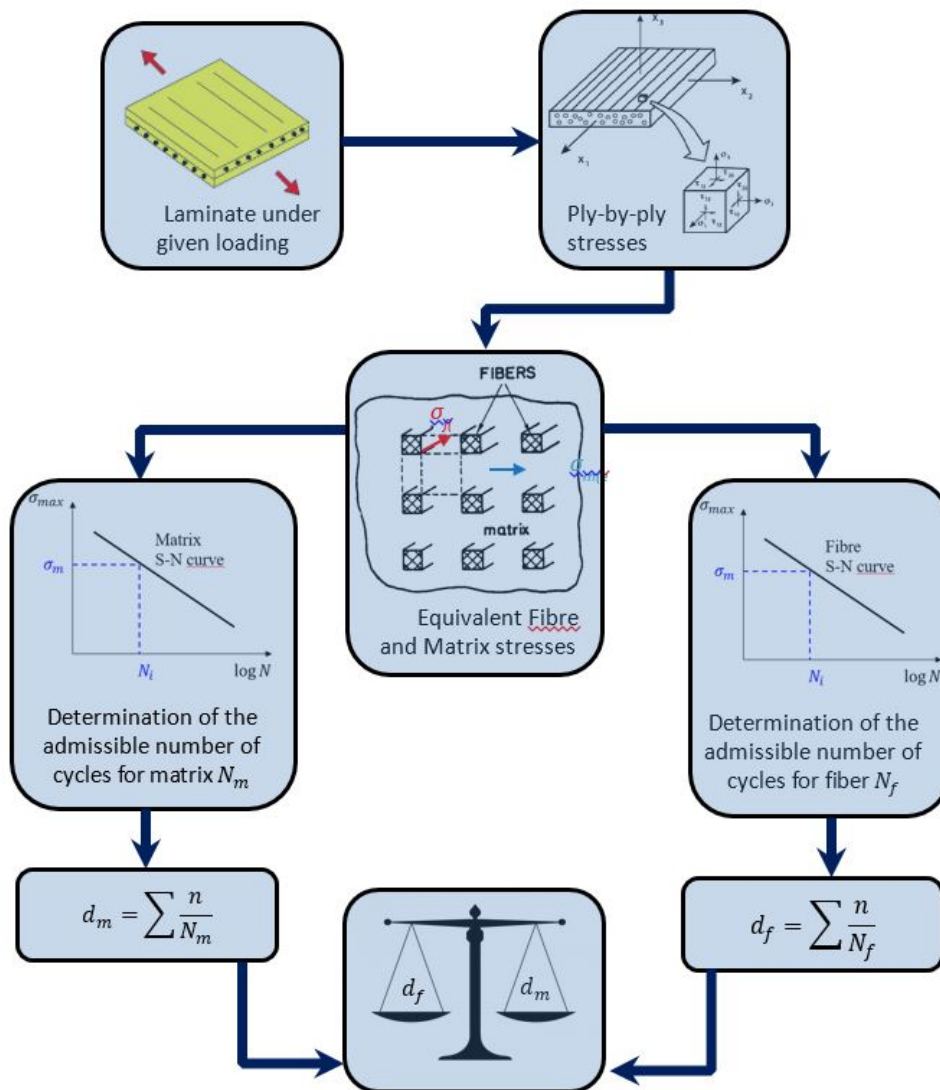


Figure 2.47: Fatigue life evaluation using UD S-N curves.

- **Fibre and matrix stresses**

Since the fatigue behaviour in the fibre and matrix are assumed to be different, the ply local stresses are decomposed into fibre and matrix stresses. The equivalent fibre and matrix stresses are expressed as:

$$\sigma_f = \sigma_1 \quad (37)$$

Where:  $\sigma_f$  is the equivalent fibre stress taken equal to the stress along direction 1 and therefore,  $\sigma_2$  and  $\tau_{12}$  are neglected.

$$\sigma_m = \sqrt{\sigma_2^2 + (f_2 \tau_{12})^2} \quad (38)$$

where:

- $\sigma_m$  is the equivalent matrix stress that takes into account the transverse stress  $\sigma_2$  and in-plane shear stress  $\tau_{12}$ .

$$f_2 = \begin{cases} \frac{\sigma_{brt2}}{\tau_{br12}}, & \text{if } \sigma_2 \geq 0 \\ \frac{\sigma_{brc2}}{\tau_{br12}}, & \text{if } \sigma_2 < 0 \end{cases}$$

- where:  $\sigma_{brt2}$ ,  $\sigma_{brc2}$  and  $\tau_{br12}$  are the theoretical breaking stresses in the transverse direction as defined in BV NR546 [16] and shown in Table 2.10.

#### • Rainflow Algorithm

The matrix and fibre stresses are in function of time. The stress history load has irregular signal with variable peaks and valleys. The fatigue damage assessment works with regular signal with constant amplitude and cycles. Therefore, Rainflow algorithm is used to obtain constant stress amplitudes for certain cycles, Figure 2.48 [22].

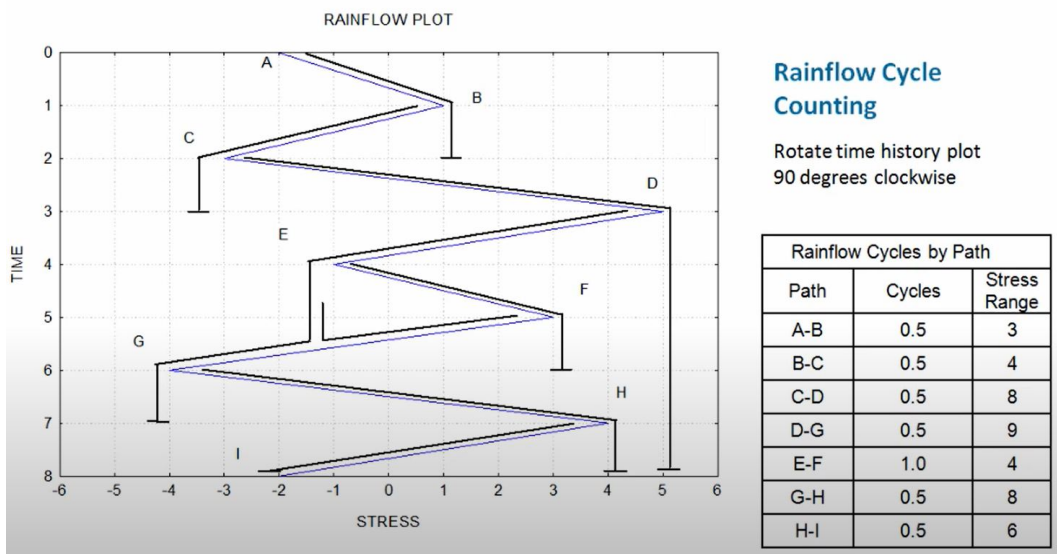


**Figure 2.48:** Rainflow algorithm.

There are certain parameters extracted from rainflow algorithm including:

- Stress range is the difference between the maximum and minimum stress.

$$\Delta\sigma = \sigma_{max} - \sigma_{min} \quad (39)$$

- The number of cycles ( $n$ ) for each stress range ( $\Delta\sigma$ ).
- The mean stress of the cycle ( $\sigma_{mean}$ ).

Other parameters are calculated such as:

- The alternate stress of the cycle is expressed as:

$$\sigma_{alternate} = \frac{\Delta\sigma}{2} \quad (40)$$

- The maximum stress ( $\sigma_{max}$ ) of the cycle is computed using:

$$\sigma_{max} = \sigma_{alternate} + \sigma_{mean} \quad (41)$$

- Similarly, the minimum stress ( $\sigma_{min}$ ) of the cycle is calculated using:

$$\sigma_{min} = \sigma_{mean} - \sigma_{alternate} \quad (42)$$

- Stress ratio ( $R$ ) is the ratio between the minimum to the maximum stress:

$$R = \frac{\sigma_{min}}{\sigma_{max}} \quad (43)$$

- The alternate stress ratio ( $\rho$ ):

$$\rho = \frac{\sigma_{mean}}{\sigma_{alternate}} \quad (44)$$

- **S-N curves**

The stress ratio ( $R$ ) is an important parameter to evaluate fatigue of composite materials. Each  $R$  ratio correspond to different behaviour of the stress cycle. Figure 2.49 shows some examples of different  $R$  ratios stress signals.

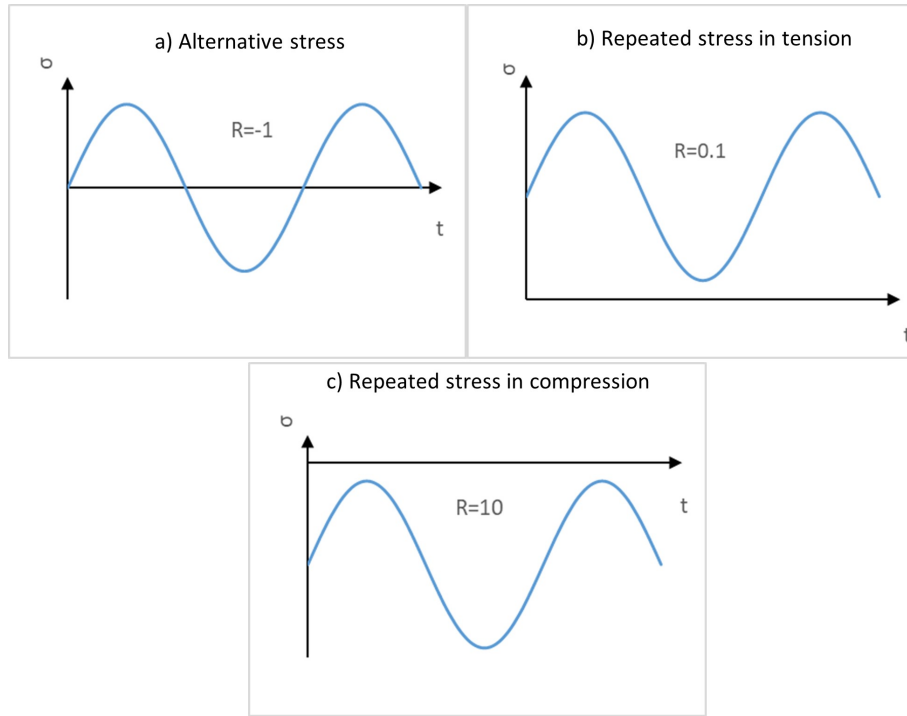


**Figure 2.49:** Different stress ratios ( $R$ ).

To construct an S-N curve of an individual layer for fibre or matrix, Eq. 45 relates the stress level for specific number of cycles to failure according to [21]. Eq. 45 gives a log-log linear curve.

$$N_{R,i} = \sigma_i^{-m} \quad (45)$$

Where:

- $N_{R,i}$  is the number of cycles to failure.
- $\sigma_i$  is the alternate stress level defined as the ratio of the alternate stress to the theoretical breaking stress:

$$\sigma_i = \frac{\sigma_{alternate}}{\sigma_{br}} \quad (46)$$

and:

$$\sigma_{br} = \frac{\sigma_{brt}}{2} \times (1 - R), \text{ when } \frac{\sigma_{brc}}{\sigma_{brt}} \leq R < 1 \quad (47)$$

or:

$$\sigma_{br} = \frac{\sigma_{brc}}{2} \times \frac{(1 - R)}{R}, \text{ otherwise} \quad (48)$$

- $m$  is the slope coefficient for the S-N curve.

#### • Linear Interpolation

Fatigue tests are time-consuming and for composite materials, one S-N curve only corresponds to one stress ratio ( $R$ ). Each stress ratio has a specific  $m$  slope coefficient

and therefore one S-N curve. Since it is tedious to perform fatigue tests for each stress ratio, another approach is to use the Constant Fatigue Life (CFL) diagram that relates the alternate stress ( $\sigma_{alternate}$ ) to mean stress ( $\sigma_{mean}$ ) of each stress ratio and number of admissible cycles ( $N$ ). Figure 2.50 shows a typical CFL diagram used for wind turbine applications [21].

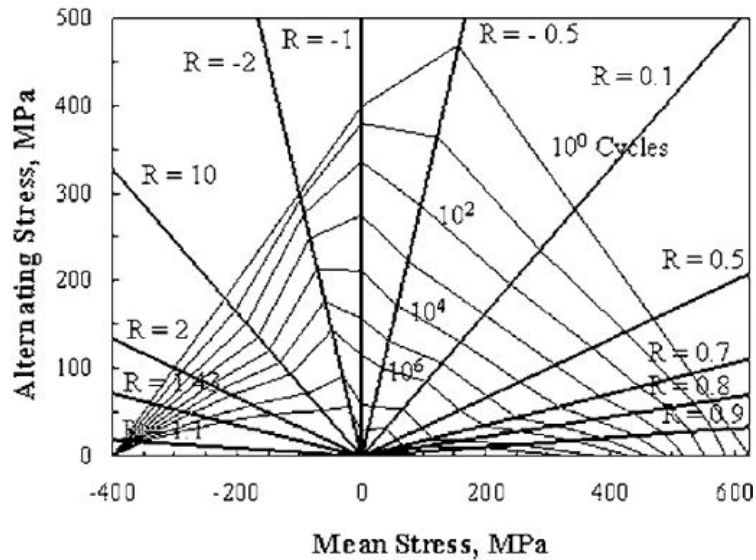


**Figure 2.50:** CFL diagram for wind turbine applications.

Knowing two stress ratios ( $R_1$  and  $R_3$ ) we can linearly interpolate an intermediate stress ratio ( $R$ ) as shown in Figure 2.51 [21].

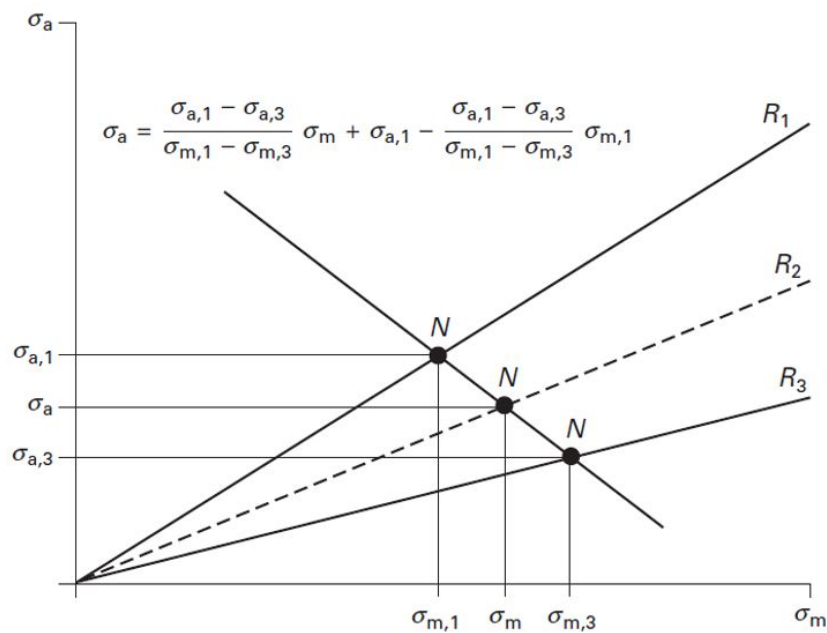


**Figure 2.51:** Intermediate ratio linear interpolation.

The intermediate alternate stress ( $\sigma_a$ ) equation in Figure 2.51 can be re-written as:

$$\sigma_a = \frac{\sigma_{a_1}(\rho_1 - \rho_3)}{(\rho_1 - \rho) \frac{\sigma_{a_1}}{\sigma_{a_3}} + (\rho - \rho_3)} \quad (49)$$

where:

- $\sigma_{a_1}$  and  $\sigma_{a_3}$  are the alternate stresses for the known ratios ( $R_1$  and  $R_3$ ) and obtained using the following equations:

$$\sigma_{a_1} = \sigma_{br1} \times \sigma_i = \sigma_{br1} \times N^{\frac{-1}{m_1}} \quad (50)$$

and,

$$\sigma_{a_3} = \sigma_{br3} \times \sigma_i = \sigma_{br3} \times N^{\frac{-1}{m_3}} \quad (51)$$

- $\sigma_{br1}$  and  $\sigma_{br3}$  are evaluated based on Eq. 47 or Eq. 48 depending on  $R_1$  and  $R_3$ .
- $\rho$ ,  $\rho_1$  and  $\rho_3$  are obtained according to Eq. 44 depending on  $R$ ,  $R_1$  or  $R_3$ .

However, in many cases, stress ratios are not always available. Most often, the results for one tensile stress ratio and one compressive ratio would be available. Since we need both ( $R_1$  and  $R_3$ ) for interpolation,  $R_3$  can be a line on the ( $\sigma_m$ ) axis. In this case,  $R_3 = 1$ ,  $\rho_3 = \infty$ ,  $\sigma_{a_3} = 0$  and  $\sigma_{m_3} = \sigma_{UTS}$  or  $\sigma_{UCS}$ . Therefore, Eq. 49 can be re-written as:

$$\sigma_a = \frac{\sigma_{UTS}}{\frac{\sigma_{UTS}}{\sigma_{a_1}} + \rho - \rho_1} \quad (52)$$

Similarly, for fatigue under compression:

$$\sigma_a = \frac{\sigma_{UCS}}{\frac{\sigma_{UCS}}{\sigma_{a_1}} + \rho - \rho_1} \quad (53)$$

Where  $\sigma_{UTS}$  is the ultimate tensile strength ( $\sigma_{brt}$ ) of the fibre or matrix and similarly  $\sigma_{UCS}$  is the ultimate compression strength ( $\sigma_{brc}$ ).

#### • Damage Calculation

Iterating over Eq. 49, we can obtain the intermediate alternate stresses ( $\sigma_a$ ) at every interpolated number of cycle ( $N$ ). This will allow constructing the S-N curve for the interpolated  $R$  ratio.

Using the stress range ( $\Delta\sigma$ ) for one Rainflow cycle, we can extrapolate the number of cycles to failure obtained by this stress range from the interpolated S-N curve. Therefore, using the Rainflow cycle ( $n$ ), the total damage ( $D$ ) experienced by the ply's fibre or matrix can be obtained using Miner's sum, expressed as:

$$D_f = \sum_i \frac{n_{f,i}}{N_{f,i}} \quad (54)$$

$$D_m = \sum_i \frac{n_{m,i}}{N_{m,i}} \quad (55)$$

Where  $n_{f,i}$  is the cycle for one stress ratio  $R$  and  $N_{f,i}$  is the admissible number of cycles under the stress range ( $\Delta\sigma$ ) for the fibres. Similarly,  $n_{m,i}$  and  $N_{m,i}$  are for the matrix. Finally, the following criteria needs to be satisfied for the fibre and matrix safety factors ( $SF$ ):

$$\max(D_m SF_m, D_f SF_f) \leq 1 \quad (56)$$

### 2.7.2. Fatigue tool validation

This section aims to demonstrate the validity of the proposed fatigue analysis tool explained in Section 2.7.1. To do so, the fatigue methodology in Section 2.7.1 is coded in Python script. The time-dependent global loads acting on the FOWT tower vector defined in Eq. 7 is generated only to showcase the validity of the python tool. The aim is to generate a time-series signal that result in alternative stress history (tension and compression).

Using the analytical formulation developed in Section 2.5.2 to convert the global loads to line loads at a given tower height and section, the global laminate deformations are obtained using Eq. 30 and hence the ply stresses defined in Eq. 33. Here, the used laminate is carbon/epoxy as defined in Table 2.11. To use the fatigue methodology proposed in this section, the ply equivalent fibre and matrix stresses are obtained using the ply local stresses as defined in Eq. 37 and 38. Figure 2.52 shows the fibre and matrix stress history experienced by the ply.

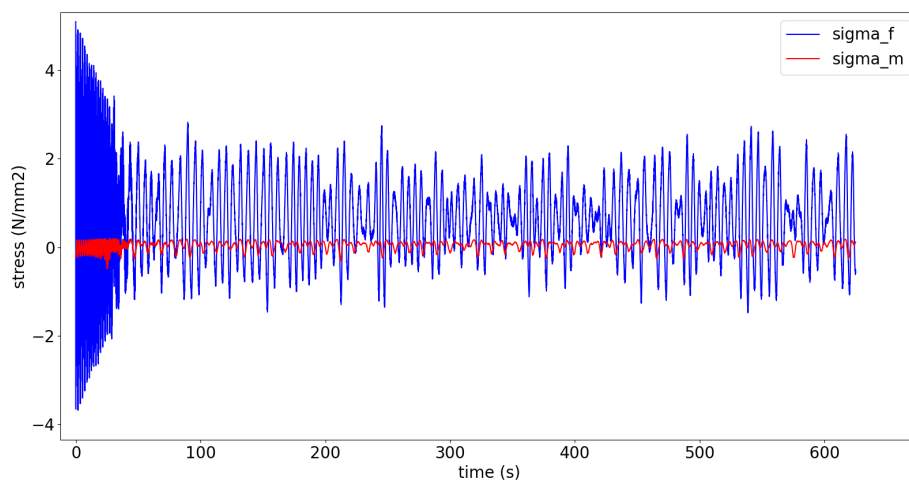


**Figure 2.52:** Ply fibre and matrix stresses.

Referring to stress history for the fibre and matrix in Figure 2.52, it can be seen that the ply is experiencing variable loading. Some cycles are in tension or compression and some has the combination of both. Figure 2.53 shows those different regions on the CFL diagram. It is essential to know which region the intermediate stress ratio ( $R$ ) is falling in to assign the boundary stress ratios ( $R_1$  and  $R_3$ ) for interpolation.

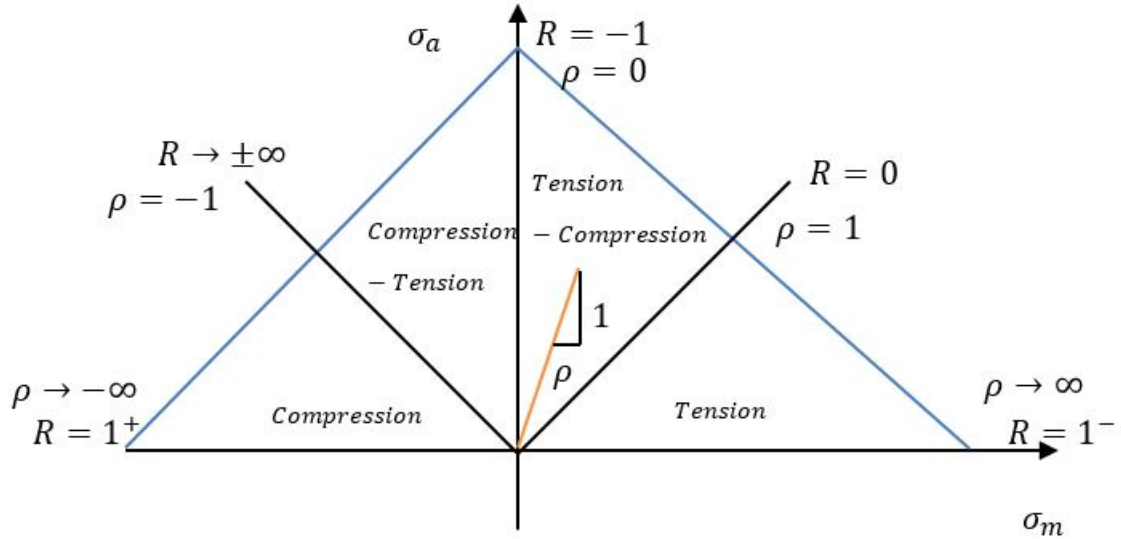


**Figure 2.53:** CFL tension-compression regions

Using the Rainflow algorithm defined in section 2.7.1, the matrix and fibre stress history in Figure 2.52 is converted to signals with different stress ratios ( $R$ ) with constant amplitudes. To use the linear interpolation approach as defined in Eq.49, the work of [23] is used for the boundary stress ratios ( $R_1$  and  $R_3$ ) with corresponding slope coefficients ( $m_1$  and  $m_3$ ) for carbon epoxy. Table 2.14 shows the used R ratios for interpolation based on the work of Kawai [23]. In this methodology, the boundary stress ratios ( $R_1$  and  $R_3$ ) are used according to Figure 2.53 but with the values based on Table 2.14.

**Table 2.14:** Slope coefficients ( $m$ ) used for interpolation.

Fibre orientation	Axis Direction	R	m
UD	parallel to fibres ( $\sigma_f$ )	-1	22.9
		0.1	20.2
		10	50.3
	perpendicular to fibres ( $\sigma_m$ )	-1	10.9
		0.1	15.0
		10	165

Figure 2.55 and Figure 2.54 show the CFL diagram of one ply using the data for the demonstrated case study. It can be seen that the stress ratios are interpolated according



to the boundary regions ( $R_1$  and  $R_3$ ) they fall at. Moreover, when ( $R_3 = 1$ ) the point on the mean stress axis correspond to the ultimate tension ( $\sigma_{UTS}$ ) or compression strength ( $\sigma_{UCS}$ ) of the fibre or matrix. Here the values of ( $\sigma_{UTS}$ ) and ( $\sigma_{UCS}$ ) are equal to the fibre and matrix theoretical breaking stresses defined in Table 2.10 for carbon and epoxy.

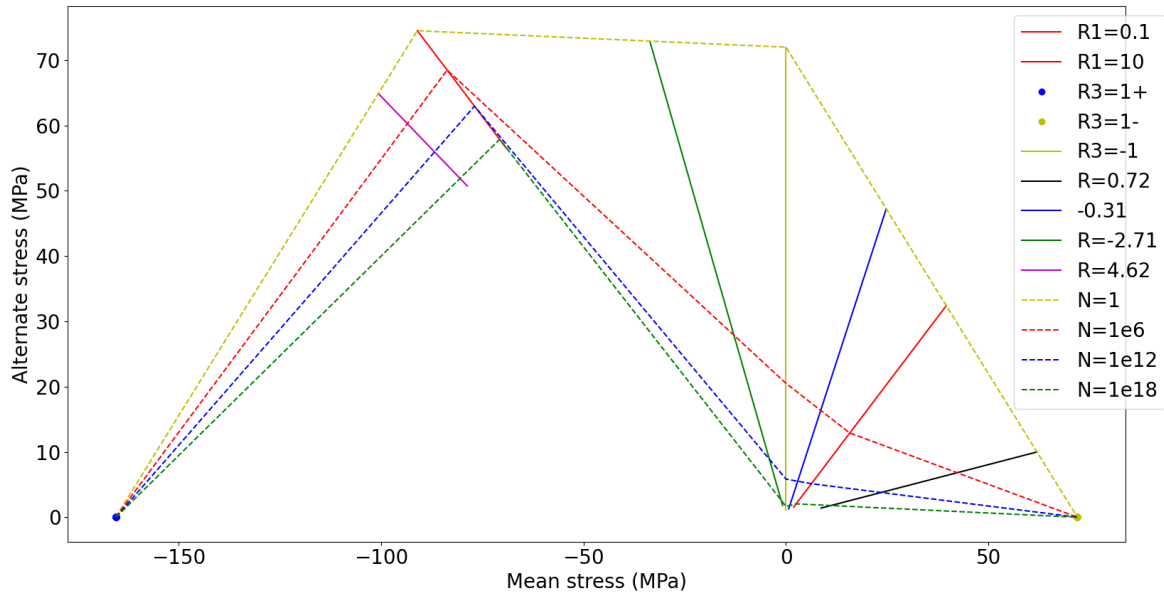


Figure 2.54: CFL matrix.

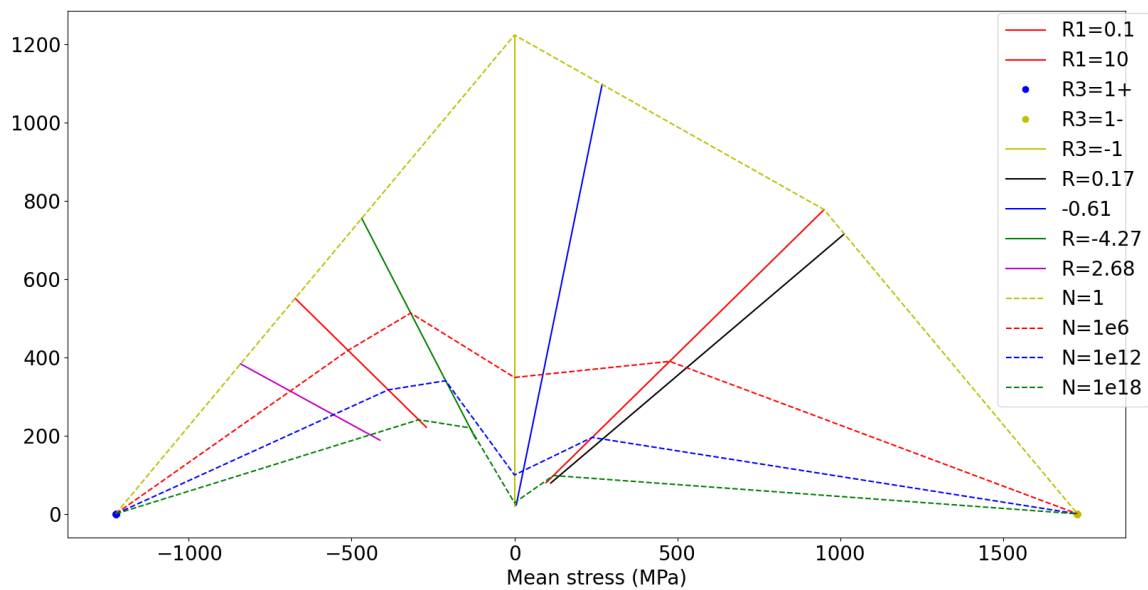


Figure 2.55: CFL fibre.

### 3. RESULTS AND DISCUSSION

In this section, the results of the analysis explained in Section 2 will be presented and discussed.

#### 3.1. Hydrodynamic Response

All the results presented in this section are for a  $0^\circ$  wave heading to simplify the analysis.

##### 3.1.1. Radiation

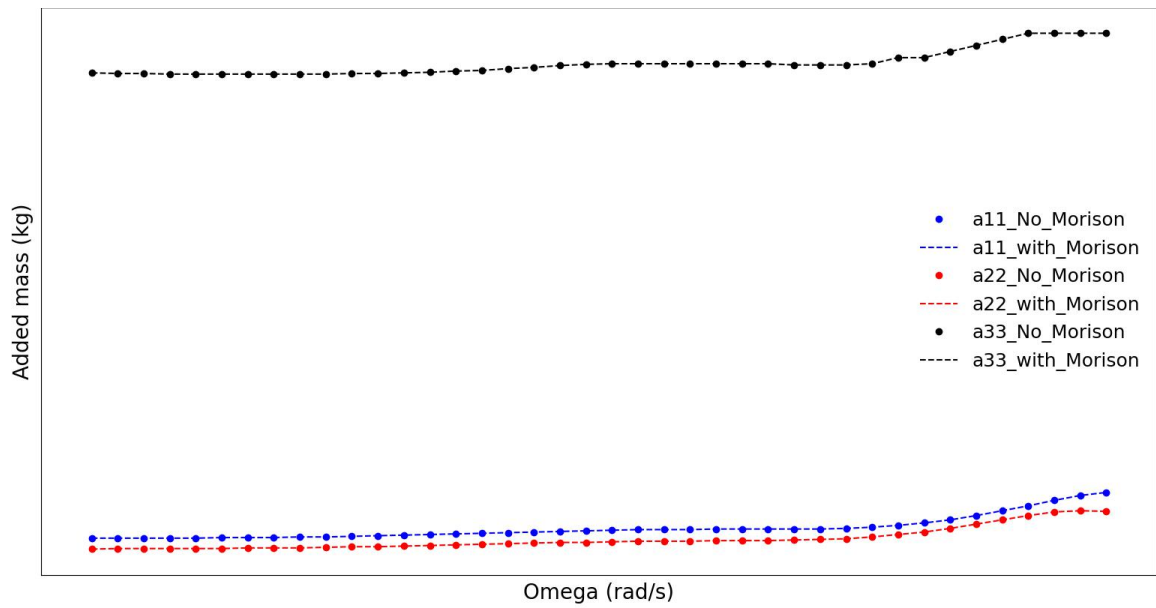
As mentioned in Section 2.3, the hydrodynamic analysis was carried out using BV software HydroStar [14]. The radiation solutions in the radiation and diffraction module solves the potential flow around the floater when the platform moves due to the incident waves. The radiation damping is defined by the ratio of the load to the floater velocity while the added mass is due to the load on the floater due to its unit acceleration [14]. The added mass matrix has the shape of 6x6 with respect to the DoF in Figure 2.5 expressed as:

$$\text{Added mass} = \begin{bmatrix} a_{11} & a_{12} & a_{13} & a_{14} & a_{15} & a_{16} \\ a_{21} & a_{22} & a_{23} & a_{24} & a_{25} & a_{26} \\ a_{31} & a_{32} & a_{33} & a_{34} & a_{35} & a_{36} \\ a_{41} & a_{42} & a_{43} & a_{44} & a_{45} & a_{46} \\ a_{51} & a_{52} & a_{53} & a_{54} & a_{55} & a_{56} \\ a_{61} & a_{62} & a_{63} & a_{64} & a_{65} & a_{66} \end{bmatrix} \quad (57)$$

Where:

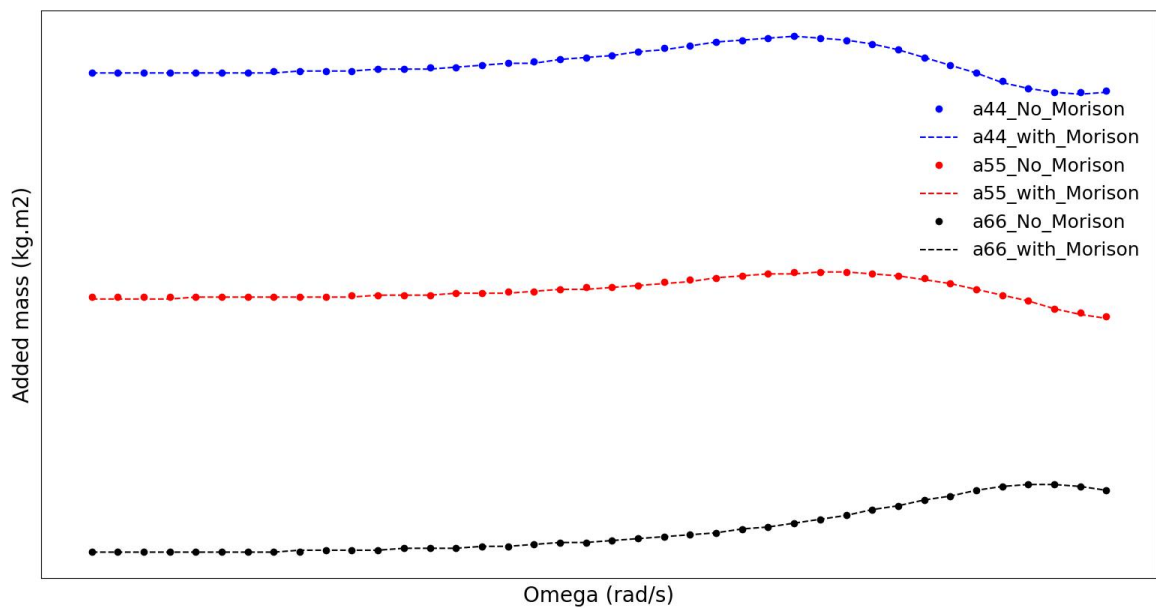
- $a_{11}$  is the surge added mass
- $a_{22}$  is the sway added mass
- $a_{33}$  is the heave added mass
- $a_{44}$  is the roll added mass
- $a_{55}$  is the pitch added mass
- $a_{66}$  is the yaw added mass

Figure 3.1 and 3.2 show the added mass plot with respect to different frequencies. Using Morison elements have no influence on the added mass since they are added in the mcn. module when computing the motions. The added mass in heave is higher compared to surge and sway due and similarly, roll and pitch are higher than yaw DoF due to the presence of heave plates.



**Figure 3.1:** Added mass in translation DoF.

In the work of [12], the added mass in pitch was higher than roll, this is due to the presence of the braces as shown in Figure 2.7 while in this work, the braces were not modeled but instead were added as Morison elements.



**Figure 3.2:** Added mass in rotational DoF.

To dissipate the energy exerted by the waves due to the interaction between the wave and floater, the radiation damping is used. Figure 3.1 and 3.4 and show the radiation damping output from HydroStar. Due to the presence of the heave plates, the radiation damping is higher in heave DoF compared to surge and sway. Similarly, the three heave plates

produce more damping in the roll and pitch compared to yaw. The radiation damping in all DoF increases with the increase of the wave frequencies.

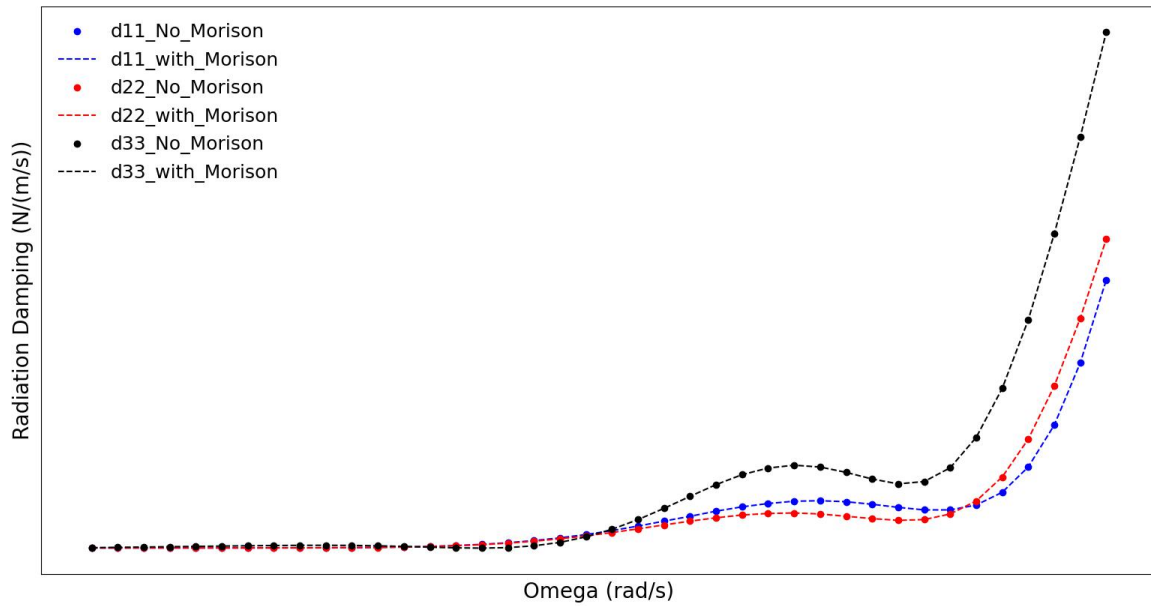


**Figure 3.3:** Radiation damping in translation DoF.

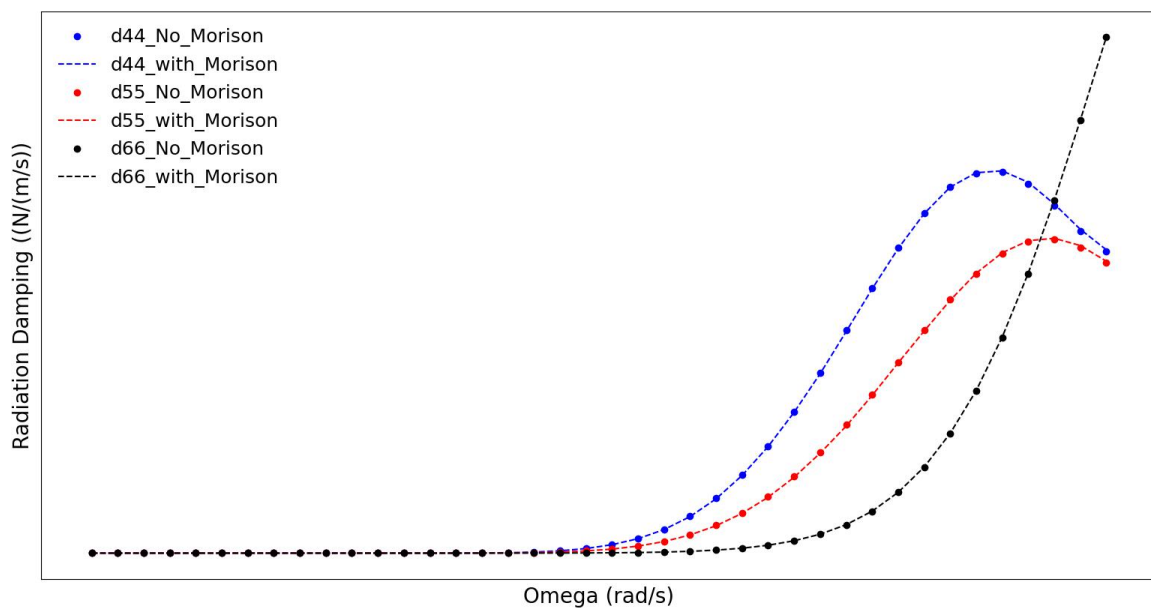


**Figure 3.4:** Radiation damping in rotational DoF.

### 3.1.2. Diffraction

The potential flow solution of incident waves around the still floater is called diffraction. By integrating the dynamic pressure acting on the floater, the wave excitation loads are obtained due to the incoming waves [14]. The diffraction force which is obtained by

integration of pressures from Airy theory for regular waves assuming deep water condition [24]. The diffraction force is expressed as:

$$F = \int_A PdA \quad (58)$$

Figure 3.5 and 3.6 show the first-order wave loads output from HydroStar. The force in the surge direction increases with the increases of the wave frequency. The force in the sway DoF is zero due to symmetry. Similarly, the moments in Sway and roll are very low compared to the pitch moment where it increases with more frequencies.

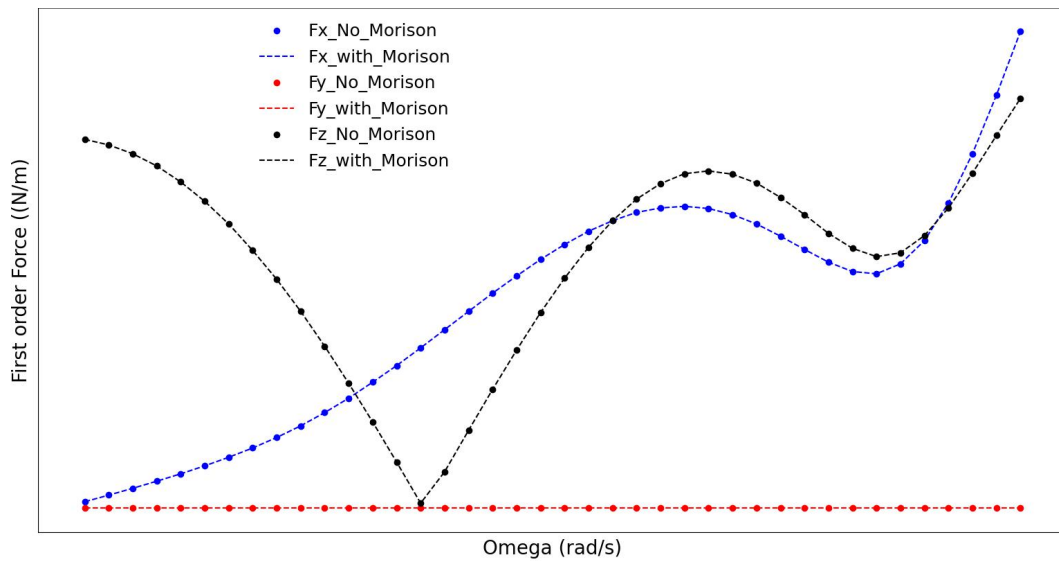


**Figure 3.5:** First-order forces in translation DoF.

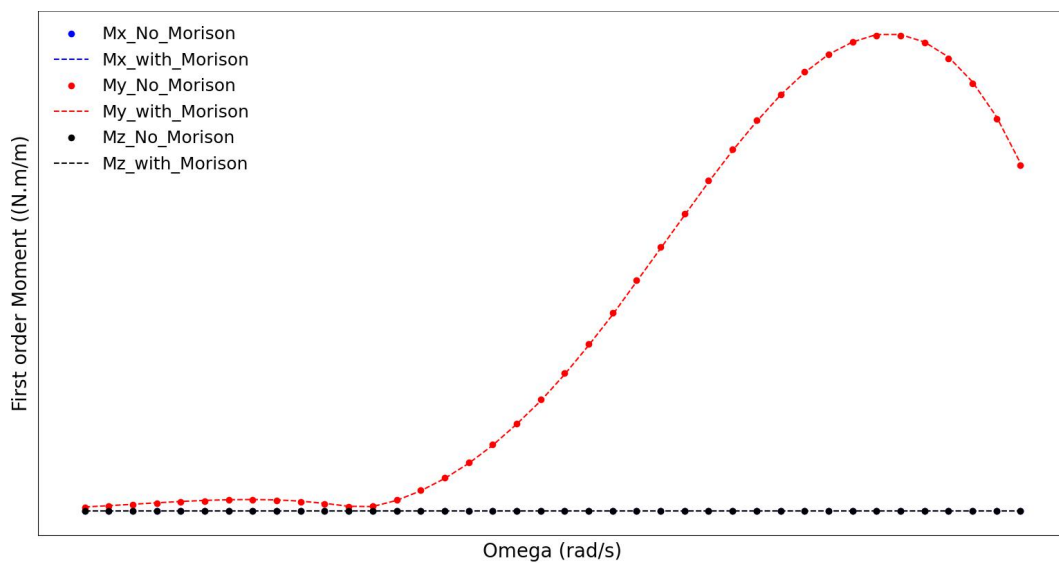


**Figure 3.6:** First-order moments in translation DoF.

### 3.1.3. Motions

To describe the motions of the floater, Newton's second law is used [14] and it is expressed as:

$$([M] + [M_A])\ddot{X} + [B]\dot{X} + [K]X = F \quad (59)$$

Where:

- $[F]$  is the diffraction and Froude-Krylov excitation incident-wave load comes from the rdf. module.
- $[X]$  is the floater motion vector
- $[K]$  is the stiffness matrix using the floater hydro-static properties computed in rdf. module.
- $[B]$  is the damping matrix comes from the radiation damping in rdf. module.
- $[M_A]$  is the added mass matrix computed from the rdf. module.
- $M$  is the inertia matrix of the FOWT. This is computed from the mcn. module by taking the total mass and CoG of the whole FOWT (not the floater only).

The motion of the FOWT is computed as Response Amplitude Operators (RAOs) for each motion. The RAO is calculated using the following equation:

$$RAO = \left| \frac{\eta_0}{a} \right| = \frac{|F/a|}{\sqrt{([K] - \omega_i^2([M] + [M_A]))^2 + \omega_i^2[B]^2}} \quad (60)$$

Where  $\eta_0$  is the response and  $a$  is the wave amplitude and  $\omega$  is the wave frequency. Figure 3.7 and 3.8 show the FOWT motion response (RAOs) in translation and rotation. The surge motion is decreasing from low to high frequencies due to the absence of the mooring lines.

The heave motion without Morison elements showed high response around the natural frequency while with Morison elements the heave response was damped. The RAO in pitch exhibited the opposite response with and without Morison elements compared to heave with more response when using Morison elements around the natural frequency. There are no motions response in sway, roll and yaw under the  $0^\circ$  wave heading.

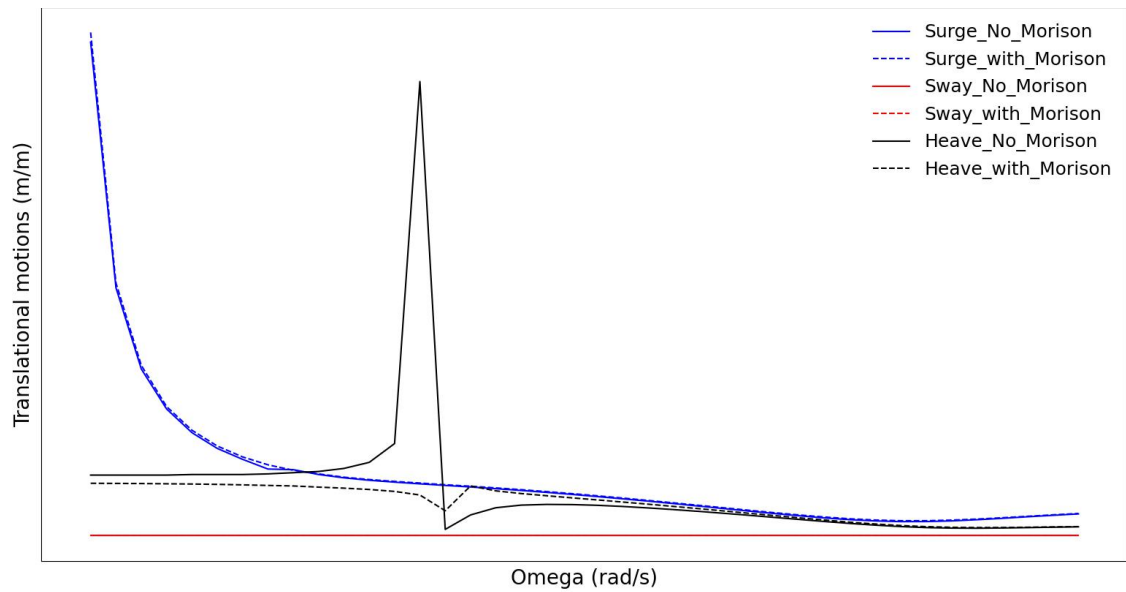


**Figure 3.7:** Translational motions (RAOs)

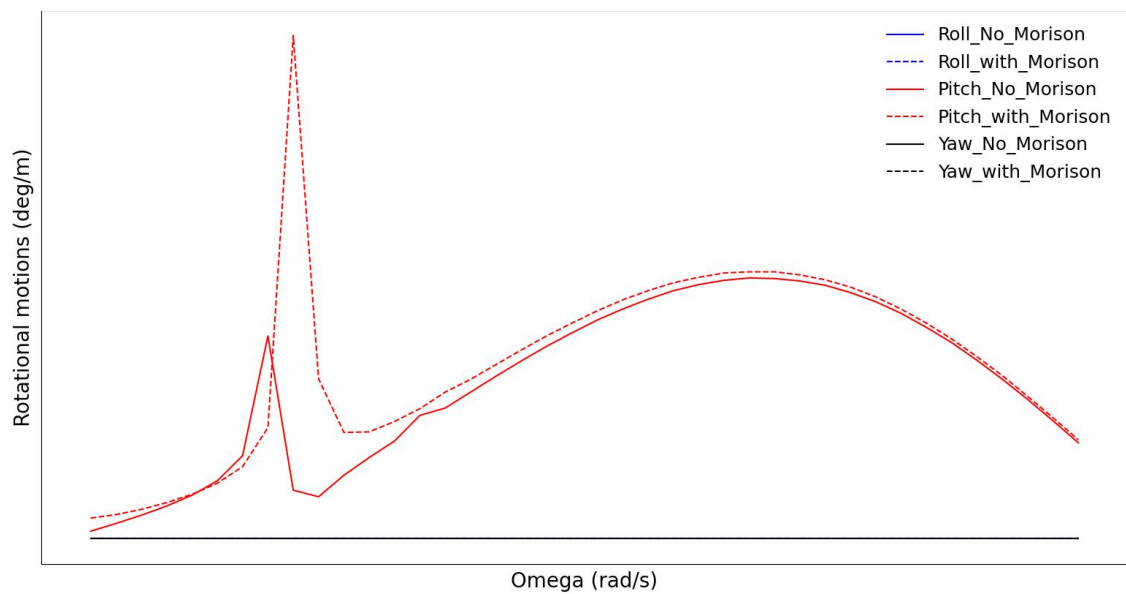


**Figure 3.8:** Rotational motions (RAOs)

### 3.1.4. 2nd order loads

The quadratic function of the incident and diffraction wave fields governs the low-frequency loads. The solution of the second order problem result in the formation of the QTF except the diagonal terms that correspond to the mean drift loads which is found from the 1st order solution [14]. The output of the qtf. module is loaded to OPERA. From the results in OPERA, the QTF loads were found to be minimal compared to the first-order loads.

## 3.2. FOWT Global Response

The output from HydroStar obtained in Section 3.1 is loaded in OPERA along with all the inputs defined in Section 2.4.

### 3.2.1. Model verification

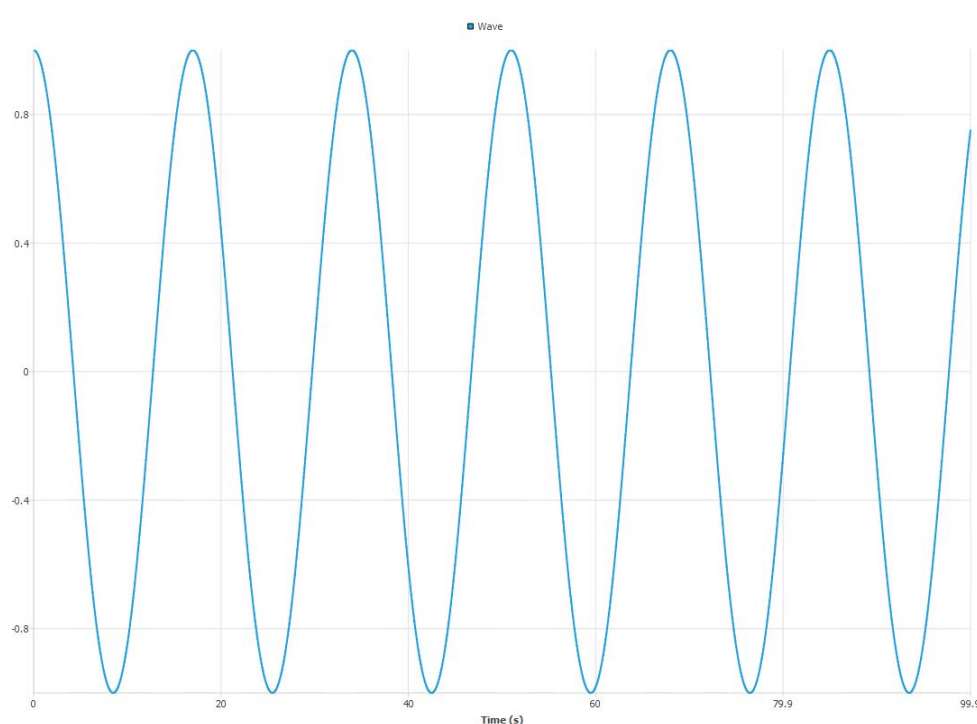
To verify the different inputs used in OPERA are correct, several checks were performed including the followings:

- **Stability**

The stability check for each components loaded in OPERA was checked by looking at the gravity and Archimedes loads of the output file. Several run were made to ensure the FRP towers, nacelles, blades and floater yielded the expected weight before going for any further analysis. The floater displacement was checked as well to ensure the Archimedes loads is sufficient to maintain the design draft of the platform.

- **Motions (RAO)**

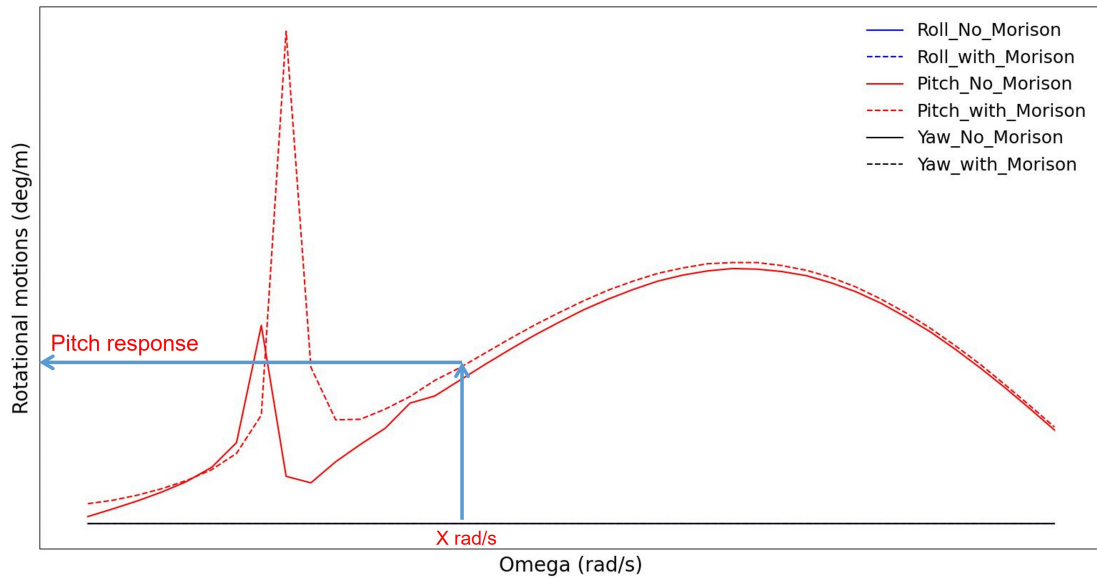
The motions (RAOs) of the FOWTs were checked by running several regular waves with amplitude of 1 meter and against different frequencies in OPERA. The response in the motions was ensured to be the same as the one computed in HydroStar [14] and as shown in Section 3.1. Figure 3.9 shows an example of a regular wave signal with  $x$  frequency.



**Figure 3.9:** Regular wave signal in OPERA.



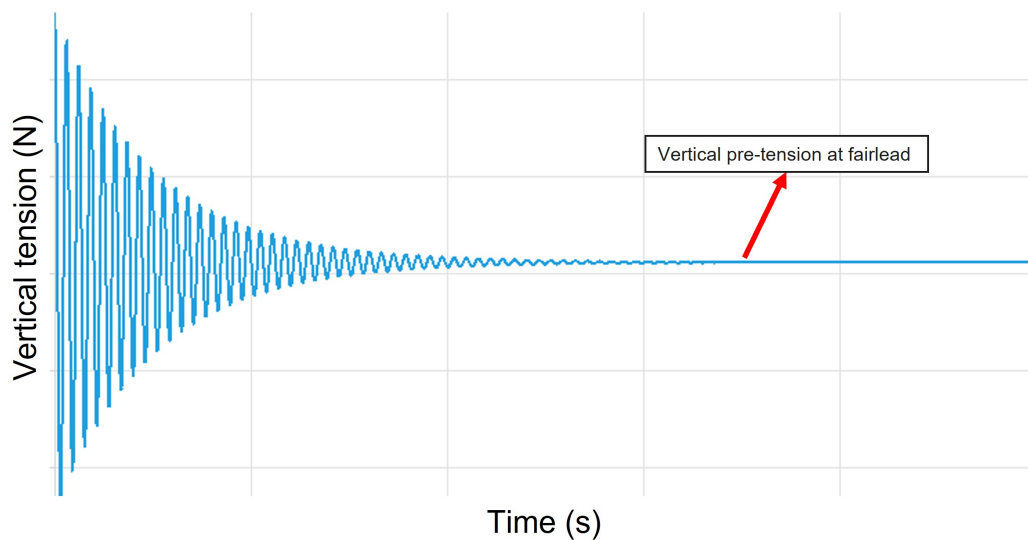
Figure 3.10 shows an example of the checking method in pitch motion with HydroStar RAO. The process was repeated with different frequencies for different motions and first-order loads.



**Figure 3.10:** Pitch response verification against regular waves.

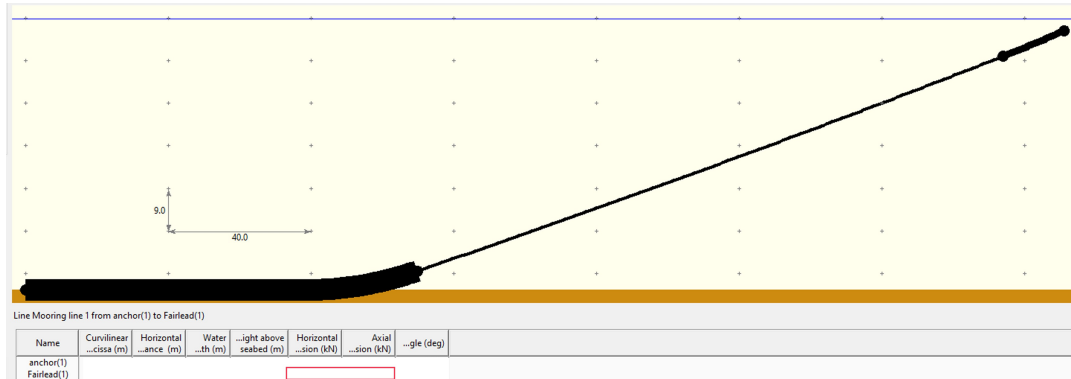
- **Mooring lines**

The mooring line pre-tension, horizontal and vertical stiffnesses at the fairlead were checked to ensure agreement with the data provided by FibreGY partners [10]. The pre-tension in OPERA was also verified with BV software Ariane [25] to ensure the values were correct. Figure 3.11 shows the output in OPERA in terms of vertical pre-tension at the fairlead.



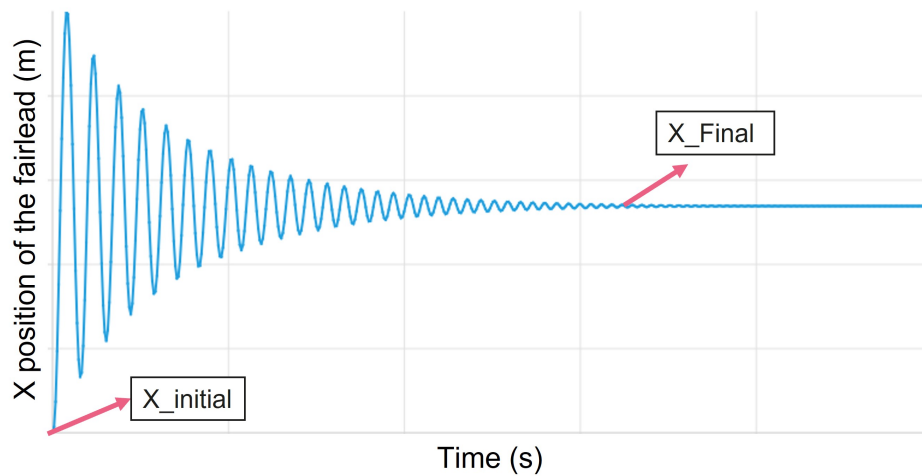
**Figure 3.11:** Vertical pre-tension at fairlead in OPERA.

Figure 3.12 shows the mooring lines set up in Ariane [25] with axial and horizontal pre-tensions at the fairlead. The vertical pretension in Ariane was obtained using both the axial and horizontal tensions in the output file.



**Figure 3.12:** Axial and horizontal pre-tensions at fairlead in Ariane.

The horizontal and vertical stiffnesses of the mooring lines were checked by applying horizontal and vertical forces at the fairlead in both negative and positive directions of the (X, Y and Z) axis. The offset in the axis direction was obtained from the output file in OPERA. Figure 3.13 shows an example of the fairlead offset in the X-direction.



**Figure 3.13:** Fairlead offset in the x-direction

Eq. 61 was then used to obtain the stiffness at the desired direction. Figure 3.14 shows a summarized schematic of the mooring lines stiffnesses at the fairlead. For Y-axis only one direction was considered due to symmetry of the FOWT platform.

$$F = K \Delta x$$

$$K = \frac{F}{\Delta x} = \frac{F}{X_{final} - X_{initial}} \quad (61)$$

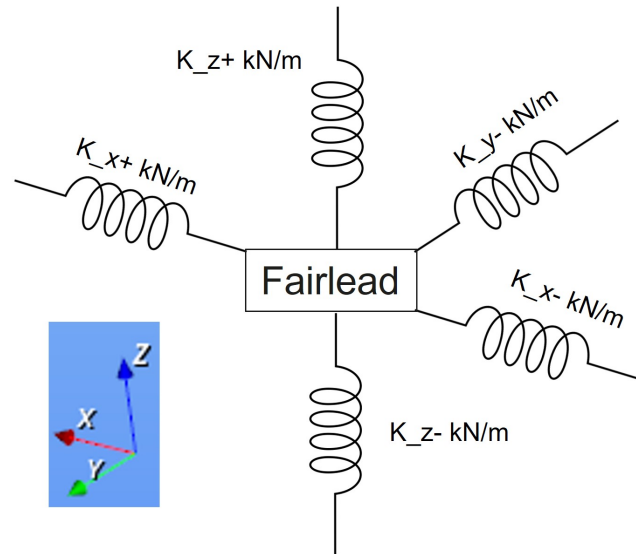


**Figure 3.14:** Schematic of the horizontal and vertical stiffnesses at the fairlead.

### 3.2.2. Global internal loads

The global internal loads of each section of the tower was obtained after running all the load types defined in Section 2.4.7, Table 2.4. Figure 3.15 and 3.16 show the internal global forces and moments at tower base section N-Full according to the tower segments in Figure 2.4.

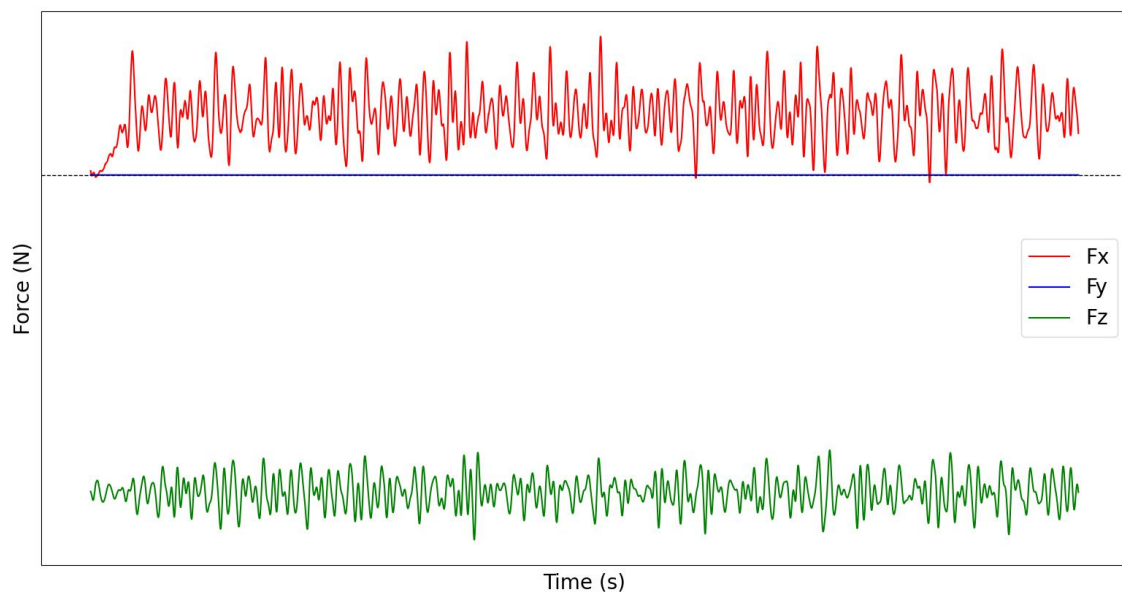


**Figure 3.15:** Global Forces time-series at tower base section.

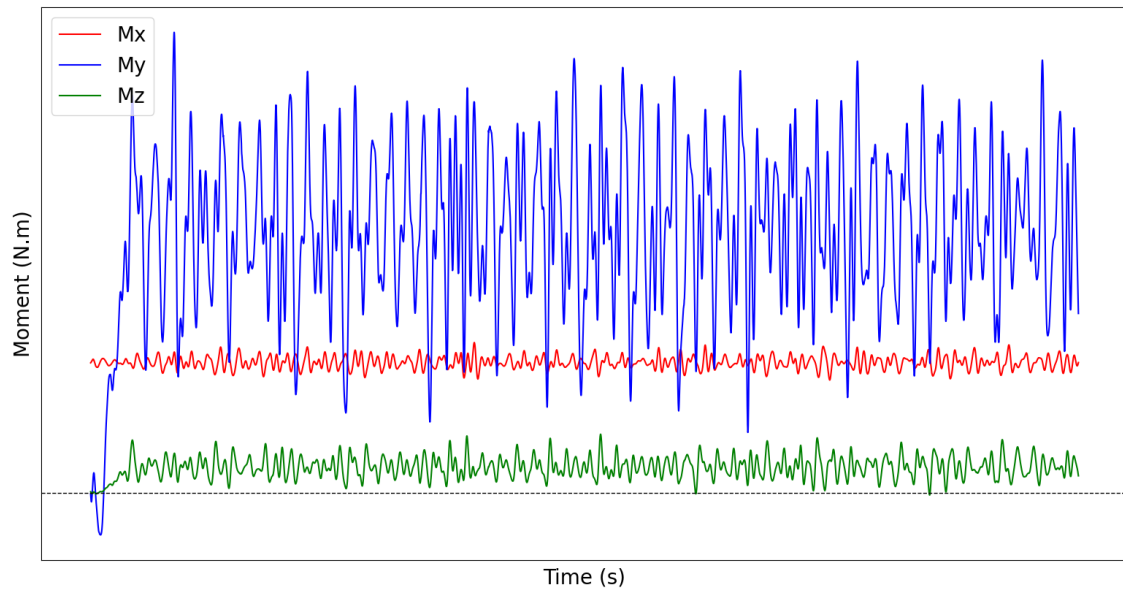


**Figure 3.16:** Global Moments time-series at tower base section.

The global internal loads are maximum at the tower base and decreases as the studied section is further from the tower base. The maximum moment is in the  $y$ -axis ( $M_y$ ) as shown in Figure 3.16. To show that the magnitude of the loads are different in various section of the tower, ( $M_y$ ) is shown in Figure 3.17.

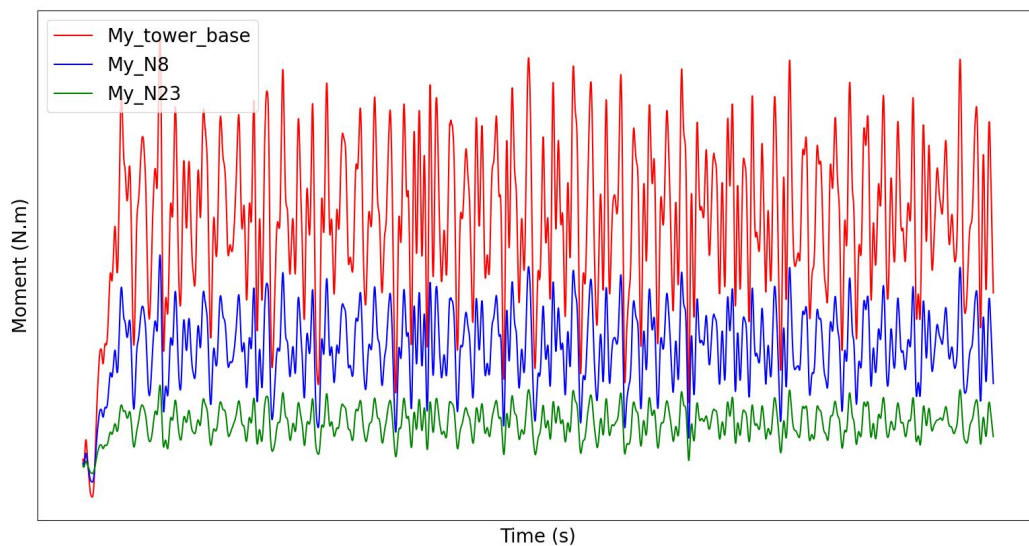


**Figure 3.17:**  $M_y$  at various sections of the tower.

The internal global loads follow the global frame reference system. The internal loads are viewed by taking the lower half of the tower as shown in Figure 3.18. Therefore, all

the forces are positive since they follow the global system except  $F_z$  is negative since the weight is acting downward as shown in Figure 3.15. All the moments are positive following the thumb rule as demonstrated in Figure 3.16.

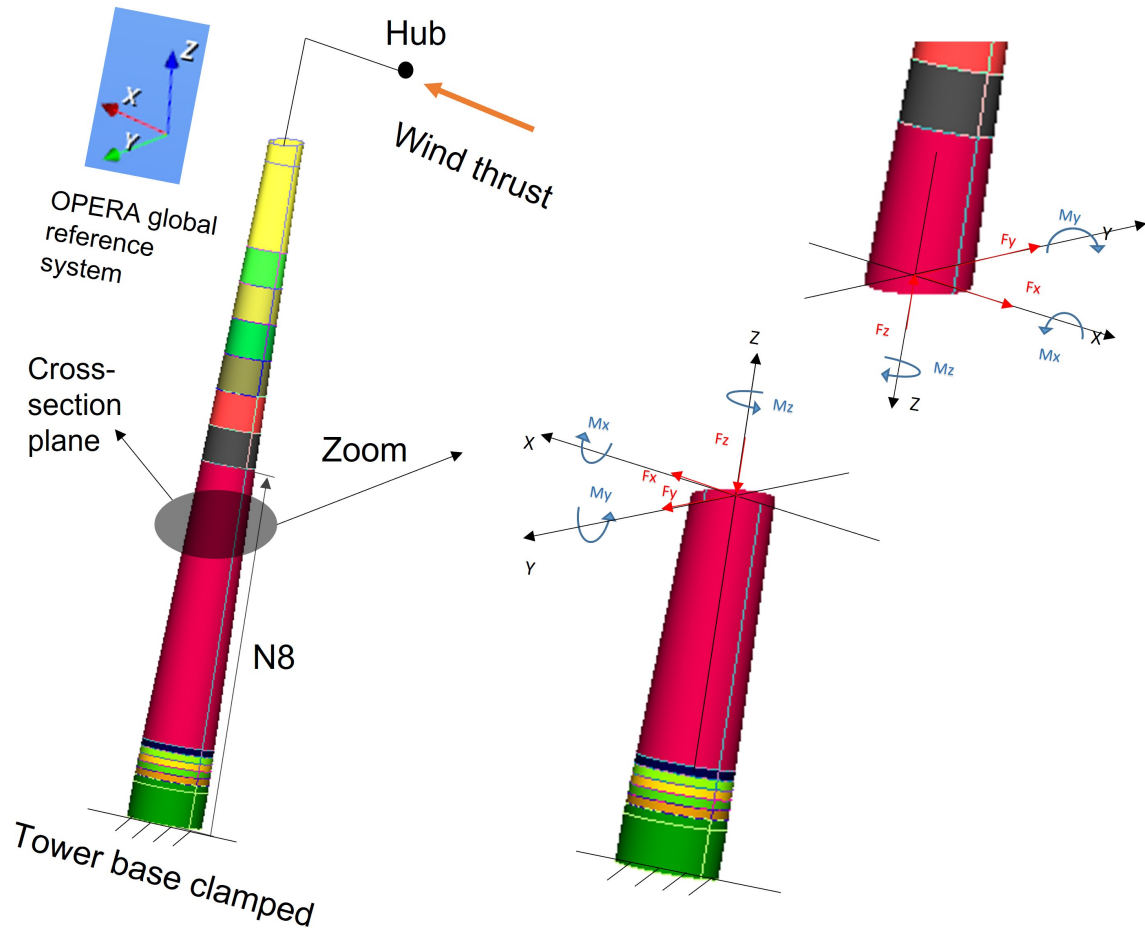


**Figure 3.18:** Global frame system and internal loads in OPERA.

### 3.3. Macro-Mechanical Analysis

#### 3.3.1. Line loads

In this section the ply stresses at different sections of the FRP tower will be assessed using the macro-mechanical Python tool developed in Section 2.6. The global internal loads from OPERA were converted to in-plane line loads acting on the mid-plane of the laminate as demonstrated in Section 2.5.2.

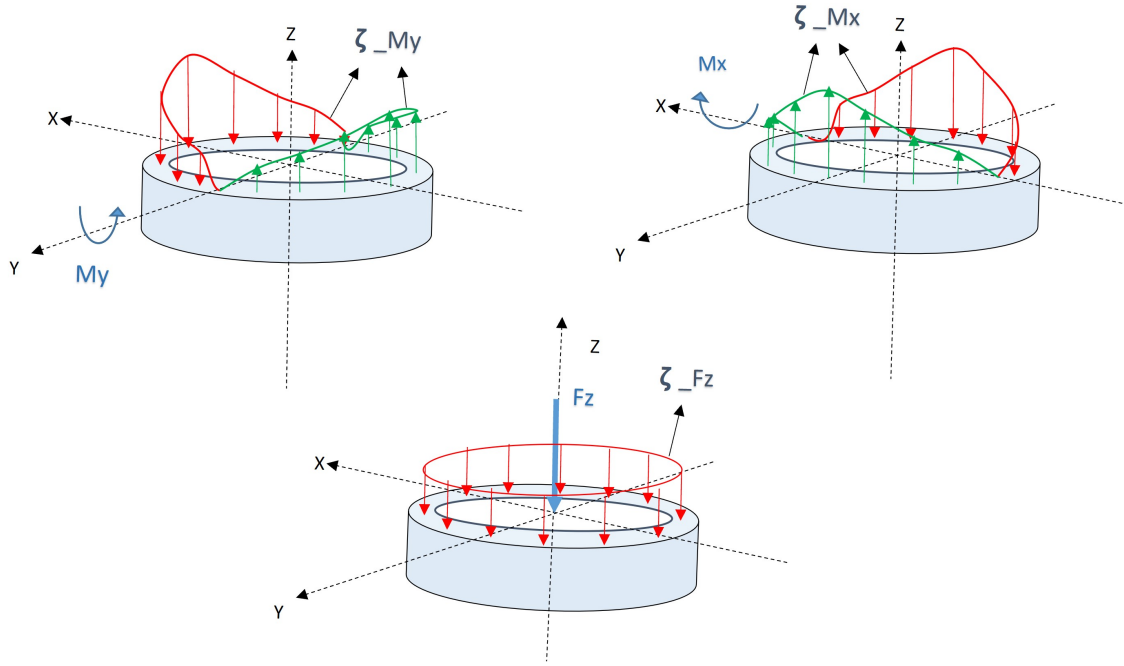


**Figure 3.19:**  $Nx$  line loads variation in different radius angles.

First, critical elements at a specific tower section are selected. The selection of the elements was based on the maximum compression and tension line loads. The elements location were based on the radius angle ( $\theta$ ). Figure 3.19 shows the line load ( $Nx$ ) profile with respect to the radius angle due to the axial global internal force  $F_z$  and bending moments  $M_x$  and  $M_y$ .

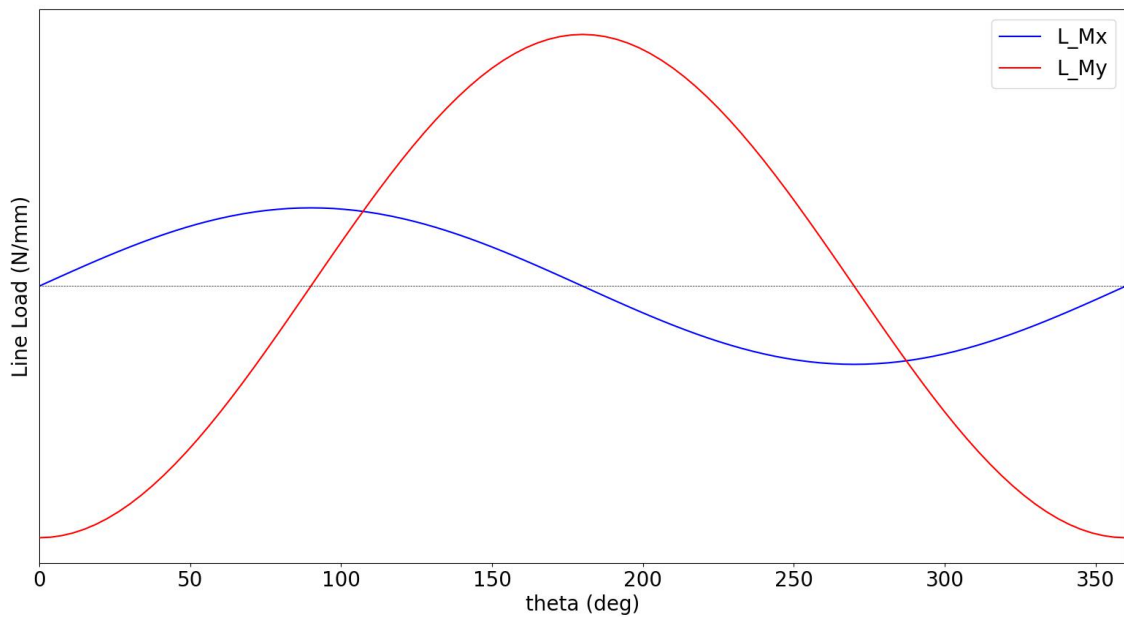


**Figure 3.20:**  $\zeta_{M_x}$  and  $\zeta_{M_y}$  line loads with respect to radius angle  $\theta$ .

The selection of the critical element is based on the radius angle. The maximum peak

global bending moment ( $M_y$ ) in Figure 3.16 was chosen. The other global forces and moments were taken corresponding to maximum  $M_y$ .

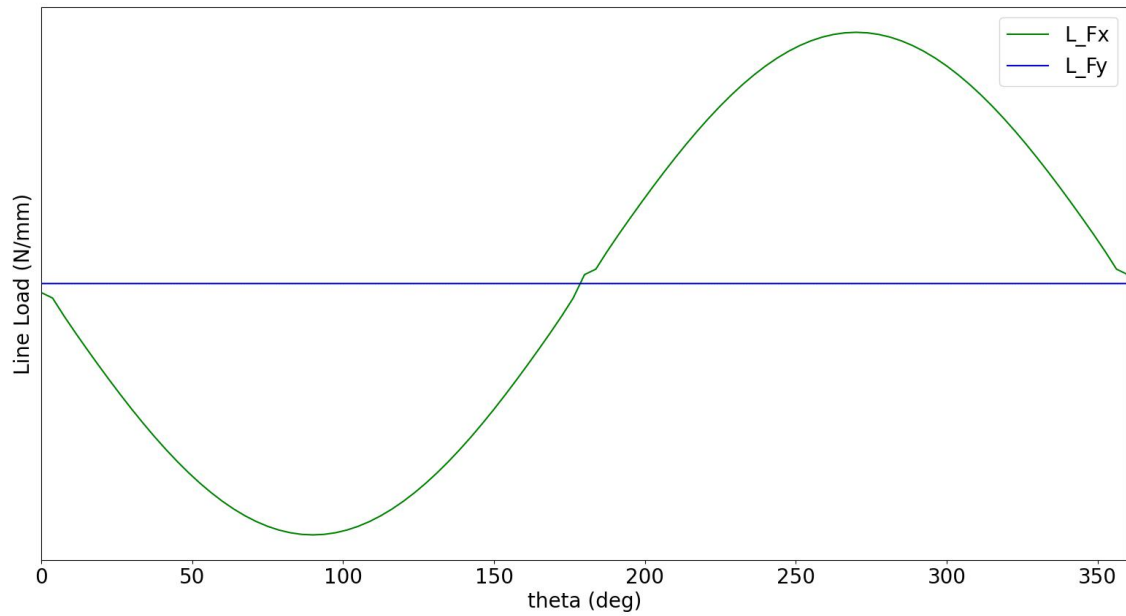


**Figure 3.21:**  $\zeta_{F_x}$  and  $\zeta_{F_y}$  line loads with respect to radius angle  $\theta$ .

The laminate axis in the tower is shown in Figure 3.22. The x axis is the normal axis where the line load  $N_x$  is acting. The y axis is the hoop axis of the tower tube for  $N_y$  line of action.

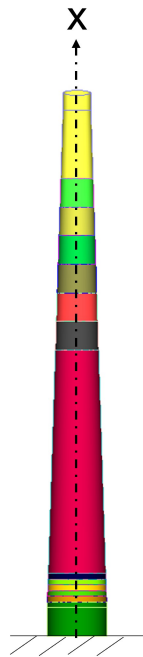


**Figure 3.22:** Laminate axis in the tower.

The section at the tower base is selected to demonstrate the results based on the internal global loads shown in Figure 3.15 and 3.16. Figure 3.20 shows the line loads  $\zeta_{M_x}$ ,  $\zeta_{M_y}$  across the radius angles. The line load  $\zeta_{F_z}$  is constant with respect to the radius angle. Similarly, Figure 3.21 shows the shear line loads  $\zeta_{F_x}$  and  $\zeta_{F_y}$  with respect to the radius angle. The torsion line load  $\zeta_{M_z}$  is constant across the tube edge.

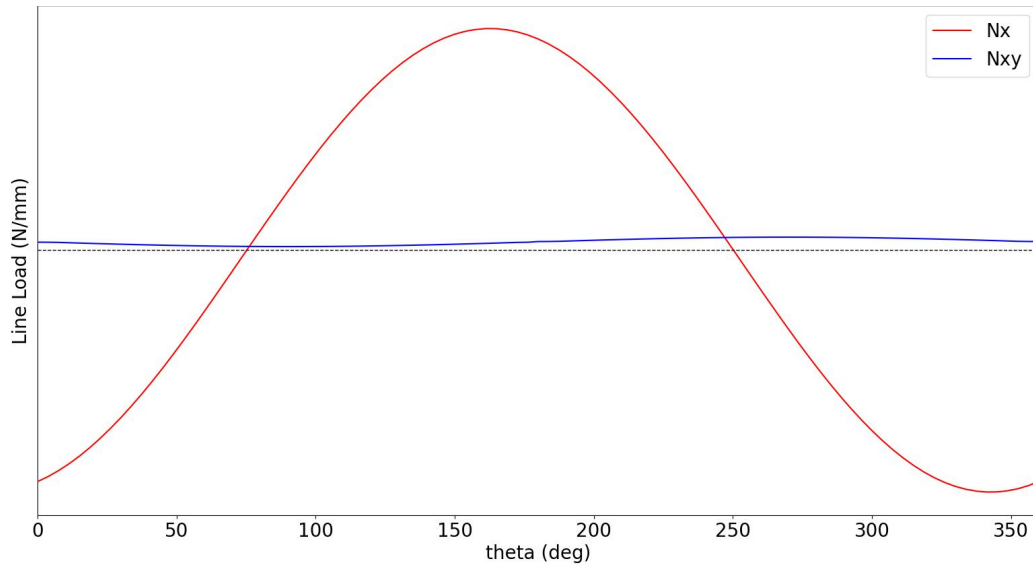


**Figure 3.23:** In-plane forces  $N_x$  and  $N_{xy}$  with respect to radius angle  $\theta$ .

Using Eq. 28 and 29, Figure 3.23 is plotted. The maximum tension value of  $N_x$  occurred in a radius angle of  $161.25^\circ$  and maximum compression value at  $341.25^\circ$ . The value of  $N_{xy}$  is small compared to  $N_x$ . These two radius angles are used to locate the elements to compute the ply stresses and assess the fatigue damage. Figure 3.24 and 3.25 shows the time-series in-plane forces in the elements correspond to  $161.25^\circ$  and  $341.25^\circ$ , respectively.

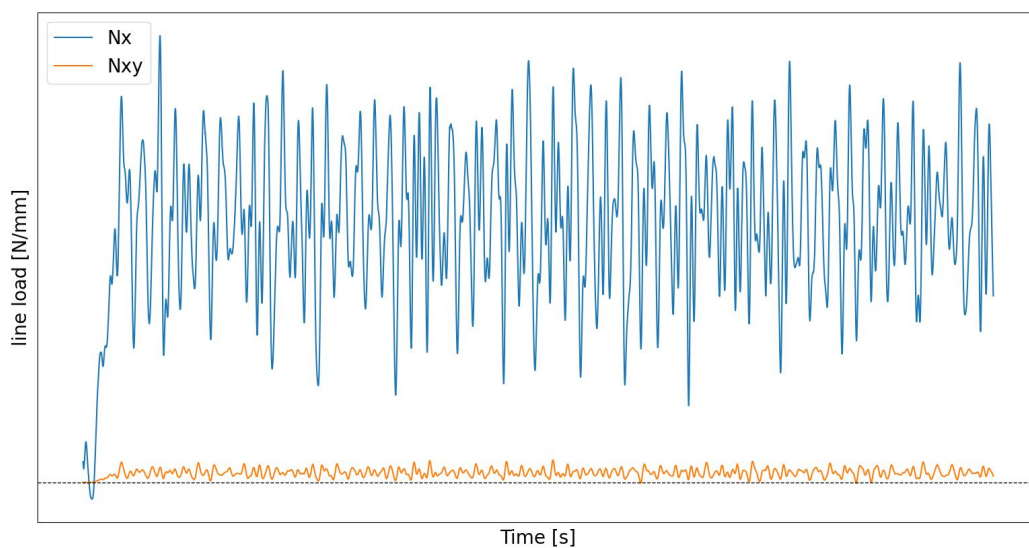


**Figure 3.24:**  $N_x$  time-series at  $161.25^\circ$ .



Referring to Figure 3.24, it is clear that the element at  $161.25^\circ$  radius angle is under tension while in Figure 3.25 it is under compression at  $341.25^\circ$ .

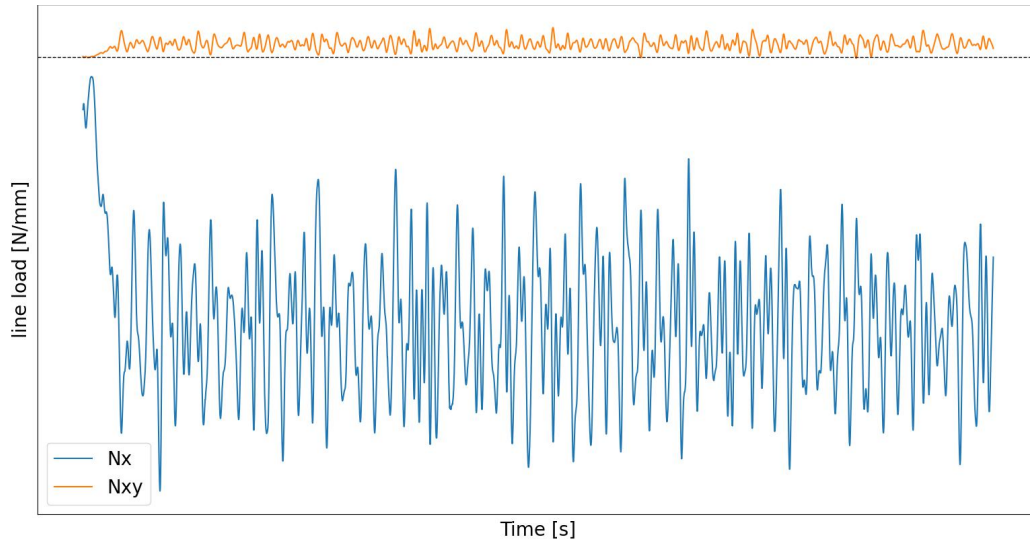


**Figure 3.25:**  $N_x$  time-series at  $341.25^\circ$ .

### 3.4. Fatigue Analysis

#### 3.4.1. Ply stresses

The time-series ply stresses are computed starting from Eq. 30 to Eq. 33. Figure 3.26 shows an example of the ply stresses in function of time ( $\sigma_1$ ,  $\sigma_2$  and  $\tau_{12}$ ) at  $90^\circ$  ply under compression line load  $N_x$ , Figure 3.25. The ply is more stressed in  $\sigma_1$  compared to  $\sigma_2$  and  $\tau_{12}$ .

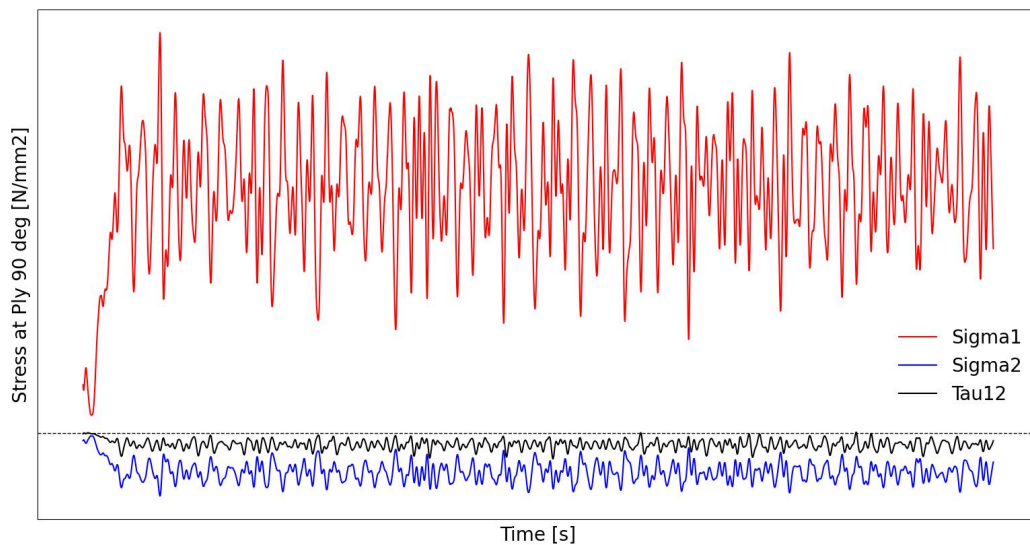


**Figure 3.26:** Ply stresses time-series at  $90^\circ$  ply.

To use the fatigue methodology explained in Section 2.7, first, the fibre and matrix time-series stresses were computed according to Eq. 37 and 38. Figure 3.27 shows the fibre and matrix stress history for the 90° ply as an example.

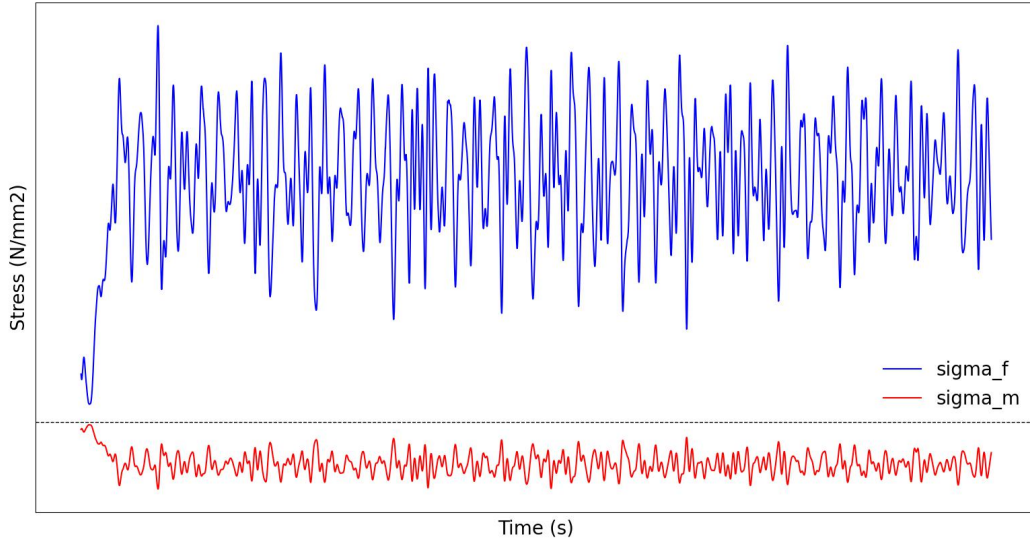


**Figure 3.27:** Fibre and matrix stress history of 90° ply.

### 3.4.2. S-N curve linear interpolation and CFL diagram

Using rainflow algorithm and linear interpolation as explained in Section 2.7. Figure 3.28 shows S-N diagram and the linear interpolation of an intermediate stress ratio ( $R$ ) between two known stress ratios  $R_1$  and  $R_3$ . Using the stress range ( $\Delta\sigma$ ) for one rainflow cycle, we can extrapolate the number of cycles to failure ( $N$ ) using stress range from the interpolated S-N curve as shown in Figure 3.28. The  $N$  value is simply obtained by using  $(10^{\log N})$ . The damage for one stress ratio is then computed using Eq. 54 and 55 for fibre and matrix, respectively.

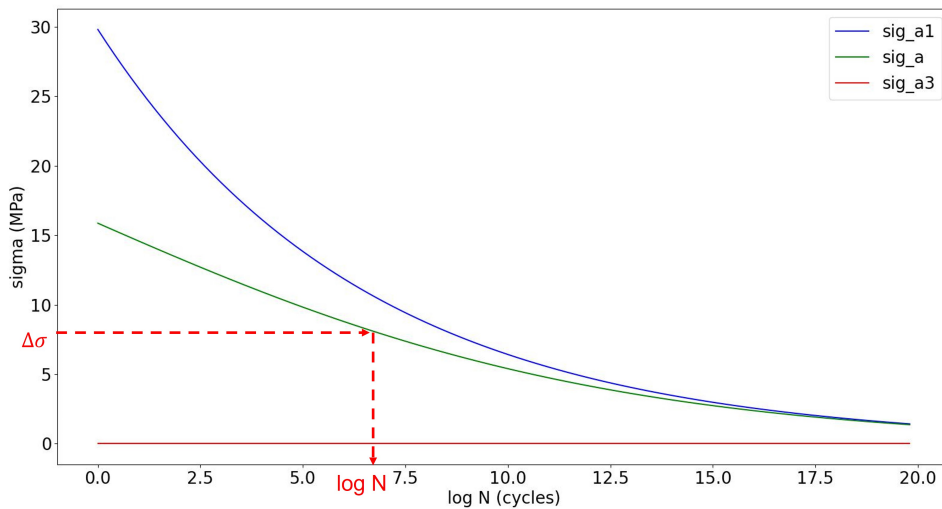


**Figure 3.28:** S-N diagram linear interpolation example for the matrix 90° ply.

Continuing with 90° ply example, the CFL diagrams for the matrix and fibre are plotted in Figure 3.29 and 3.30. The matrix is experiencing compression in the 90° ply while the fibres are under tension as shown in Figure 3.27. Referring to Figure 3.29 and 3.30 the fatigue life of the matrix in compression will drive the fatigue design while for the fibre tension is the design driver.

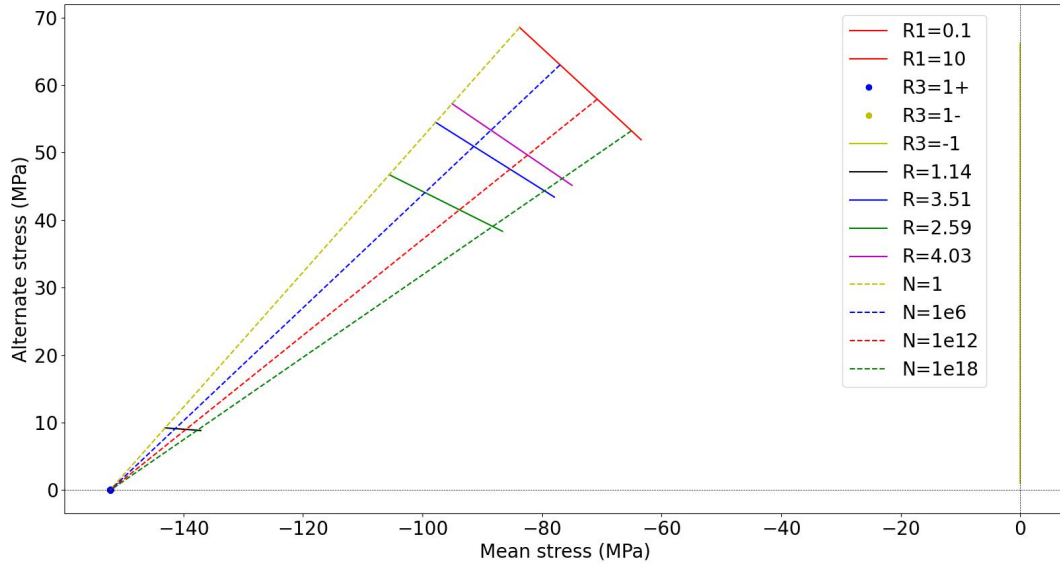


**Figure 3.29:** Matrix CFL diagram for 90° ply.

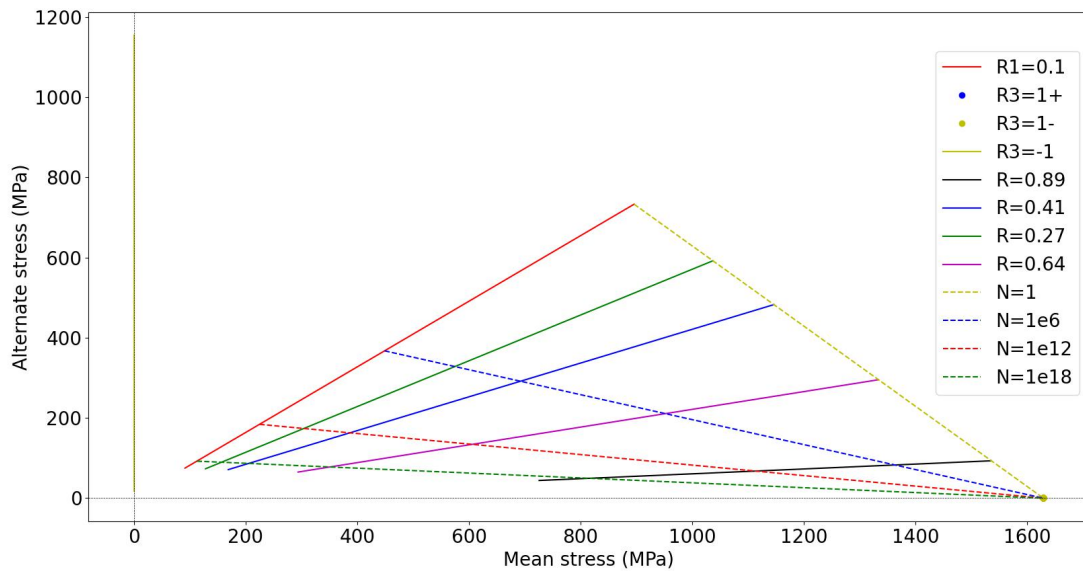


**Figure 3.30:** Fibre CFL diagram for 90° ply.

The fatigue damage was computed using Eq. 54 and 55 at the tower base. Table 3.1 shows the damage of some of the plies with different orientation at an element ( $\theta = 341.25^\circ$ ) under compression. Similarly, Table 3.2 shows the fatigue damage at an element ( $\theta =$

161.25°) under tension. The damage was computed considering 20 years design life of the FOWT tower.

**Table 3.1:** Fatigue damage of several plies at the tower base ( $\theta = 341.25^\circ$ ).

Ply Orientation	Matrix	Fibre
45	1.7E-19	1.7E-28
-45	1.5E-19	4.6E-32
0	3.7E-18	6.6E-32
90	1.1E-19	6.8E-21

Referring to Table 3.1 and 3.2, the fibre has less damage in compression compared to tension. However, the damage in the matrix is different in compression and tension depending on the ply orientation. Ply -45° ply has the highest damage in the matrix under tension while 0° ply has more damage in compression. The highest damage in the fibre is in 90° ply in compression while 0° ply has more damage in tension.

**Table 3.2:** Fatigue damage of several plies at the tower base ( $\theta = 161.25^\circ$ ).

Ply Orientation	Matrix	Fibre
45	5.6E-17	2.0E-19
-45	1.1E-16	2.9E-19
0	8.8E-19	2.6E-18
90	6.1E-17	1.5E-26

### 3.4.3. Summary

The fatigue methodology of FRP tower at the tower base was applied in this section. The fatigue damage was computed at each ply in two different elements. Namely, element with radius angle of 341.25° under compression and the other element under tension with radius angle of 161.25°. The results show that the FRP tower has very low fatigue damage at the tower base where the maximum global loads are acting. This is due to high static safety factor. The design life of the FOWT tower of 20 years is sufficient for fatigue. In the following section, the static analysis of the tower under global loads will be performed to obtain the static safety factors.

### 3.5. Static Analysis

#### 3.5.1. Static loads

As mentioned before, the maximum internal global load acting on the FRP tower is the bending moment about Y-axis ( $M_y$ ). The maximum peak value of ( $M_y$ ) was selected for the static analysis. The selection interval was set to excluded the linear response at the beginning. The other internal global forces and moments were taken at the same time as the maximum ( $M_y$ ). Figure 3.31 summarizes the method that the global internal moments were selected for the static analysis. Similarly, using the time index for the maximum ( $M_y$ ), the global internal forces were selected.

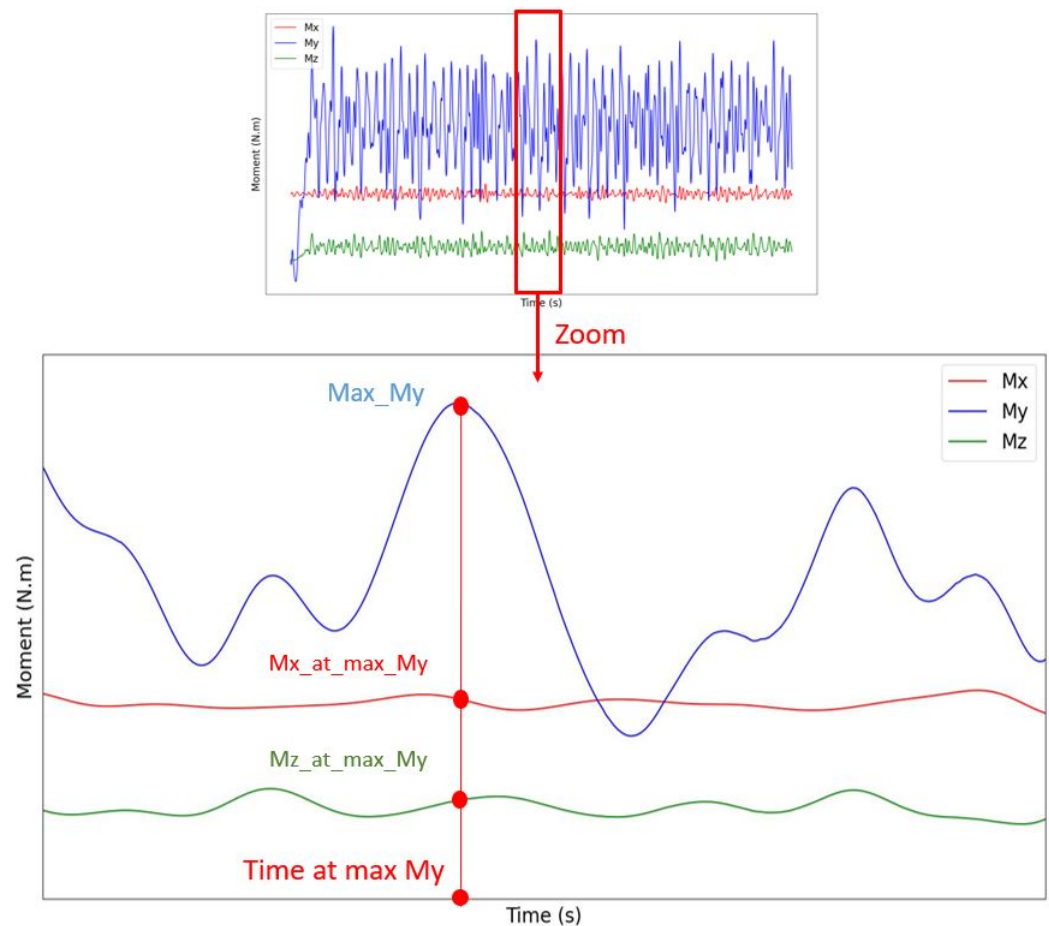


**Figure 3.31:** Selection method of static optimization global internal loads.

Similar to the fatigue damage assessment, two elements were selected for the static analysis. Element under compression at ( $\theta = 161.25^\circ$ ) and element under tension at ( $\theta = 341.25^\circ$ ). Figure 3.32 summarizes the selection method of the in-plane forces ( $N_x$ ) and ( $N_{xy}$ ) for the static analysis.

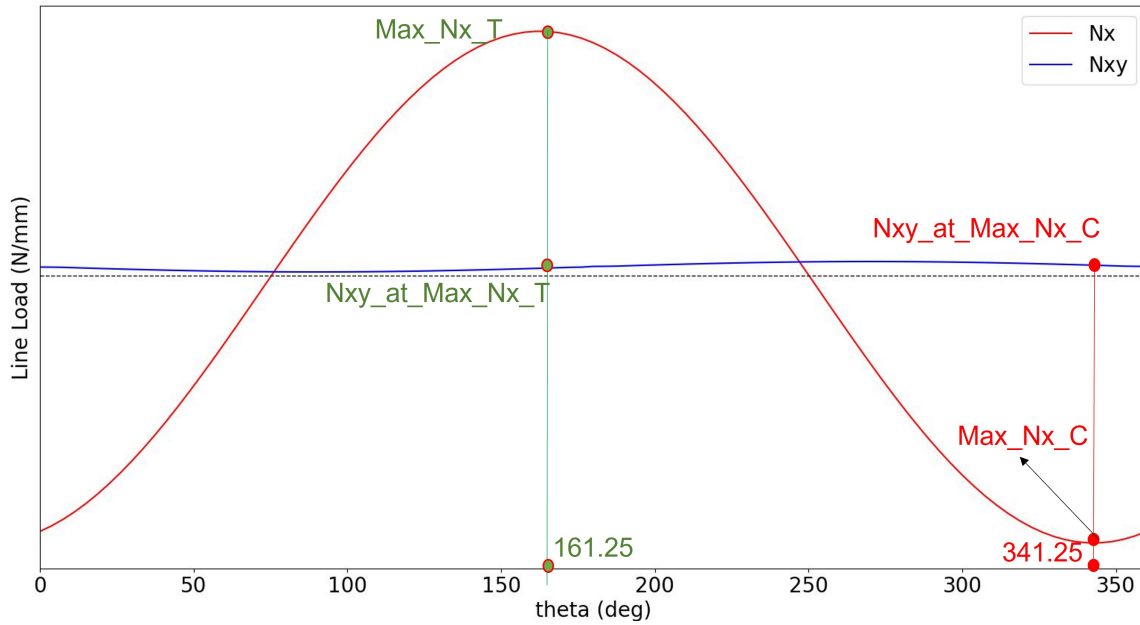


**Figure 3.32:** Selection method of in-plane forces for static analysis.

### 3.5.2. Safety factors

The in-plane forces ( $N_x$ ) and ( $N_{xy}$ ) were used as inputs for ComposeIT. The WSD (working stress design) is followed which require one SF (safety factor) to cover all uncertainties [26]. For WSD, using a combined stress criterion, the safety factor is given by:

$$SF_{CS} \geq C_{CS}C_V C_F C_i C_l \quad (62)$$

And for the maximum stress criterion:

$$SF \geq C_V C_F C_i C_l C_R \quad (63)$$

Where:

- $C_{CS}$  is the partial SF for combined stresses in the individual layers [26].
- $C_R$  is the partial SF for the type of stress in the individual layers [26].
- $C_F$  is the partial SF for the fabrication process [26].
- $C_i$  is the partial SF for the type of loads [26].
- $C_L$  is the partial SF based on the load case. For Normal load case is 1.23 [26]
- $C_V$  is the partial SF taking into account the ageing effect on the laminates. Here, its value is 1.1 for monolithic laminates or face skin above the splash zone [26].

All SFs are taken into account in ComposeIT except  $C_L$ . The value of  $C_V$  in ComposeIT is 1.2. Therefore, to obtain a value of 1.1 we multiply with a correction factor  $\frac{1.1}{1.2}$ . Those

SFs were multiplied by  $N_x$  and  $N_{xy}$  as shown in Eq. 64 and Eq. 65.

$$[N_x]_{ComIT} = [N_x]_{max} \times C_L \times C_V = [N_x]_{max} \times 1.23 \times \frac{1.1}{1.2} \quad (64)$$

$$[N_{xy}]_{ComIT} = [N_{xy}]_{max} \times C_L \times C_V = [N_{xy}]_{max} \times 1.23 \times \frac{1.1}{1.2} \quad (65)$$

### 3.5.3. Results

To demonstrate the results for the static analysis, the tower base section is used. The in-plane loads in Eq. 64 and 65 were used as inputs to ComposeIT. Table 3.3 shows the results of the reference laminate of the tower base section.

The results are expressed in criteria (percent of stress usage) at each layer under a specific type of ply stress. If the criteria is larger than 1, the layer will not respect the criteria expressed in Eq. 66.

$$\text{Criteria} = \frac{\text{SF}}{\text{Ratio}} \quad (66)$$

The ratio is computed in ComposeIT as shown in Eq. 67. If the ratio is less than safety factor, failure will occur.

$$\text{Ratio} = \frac{\text{Rule stress}}{\text{Actual stress}} \quad (67)$$

**Table 3.3:** Criteria of the tower base reference laminate under static load ( $\theta = 341.25^\circ$ ).

Orientation	Layer	$\sigma_1$	$\sigma_2$	$\tau_{12}$	Combined
45	UD300	0.01	0.01	0.04	0.03
-45	UD300	0.03	0	0.04	0.04
0	UD600	0.07	0	0.01	0.05
0	UD300	0.07	0	0.01	0.05
90	UD300	0.01	0.01	0.01	0.02
0	UD600	0.07	0	0.01	0.05

Referring to Table 3.3, the plies criteria are low under compression which shows that they can withstand more stress. The plies criteria were also checked for the element under tension and the values were also low. Table 3.4 shows the plies criteria for an element under tension ( $\theta = 161.25^\circ$ ).

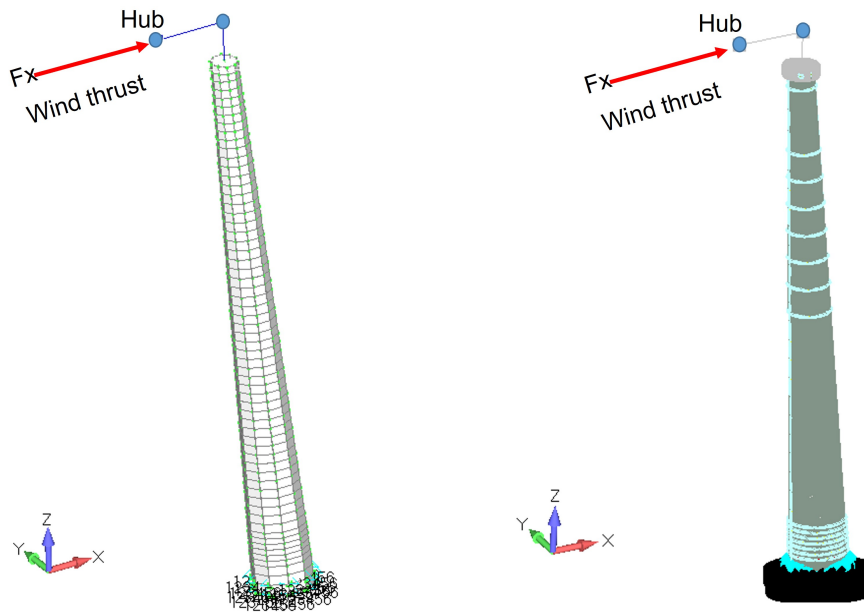
**Table 3.4:** Criteria of the tower base reference laminate under static load ( $\theta = 161.25^\circ$ ).

Orientation	Layer	$\sigma_1$	$\sigma_2$	$\tau_{12}$	Combined
45	UD300	0.02	0.01	0.03	0.04
-45	UD300	0.01	0.01	0.03	0.04
0	UD600	0.04	0	0.01	0.03
0	UD300	0.04	0	0.01	0.03
90	UD300	0.02	0.02	0.01	0.04
0	UD600	0.04	0	0.01	0.03

The ratio for the static loads is computed for both elements under compression and tension and it is greater than 20. It is clear that the ratio is greater than the safety factor ( $SF_{CS}$ ). The fatigue damage was already obtained for the reference laminate in Table 3.1 and 3.2 and the results were very low. This shows that the composite laminate at the tower base section is safe under fatigue damage and static loads.

### 3.6. Tower Deflection

The carbon/epoxy ply characteristics defined in Table 2.1 is used to create the tower laminates (see Figure 2.4) in ComposeIT software [15]. The laminate characteristics of each section are then exported to FEMAP as properties and then they are assigned on the tower surface corresponding to their section. Figure 3.33 shows the applied wind thrust with two meshes for the tower with different element size.

**Figure 3.33:** Tower setup (left) Element size 200 mm (right) Element size 20 mm.

The tower maximum deflection is checked in FEMAP [13]. The maximum thrust load



in Figure 2.23 is applied at the tower hub in FEMAP while fixing the tower base. The nacelle and rotor masses were defined in the tower model. For composite materials, the material orientation needs to be defined prior the analysis according to Figure 3.22. Figure 3.34 shows the fibre  $0^\circ$  ply direction on the tower elements.

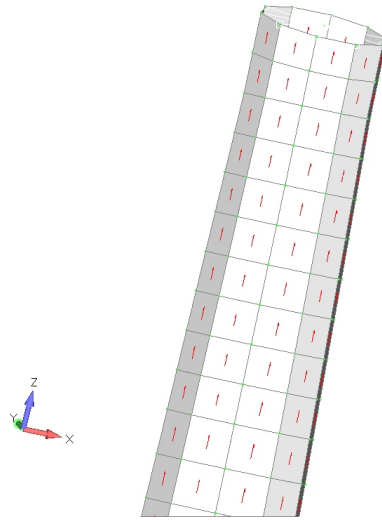


**Figure 3.34:** Material orientation in FEMAP.

Figure 3.35 shows the result of the simulation. With the tower base fixed, the deformed profile shows that the maximum deflection is at the tower top. Similarly, the analysis was repeated for the tower with the fine mesh.

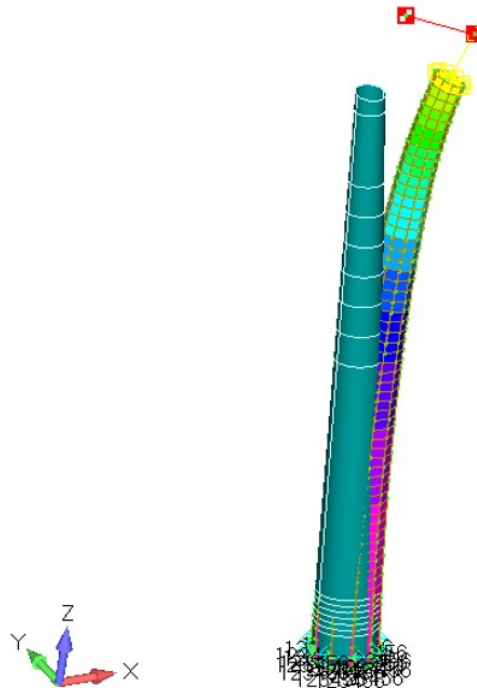


**Figure 3.35:** Tower deflection in FEMAP.

The results for both meshes are shown in Table 3.5. According to [26], the maximum

deflection of the tower should respect the following criteria.

$$150 < \frac{\text{Tower height}}{\text{Max deflection}} \quad (68)$$

**Table 3.5:** Deflection criteria of the tower with different meshes.

Element size [mm]	Deflection Criteria	Check
200	619	Pass
20	674	Pass
Difference [%]	8	

Referring to Table 3.5, the difference of the tower meshes is 8%. The deflection criteria defined in Eq. 68 is respected using the carbon/epoxy reference laminates across the tower. This shows that the tower can sustain static loads and fatigue damage while respecting the deflection criteria.

### 3.7. Buckling

The buckling of the FRP tower was checked with the composite laminates in FEMAP under the maximum wind thrust with fixed tower base. The same tower model in Figure 3.33 was used for the buckling analysis. Figure 3.36 shows the post-process of the 1st buckling mode for the fine mesh model in FEMAP. The profile of the other modes are shown in Appendix B.

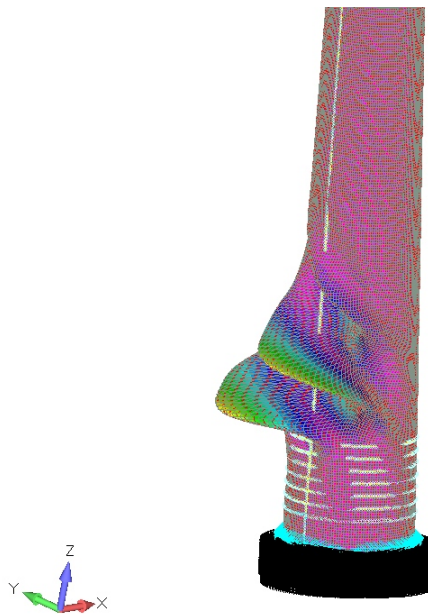


**Figure 3.36:** First buckling mode of the tower (element size: 20mm).

**Table 3.6:** Buckling load factors for both tower mesh.

Buckling Mode	Buckling load factor	
	Element size: 200 mm	Element size: 20 mm
1	-104.79	-73.67
2	105.35	-73.68
3	-105.83	74.61
4	106.31	74.69
5	-109.67	75.21

Table 3.6 shows the buckling load factor of the FRP tower for the first five buckling modes. There is a significant difference when using different element size for the mesh. The load factor value is compared with the buckling safety factor according to [26]. The buckling safety factor is expressed as:

$$SF_B \geq C_{Buck} C_V C_F C_i C_l \quad (69)$$

Where,  $C_{Buck}$  is the partial SF for laminate panel buckling taken equal to 1.45. The buckling SF is computed according to Eq. 69 and results in a value of 2.26. This value is compared to the obtained load factors in Table 3.6. It is clear that the obtained load factor for the fine mesh (Element size: 20 mm) is significantly greater than the calculated SF in Eq. 69. The results shows that the FRP tower laminates respect the buckling criteria.

### 3.8. Modal Analysis

The dynamic characteristics of structures can be found using modal analysis either by structural testing or Finite Element Methods (FEM) simulation. These characteristics depends on the structure stiffness, mass and damping [27].

One important parameter taken from the structure's modal analysis is the natural frequency (eigenvalues) and its associated mode shape (eigenmodes). It is important to perform modal analysis of a structure to know its natural frequency to avoid coinciding with external exciting frequencies.

In this thesis, the modal analysis of the FOWT's tower is performed. The modal analysis for the tower is carried out using FEMAP software [13]. Figure 2.2 shows the tower model in FEMAP. Referring to Figure 2.4, the composite tower is made with variable laminates across its height. The tower lay up data is provided by the FibreGY partners [10].

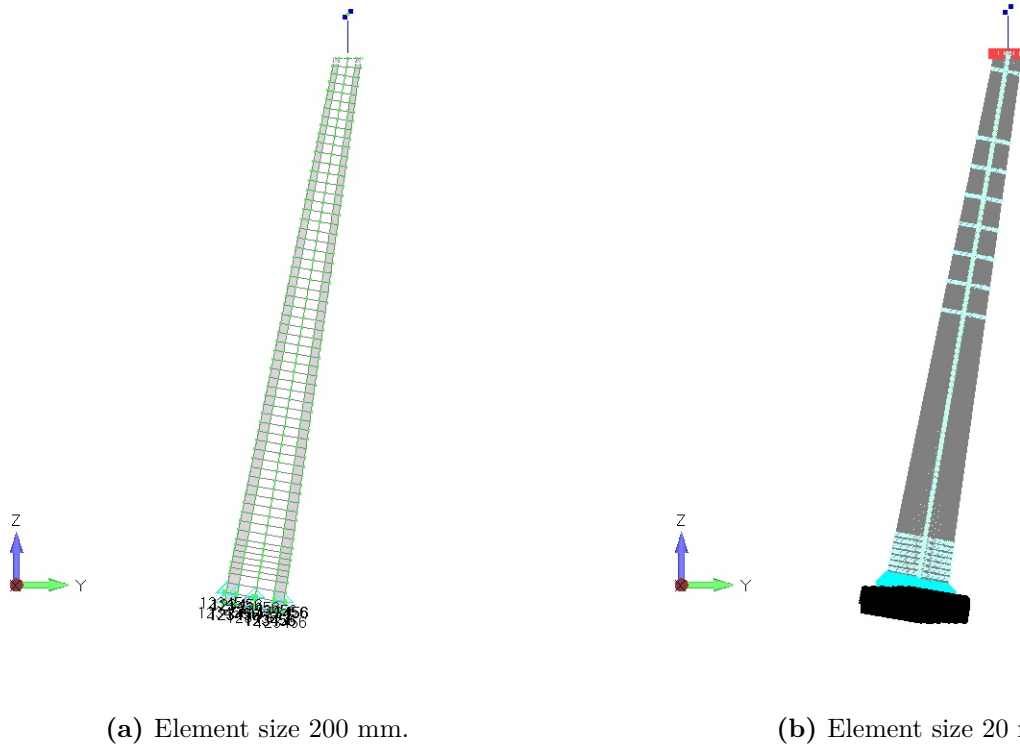


**Figure 3.37:** FRP tower mesh in FEMAP.

Figure 3.38 shows the mode shape of mode 1 in FEMAP which shows a bending mode of the tower. Other mode shapes of the tower are shown in Appendix C. Table 3.7 shows the eigenvalues (natural frequencies) of the FRP tower with slight difference between the two meshes.

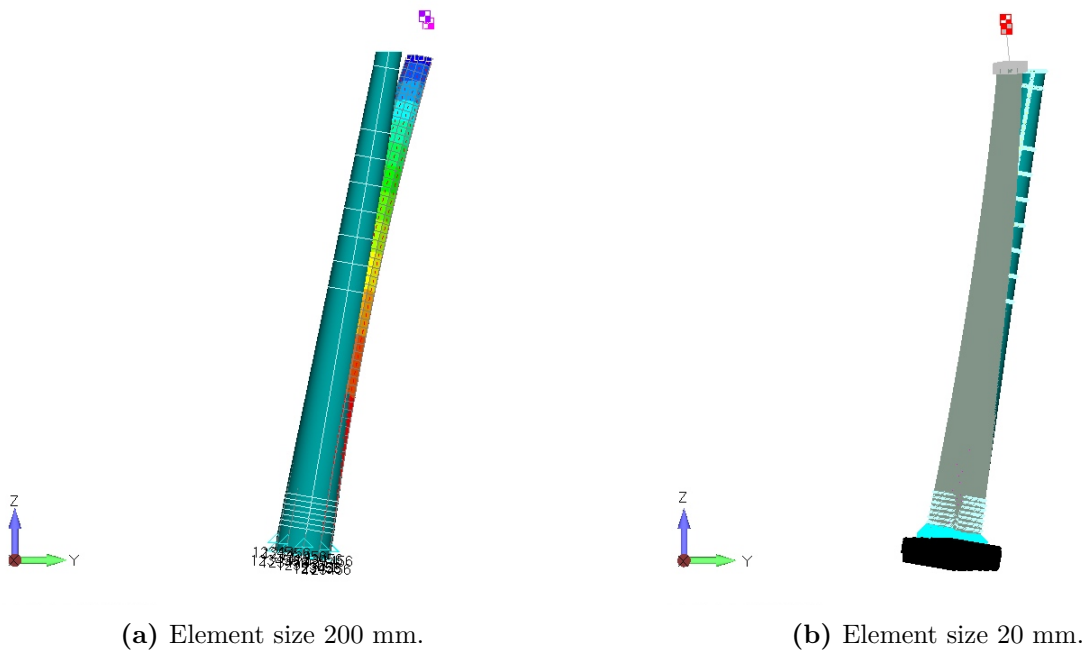


**Figure 3.38:** First mode shape the FRP tower in FEMAP.

**Table 3.7:** Eigenvalues (natural frequencies) of the FRP tower.

Mode	Natural Frequency [Hz]	
	Element size: 200 mm	Element size: 20mm
1	2.78	2.91
2	2.81	2.92
3	12.63	13.28
4	31.49	32.75
5	42.88	44.13
6	55.7	56.177
7	65.52	62.48
8	65.83	62.6
9	75.97	77.54
10	92.06	88.97

The natural frequencies obtained in Table 3.7 are shown here to showcase the values. In this thesis, it was not checked if the natural frequencies would lead to problems in the design.

### 3.9. Summary

In this section, the results of the hydrodynamic and global response of the FOWT were presented. The global internal loads from OPERA was used as inputs for the analytical model to obtain the ply stresses. The fatigue tool was used to compute the damage in the Fibre and matrix and the 20 years design life of the FOWT is sufficient. The FRP tower was checked under static loads and the obtained static safety factors are high. The deflection and buckling of the FRP tower were checked and both respect the design guidelines criteria. Finally, the eigenmodes and eigenvalues of the FRP tower were obtained and checked with two tower meshes. The results in this section shows that the FRP tower has margin for optimization for static loads and fatigue damage. Therefore, the following section demonstrates the design optimization of the FRP tower.

## 4. Design Optimization

In this section, the design optimization of the FRP tower will be performed. The material used is carbon fibre with epoxy resin as defined in Section 2.2. As a demonstration of the optimization process, the tower base section will be used. BV software ComposeIT [15] was used to perform the static design optimization to obtain the static safety factor. At each static optimization iteration, the fatigue damage will be checked. Both elements under compression and tension were checked against static and fatigue loads. The process was repeated for the other sections of the tower. The selected optimized laminates will be checked for the deflection criteria and buckling. Finally, modal analysis for the selected optimized section will be carried out and compared with the reference laminate.

### 4.1. Static and Fatigue Optimization

The Carbon fibre with epoxy resin laminates were created in ComposeIT for each section in the FRP tower according to Figure 2.4 and Table 2.2. Each section of the composite tower has different thickness and number of plies with more thickness at the tower base and less at the tower top. Using the plies defined in Table 2.8, all laminates were created. Each laminate has specific sequence of plies with different fibre orientation. The optimization was carried out by removing one sequence at a time. The optimization process demonstrated here will be carried out for an element under compression ( $\theta = 341.25^\circ$ ). The final optimized section will be checked against tension for ( $\theta = 161.25^\circ$ ) element.

A first optimization attempt was carried by removing one sequence of plies from both sides of the laminate. Since the laminate thickness was reduced, the cross sectional area of the tower base section was also reduced. Therefore, the in-plane forces ( $N_x$ ) and ( $N_{xy}$ ) were recomputed and used again as inputs for the new laminate. Table 4.1 shows the first static optimization attempt for the tower base section with 23% thickness reduction of the reference laminate.

**Table 4.1:** Criteria of the tower base 1<sup>st</sup> optimization under static load ( $\theta = 341.25^\circ$ ).

Orientation	Layer	$\sigma_1$	$\sigma_2$	$\tau_{12}$	Combined
45	UD300	0.02	0.01	0.05	0.04
-45	UD300	0.05	0	0.05	0.05
0	UD600	0.09	0	0.01	0.06
0	UD300	0.09	0	0.01	0.06
90	UD300	0.02	0.01	0.01	0.02
0	UD600	0.09	0	0.01	0.06

After the first optimization, the fatigue damage of the optimized laminate was checked to ensure the laminate can withstand fatigue beside static loads. Table 4.2 shows the fatigue damage of some plies at the tower base in element ( $\theta = 341.25^\circ$ ).

**Table 4.2:** Fatigue damage at the tower base with 1<sup>st</sup> optimization ( $\theta = 341.25^\circ$ ).

Ply Orientation	Matrix	Fibre
45	3.1E-14	6.2E-28
-45	1.2E-14	8.7E-32
0	7.8E-18	1.8E-31
90	5.7E-16	9.5E-21

The first optimized section of the tower base can withstand both fatigue and static loads according to Table 4.1 and 4.2. Therefore, a second optimization attempt was performed by removing another sequence of plies for both sides of the laminate. Table 4.3 shows the second static optimization attempt.

**Table 4.3:** Criteria of the tower base 2<sup>nd</sup> optimization under static load ( $\theta = 341.25^\circ$ ).

Orientation	Layer	$\sigma_1$	$\sigma_2$	$\tau_{12}$	Combined
45	UD300	0.02	0.01	0.06	0.06
-45	UD300	0.06	0.01	0.06	0.07
0	UD600	0.12	0	0.02	0.09
0	UD300	0.12	0	0.02	0.09
90	UD300	0.02	0.02	0.02	0.03
0	UD600	0.12	0	0.02	0.09

The fatigue damage of the second optimization was checked. Table 4.4 shows the fatigue damage of the 2nd optimized section at the tower base.

**Table 4.4:** Fatigue damage at the tower base with 2<sup>nd</sup> optimization ( $\theta = 341.25^\circ$ ).

Ply Orientation	Matrix	Fibre
45	4.0E-12	5.2E-27
-45	1.4E-12	3.0E-31
0	3.7E-17	1.1E-30
90	4.0E-14	1.8E-20

Referring to Table 4.3 and 4.4, the 2nd optimized section of the tower base is still sufficient to withstand static and fatigue loads. Therefore, a 3rd optimization was made for the tower base section. Table 4.5 shows the third static optimization attempt.

**Table 4.5:** Criteria of the tower base 3<sup>rd</sup> optimization under static load ( $\theta = 341.25^\circ$ ).

Orientation	Layer	$\sigma_1$	$\sigma_2$	$\tau_{12}$	Combined
45	UD300	0.03	0.02	0.11	0.09
-45	UD300	0.11	0.01	0.11	0.12
0	UD600	0.21	0	0.03	0.15
0	UD300	0.21	0	0.03	0.15
90	UD300	0.04	0.03	0.03	0.06
0	UD600	0.21	0	0.03	0.15

The 3rd optimized section of the tower base was checked for fatigue damage. Table 4.6 shows the fatigue damage of some plies of the 3rd optimized section at the tower base.

**Table 4.6:** Fatigue damage at the tower base with 3<sup>rd</sup> optimization ( $\theta = 341.25^\circ$ ).

Ply Orientation	Matrix	Fibre
45	1.0E-08	5.2E-25
-45	3.1E-09	8.1E-30
0	5.0E-15	1.2E-28
90	1.5E-10	9.1E-20

Referring to Table 4.5 and 4.6, the 3rd optimized section of the tower base is still sufficient to withstand static and fatigue loads. A 4th optimization attempt was made for the tower base section. Table 4.7 shows the 4th static optimization.

**Table 4.7:** Criteria of the tower base 4<sup>th</sup> optimization under static load ( $\theta = 341.25^\circ$ ).

Orientation	Layer	$\sigma_1$	$\sigma_2$	$\tau_{12}$	Combined
45	UD300	0.06	0.03	0.15	0.13
-45	UD300	0.14	0.02	0.15	0.16
0	UD600	0.28	0	0.04	0.2
0	UD300	0.28	0	0.04	0.2
90	UD300	0.06	0.04	0.04	0.08
0	UD600	0.28	0	0.04	0.2

The 4th optimized section of the tower base was checked for fatigue damage. Table 4.8 shows the fatigue damage of some plies of the 4th optimized section at the tower base.



**Table 4.8:** Fatigue damage at the tower base with 4<sup>th</sup> optimization ( $\theta = 341.25^\circ$ ).

Ply Orientation	Matrix	Fibre
45	7.8E-07	1.5E-28
-45	3.0E-07	3.2E-29
0	1.2E-14	6.3E-27
90	5.3E-09	3.9E-19

The 4th optimized section for the tower base still has some margin for static loads and fatigue damage as shown in Table 4.7 and 4.8. At this stage, one 0° UD ply was removed from the end of the sequence and the laminate was tested against static loads. Table 4.9 shows the 5th static optimization.

**Table 4.9:** Criteria of the tower base 5<sup>th</sup> optimization under static load ( $\theta = 341.25^\circ$ ).

Orientation	Layer	$\sigma_1$	$\sigma_2$	$\tau_{12}$	Combined
45	UD300	0.11	0.04	0.23	0.21
-45	UD300	0.2	0.03	0.23	0.24
0	UD600	0.44	0.01	0.04	0.31
0	UD300	0.44	0.01	0.04	0.31
90	UD300	0.09	0.07	0.04	0.12

The fatigue damage was checked for the 5th optimized section. Table 4.10 shows the fatigue damage of the 5th optimized section at the tower base.

**Table 4.10:** Fatigue damage at the tower base with 5<sup>th</sup> optimization ( $\theta = 341.25^\circ$ ).

Ply Orientation	Matrix	Fibre
45	4.6E-04	6.8E-31
-45	2.4E-04	4.8E-28
0	3.3E-14	3.4E-23
90	2.0E-06	9.6E-18

The 5th optimized section still can withstand static loads while having low fatigue damage. The tower base section was further optimized by removing one (0°) UD ply from the middle of the sequence. Table 4.11 shows the 6th static optimization.

**Table 4.11:** Criteria of the tower base 6<sup>th</sup> optimization under static load ( $\theta = 341.25^\circ$ ).

Orientation	Layer	$\sigma_1$	$\sigma_2$	$\tau_{12}$	Combined
45	UD300	0.31	0.08	0.54	0.5
-45	UD300	0.41	0.07	0.54	0.54
0	UD300	1.02	0.01	0.04	0.71
90	UD300	0.21	0.16	0.04	0.26

Referring to Table 4.11, the static criteria for ( $0^\circ$ ) UD ply under ( $\sigma_1$ ) exceeded 1 and it did not respect the static criteria. The fatigue damage for the 6th optimized section is also shown in Table 4.12.

**Table 4.12:** Fatigue damage at the tower base with 6<sup>th</sup> optimization ( $\theta = 341.25^\circ$ ).

Ply Orientation	Matrix	Fibre
45	145.64	1.6E-26
-45	103.99	1.7E-23
0	1.1E-13	4.5E-10
90	0.39	7.4E-13

As expected, Table 4.12 shows that ( $45^\circ$  and  $-45^\circ$ ) plies have huge cumulative damage for the matrix which is greater than one. The  $90^\circ$  ply also accumulated some damage with 0.39 but still less than 1. Therefore, the 5th optimized section for the tower base was selected. However, an element under tension ( $\theta = 161.25^\circ$ ) for the 5th optimized section needs to be checked against static criteria and fatigue damage to ensure it withstands tension. Table 4.13 shows the 5th static optimization for an element under tension.

**Table 4.13:** Criteria of the tower base 5<sup>th</sup> optimization under static load ( $\theta = 161.25^\circ$ ).

Orientation	Layer	$\sigma_1$	$\sigma_2$	$\tau_{12}$	Combined
45	UD300	0.12	0.06	0.21	0.23
-45	UD300	0.08	0.08	0.21	0.24
0	UD600	0.28	0	0.03	0.2
0	UD300	0.28	0	0.03	0.2
90	UD300	0.12	0.14	0.03	0.25

The static criteria is respected for an element under tension for the 5th optimized section of the tower base according to 4.13. The fatigue damage was also checked for the element under tension as shown in Table 4.14.

**Table 4.14:** Fatigue damage at the tower base with 5<sup>th</sup> optimization ( $\theta = 161.25^\circ$ ).

Ply Orientation	Matrix	Fibre
45	5.8E-07	3.5E-14
-45	1.5E-06	3.4E-16
0	5.5E-14	6.0E-09
90	6.6E-07	3.4E-26

Referring to Table 4.14, the fatigue damage is low which shows that the 5th optimized section of the tower base for an element under tension is safe under static and fatigue loads. It is worth to note that the fibre accumulated more damage in tension compared to compression while it is the opposite for the matrix according to Table 4.10 and 4.14. Table 4.15 shows the reduction in thickness for each optimization iteration compared to the reference laminate.

**Table 4.15:** Thickness reduction for each optimization iteration.

Laminate	Thickness reduction (%)
Reference	0
Opt 1	23.5
Opt 2	47.0
Opt 3	70.6
Opt 4	76.5
Opt 5	82.4
Opt 6	88.3

## 4.2. Tower Deflection

The tower deflection for the 5th optimized section will be checked in FEMAP similar to Section 3.6. The model set up including the maximum thrust load, nacelle and rotor masses and the fixed tower base will also be used. The 5th optimized laminate was exported from ComposeIT to FEMAP as properties. Then it was assigned for all the tower sections since it had sufficient static and fatigue margins for the tower base where the maximum internal global loads are acting. Only the fine mesh with element size of 20 mm will be shown here. Table 4.16 shows the deflection criteria of the FRP tower with the 5th optimized laminate computed according to Eq. 68.

**Table 4.16:** Deflection criteria of the FRP tower with the 5<sup>th</sup> optimized laminate.

Element size (mm)	Deflection Criteria	Check
20	134	Failed

The results in Table 4.16 shows that the 5th optimized section for static and fatigue loads did not respect the deflection criteria. Therefore, the 4th optimized section was used to check the deflection criteria again. Table 4.17 shows the deflection criteria for the FRP tower with the 4th optimized laminate.

**Table 4.17:** Deflection criteria of the FRP tower with the 4<sup>th</sup> optimized laminate.

Element size (mm)	Deflection Criteria	Check
20	208	Pass

Referring to Table 4.17, the deflection criteria is respected when using the 4th optimized laminate. Therefore, in the following section, it will be used to compute the buckling load factor.

### 4.3. Buckling

The FRP tower is checked for buckling in this section using the 4th optimized laminate. The model setup explained in Section 3.7 will be used. Figure 4.1 shows the first buckling mode of the FRP tower with the optimized laminate using the fine mesh (element size of 20mm). The other buckling modes will be shown in Appendix B.

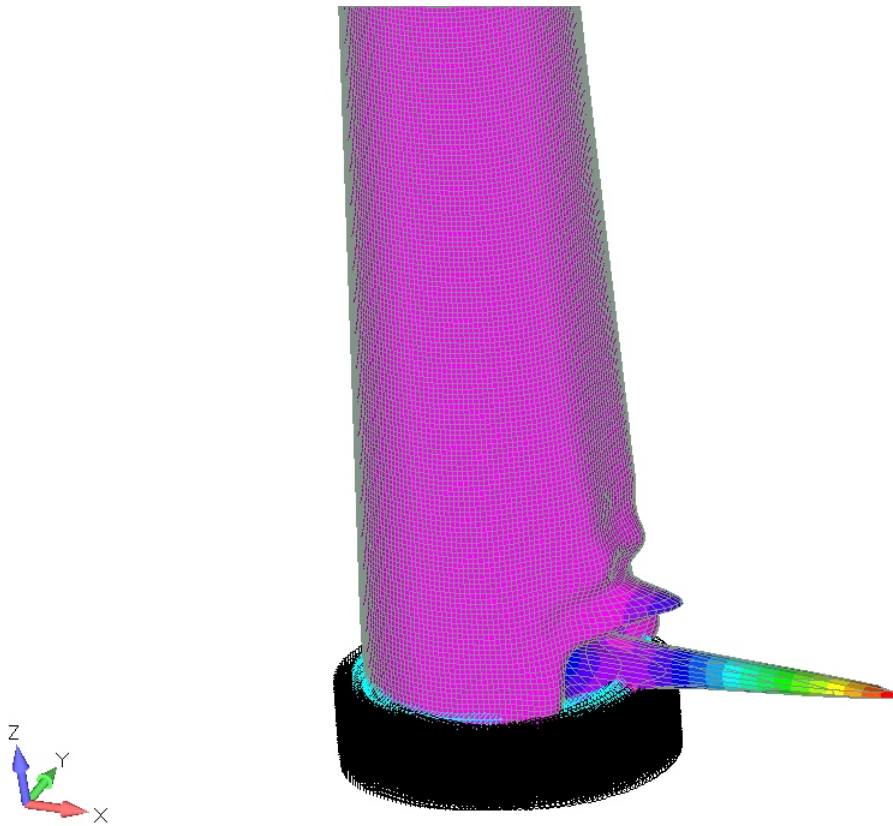


**Figure 4.1:** 1<sup>st</sup> buckling mode of the FRP tower with the 4<sup>th</sup> optimized laminate.

Table 4.18 shows the buckling load factors for five buckling modes. These values are to be compared with the computed buckling safety factor as defined in Eq. 69. The load factors shown in Table 4.18 are greater than 2.26 and thus the buckling criteria is respected.

**Table 4.18:** Buckling load factors with the 4<sup>th</sup> optimized laminate.

Buckling Mode	Load factor
1	6.46
2	-6.49
3	6.78
4	-6.8
5	-7.12

#### 4.4. Modal Analysis

The eigenmodes and eigenvalues for the FRP tower with the 4th optimized laminate will be shown in this section. The same setup in Section 3.8 will be followed. The first mode shape is shown in Figure 4.2. The other mode shapes will be shown in Appendix C.

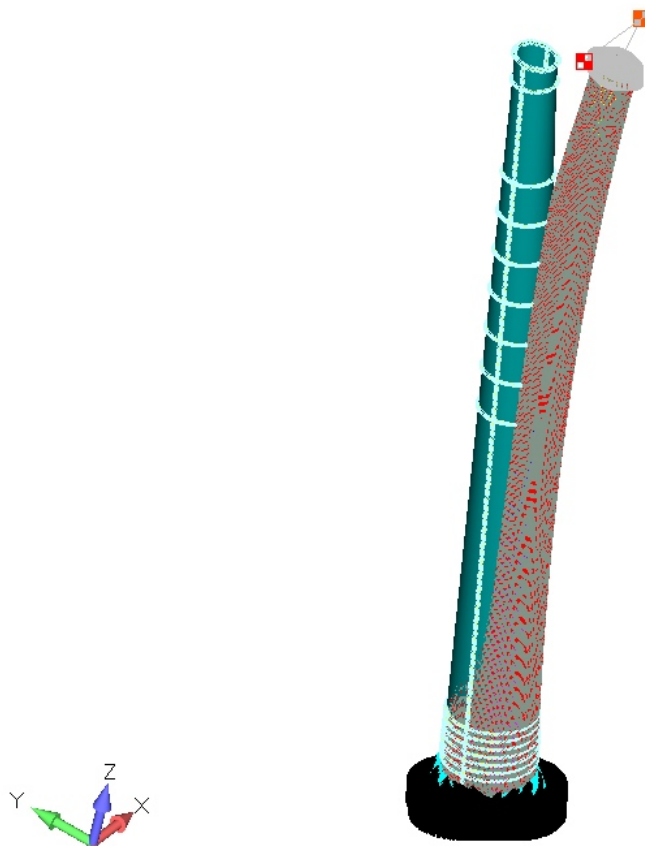


**Figure 4.2:** 1<sup>st</sup> mode shape of the FRP tower with the 4<sup>th</sup> optimized laminate.

Table 4.19 shows the eigenvalues (natural frequencies) of the FRP tower with the reference laminate and the 4th optimized laminate. Referring to the table, the difference in the obtained values are due to the reduction in stiffness of the FRP tower with the optimized laminate as the nacelle and rotor masses do not change.

**Table 4.19:** Comparison of eigenvalues of the FRP tower with two laminates.

Natural Frequency [Hz]			
Mode	Reference laminate	Opt 4	Difference [%]
1	2.91	1.62	44.3
2	2.92	1.63	44.2
3	13.28	8.41	36.7
4	32.75	21.02	35.8
5	44.13	30.96	29.8
6	56.177	31.16	44.5
7	62.48	31.25	50.0
8	62.6	42.35	32.3
9	77.54	47.89	38.2
10	88.97	47.96	46.1

## 4.5. Summary

In this section, the optimization methodology and results of the tower base section were demonstrated. The results show that the developed fatigue tool was able to predict damage in the FRP plies. The 6th optimized section of the tower base failed in both static and fatigue loads. The fatigue damage was more critical in the matrix for the  $45^\circ$  ply with an element under compression ( $\theta = 341.25^\circ$ ). The elements under compression will drive the fatigue design of the composite tower compared to elements under tension which have lower fatigue damage. The 5th optimized section of the tower base was selected since it can withstand both static and fatigue loads. The obtained combined stress static ratio for the 5th optimized section is 9.1 which is greater than the computed combined safety factor ( $SF_{CS}$ ) computed in ComposeIT with a value of 2.81. The 5th optimized section of the tower base was checked for deflection and buckling criteria. Deflection criteria was not respected when using the 5th optimized laminate. With the 4th optimized laminate both deflection and buckling criteria were respected. Thus, the 4th optimized laminate was selected for the whole FRP tower as it can withstand static loads and fatigue damage while respecting the buckling and deflection criteria. Finally, a comparison between the modal analysis of the reference laminate were shown with decrease in the eigenvalues due to reduction of mass. With the 4th optimized laminate, a reduction of approximately 66% of the original FRP tower total weight was achieved.

## 5. CONCLUSION

In this the thesis, the fatigue analysis of Floating Offshore Wind Turbine (FOWT) tower made in composite materials was demonstrated. The scope of the thesis is part of the framework of FibreGY [11] project which aims to enable the use of FRP materials in the offshore renewable sector particularly in offshore wind and tidal platforms. The W2Power FOWT designed by Enerocean [7] was used to replace the towers from steel to FRP materials. The scope of the thesis falls within the work package (WP4) of FibreGY project [11] related to engineering and design guidelines. The objective of the thesis is to use and improve the methodology developed by P. Pathak [12] using Bureau Veritas (BV) software (HydroStar, OPERA and ComposeIT) and BV fatigue [21] and composite [16] guidelines to assess the fatigue life of the FRP tower. The fatigue methodology was improved in this thesis. The summary of the thesis is presented in sections as follows:

- **Hydrodynamic Response of the FOWT**

Added mass, radiation damping, first and second order wave loads and motions of the FOWT were obtained in HydroStar [14]. As an improvement of the work done by P. Pathak [12], the braces were added as Morison elements since HydroStar is a radiation and diffraction software. The influence of Morison elements were noticed in the FOWT motions only, since they were defined in the mechanical module of HydroStar. The output from HydroStar was used as inputs to OPERA to evaluate the global response of the FOWT.

- **Global Response of the FOWT**

BV software OPERA was used to assess the global response of the FOWT platform against environmental loads including wind and waves. In OPERA, each part of the FOWT (i.e. blades, tower, floater, mooring lines etc.) were defined and then assembled. The normal design load case for wind and waves was selected for the fatigue assessment. Several types of loads were applied to different parts of the FOWT according to Table 2.4.

Several verifications were performed in OPERA to ensure that the inputs defined were correct. The stability, motions (RAO) and mooring lines pretension were checked from the simulation outputs in OPERA. BV software Ariane was used to verify the mooring lines pretension in OPERA. Several iterations were performed to obtain the right equilibrium position of the FOWT platform with the correct motions and mooring lines pretension.

The global internal loads at each section along the tower height were obtained. The internal time-series forces and moments at each section of the tower were exported to the analytical Python tool to evaluate the time-series ply stresses.

- **Analytical Model**

To evaluate the ply stresses in a specific section in the tower, the analytical model was developed. It used the global internal loads from OPERA and convert them to line loads acting on the mid-thickness of the laminate. The analytical model was validated with FEMAP software [13] and the results were in agreement. The line loads were then used as in-plane forces in the macro-mechanical analysis to obtain the ply stresses.

The macro-mechanical analysis was used following BV-NR-546 rules [16]. The analysis described in [16] was coded in a Python tool and linked to the analytical model Python script to obtain the ply stresses. To validate the macro-mechanical analysis Python tool, BV software ComposeIT [15] was used and the results were in agreement. Several laminates with complex ply's orientations were also created in the Python tool and compared with ComposeIT. The time-series ply stresses were used as inputs for the fatigue tool.

- **Fatigue Analysis**

BV fatigue guideline [21] was coded in a Python script. The matrix and fibre stresses were computed using the ply stresses. The fatigue tool was validated by generating a variable (compression and tension) time-series signal for the matrix and fibre stresses. The S-N curve interpolation and CFL were successfully demonstrated.

Using the internal global loads from OPERA, the line loads were obtained at each tower section. Two elements were selected for the fatigue analysis of each section. One element under maximum compression ( $\theta = 341.25^\circ$ ) and another under maximum tension ( $\theta = 161.25^\circ$ ). The ply stresses at these elements were computed and used to obtain the matrix and fibre time-series stresses. Using rainflow algorithm, S-N curve interpolation and CFL diagrams, the fatigue damage for 20 years design life was obtained. The fatigue damage of the matrix and fibre was evaluated at the two chosen elements. The process was repeated for each section of the tower. The tower base section was used to demonstrate the fatigue analysis where the maximum internal global loads is acting. The results show that the FRP tower fatigue damage is very low and sufficient for 20 years design life.

The static analysis of the FRP tower was performed using the maximum global internal loads in the time-series signal. The results show that the ratio of the combined stress for each ply is greater than 20. The combined safety factor ( $SF_{CS}$ ) computed in ComposeIT is 2.81. The ratio was compared to the safety factor and it was clearly higher which shows that the laminate can withstand more static loads. The FRP tower was checked against deflection and buckling and it respected both criteria. The eignemodes and eigenvalues were also obtained for the FRP tower.

---



---

Overall, the results obtained show that the FRP tower is safe for static and fatigue design and there is a margin for design optimization.

- **Design Optimization**

The design optimization of the FRP tower was carried out using ComposeIT for the static optimization and the developed Python fatigue tool for the damage. The tower base section was used to demonstrate the design optimization process. Several optimization iterations were performed by reducing the laminate thickness for each iteration. The 6th optimized laminate failed under static loads and fatigue damage. This shows that the developed Python fatigue tool can predict fatigue damage in the FRP laminate. The 5th optimized laminate withstood static loads and fatigue damage but failed against the deflection criteria. Therefore, the 4th optimized laminate was selected. The results show that the 4th optimized laminate was safe under static loads and fatigue damage while respecting the deflection and buckling criteria. The 4th optimized laminate was chosen for the FRP tower with 76.5% reduction in thickness compared to the original laminate. Using the 4th optimized laminate for every section on the FRP tower, the weight of the FRP tower was reduced with approximately 66% of the reference total weight of the FRP tower.

- **Concluding Remarks**

The work in this thesis showed that the use of FRP towers for FOWT industry is feasible which aligns with FibreGY [11] project objective. The developed methodology and Python tools were able to predict fatigue damage and allowed design optimization of FOWT towers using FRP materials. The tools developed in the thesis were proven to be efficient and less time-consuming. The future work of this thesis is to use different FRP materials like glass fibre and assess the fatigue life of the FRP tower. The global response of the FOWT in OPERA can be evaluated using flexible FRP tower compared to the rigid analysis. More design load cases can also be performed to look for severe conditions.

---

## References

- [1] Carlos V.C. Weiss, Raúl Guanche, Bárbara Ondiviela, Omar F. Castellanos, and José Juanes. Marine renewable energy potential: A global perspective for offshore wind and wave exploitation. *Energy Conversion and Management*, 177:43–54, 2018.
  - [2] International Renewable Energy Agency (IRENA). Capacity and generation (statistics time series), 2018.
  - [3] Nuno Bento and Margarida Fontes. Emergence of floating offshore wind energy: Technology and industry. *Renewable and Sustainable Energy Reviews*, 99:66–82, 2019.
  - [4] Mohammad Barooni, Turaj Ashuri, Deniz Velioglu Sogut, Stephen Wood, and Shiva Ghaderpour Taleghani. Floating offshore wind turbines: Current status and future prospects. *Energies*, 16(1), 2023.
  - [5] Orsted. Orsted - Floating Offshore Wind Energy, 2023.
  - [6] Empire Engineering. Semi-Submersible, Spar and TLP – how to select floating wind foundation types, Aug 27, 2021. Accessed on 25 August 2023.
  - [7] Enerocean. Enerocean - W2Power, 2023.
  - [8] S. Butterfield, W. Musial, J. Jonkman, and P. Sclavounos. Engineering challenges for floating offshore wind turbines. In *Presented at the 2005 Copenhagen Offshore Wind Conference*, number NREL/CP-500-38776, Copenhagen, Denmark, October 26–28, 2005 2005. National Renewable Energy Laboratory and Massachusetts Institute of Technology. Conference Paper.
  - [9] Xuan Li and Wei Zhang. Long-term fatigue damage assessment for a floating offshore wind turbine under realistic environmental conditions. *Renewable Energy*, 159:570–584, 2020.
  - [10] Project XYZ. D4.3 (wp4): W2power tower’s demonstrator design for its construction in frp. Technical Report D4.3, FibreGY, 2023. Accessed May 14, 2023.
  - [11] Fibregy. Fibre reinforced polymers composites for offshore renewable industry, 2020.
  - [12] Pharindra Pathak. Fatigue methodology for floating offshore wind power platform and turbine tower in composite materials. Master’s thesis, Ecole Centrale de Nantes, August 2022.
  - [13] FEMAP. Computer software, 2022. Version 2022.1.
  - [14] BV HydroSTAR For Expert v8.10, Reference Guide and Tutorial for Naval and Offshore Hydrodynamic Application, BV Marine and Offshore, 2021.
-

- 
- [15] BV ComposeIT. Computer software, 2022. Version 3.2.
- [16] BV - NR546 - Hull in Composite Materials and Plywood, Material Approval, Design Principles, Construction and Survey, October 2021.
- [17] A. Subbulakshmi, Mohit Verma, M. Keerthana, Saptarshi Sasmal, P. Harikrishna, and Santosh Kapuria. Recent advances in experimental and numerical methods for dynamic analysis of floating offshore wind turbines — an integrated review. 164:112525.
- [18] BV OPERA. Computer software, 2023. latest version.
- [19] International Electrotechnical Commission (IEC). Design requirements for small wind turbines. International Standard 61400-2, IEC, 2006.
- [20] Bureau Veritas. Classification and certification of floating offshore wind turbines. Rule Note NI 572 DT R02, Bureau Veritas, January 2019.
- [21] BV Composite Materials Section, Composite Fatigue Guidelines, V-0.4, BV Marine and Offshore, May 2023.
- [22] Shock & Vibration 39. Rainflow cycle counting for random vibration fatigue analysis. Technical Report 39, Shock & Vibration, 2017.
- [23] M Kawai and N Itoh. A failure-mode based anisomorphic constant life diagram for a unidirectional carbon/epoxy laminate under off-axis fatigue loading at room temperature. 48(5):571–592.
- [24] O. M. Faltinsen. *Sea Loads on Ships and Offshore Structures*. Cambridge University Press, 1990.
- [25] Bureau Veritas. *Ariane Advanced Mooring Software*, June 2023. Release Date: June 1, 2023. Version Number: 8.2.
- [26] Bureau Veritas. Development, engineering, production and life cycle management of improved FIBRE-based material solutions for the structure and functional components of large offshore wind energy and tidal power platforms. Technical Report D4.7 (WP4), FibreGY, 2023.
- [27] Siemens PLM. Modal analysis. <https://www.plm.automation.siemens.com/global/en/our-story/glossary/modal-analysis/13172>, n.d. Accessed May 14, 2023.
-

---

# APPENDIX

## A. Appendix A

### A.1. Torsion line load

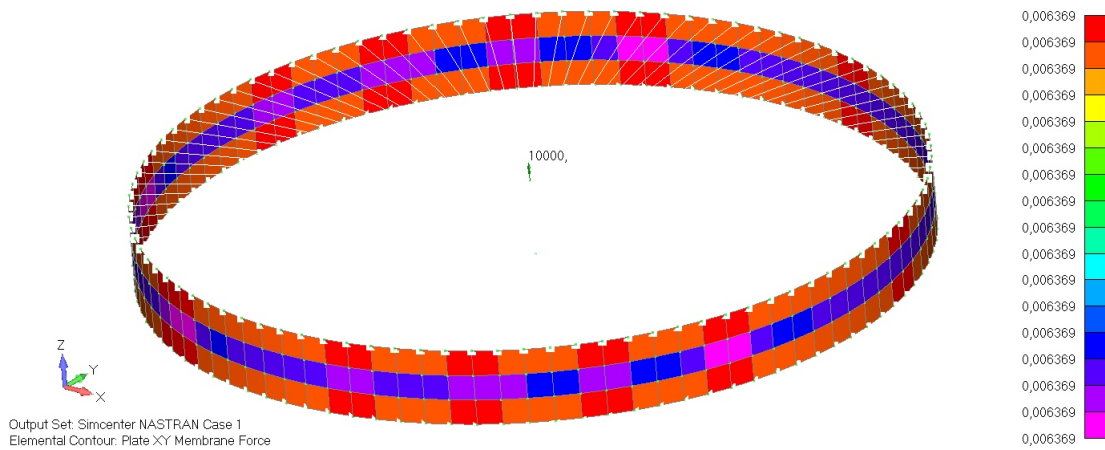


Figure A.1: FEMAP Torsion line load ( $\zeta_{Mz}$ ) due to  $M_z$ .

### A.2. Bending line load

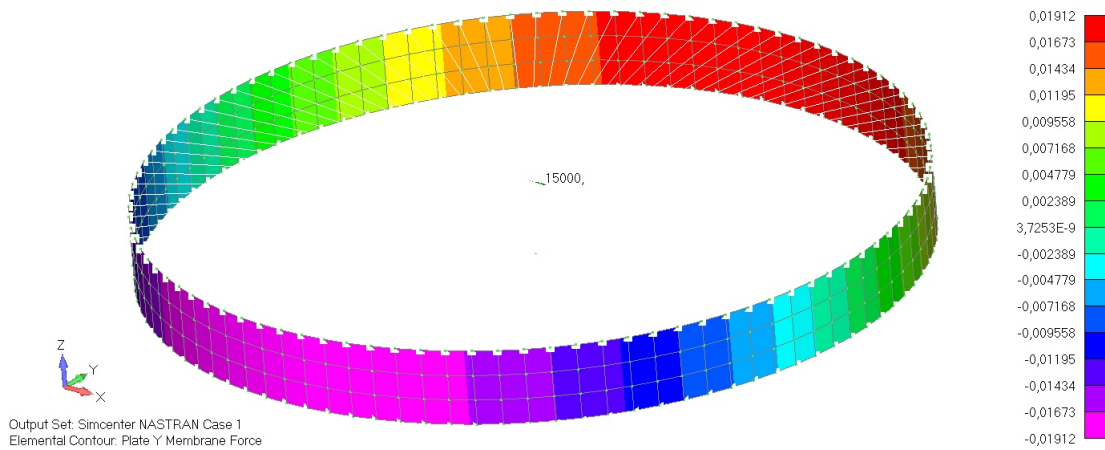


Figure A.2: FEMAP Bending line load ( $\zeta_{Mx}$ ) due to  $M_x$ .

---

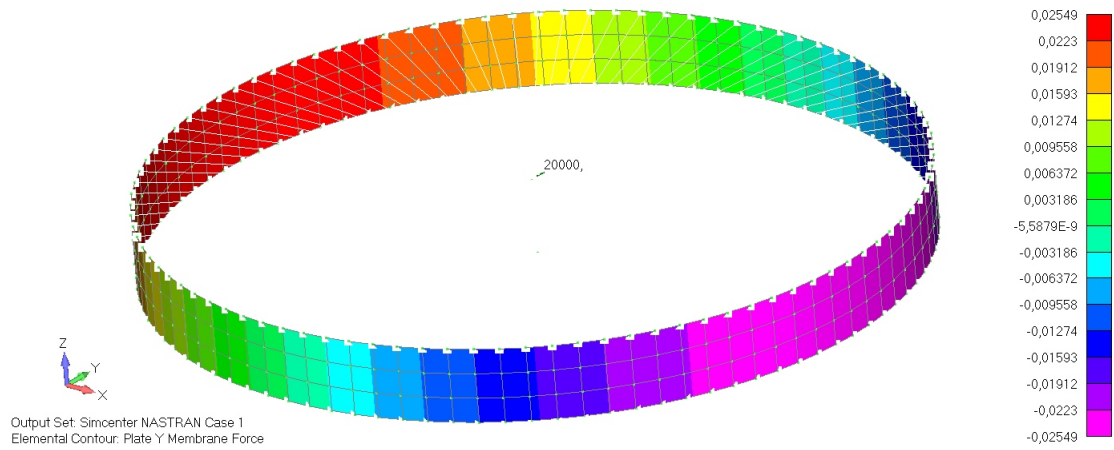


Figure A.3: FEMAP Bending line load ( $\zeta_{M_y}$ ) due to  $M_y$ .

### A.3. Shear line load

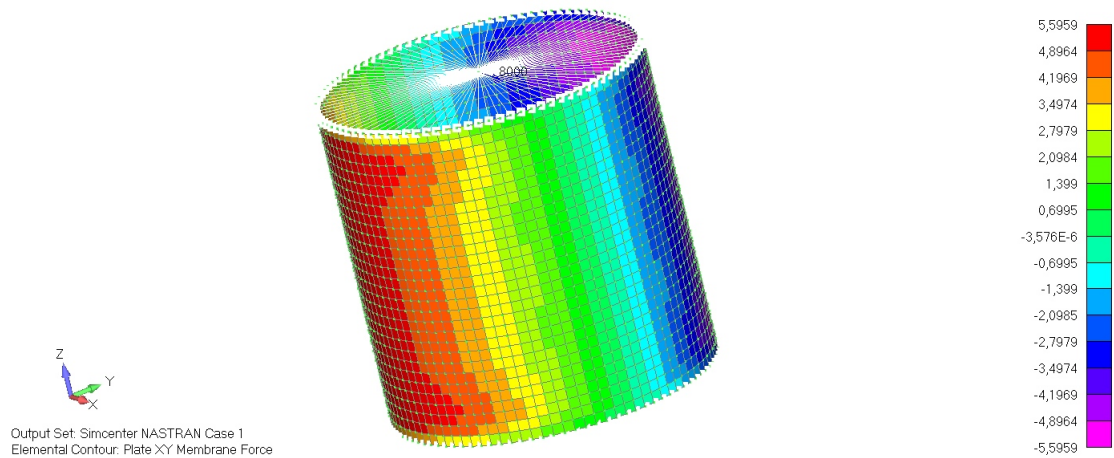


Figure A.4: FEMAP Shear line load ( $\zeta_{F_x}$ ) due to  $F_x$ .

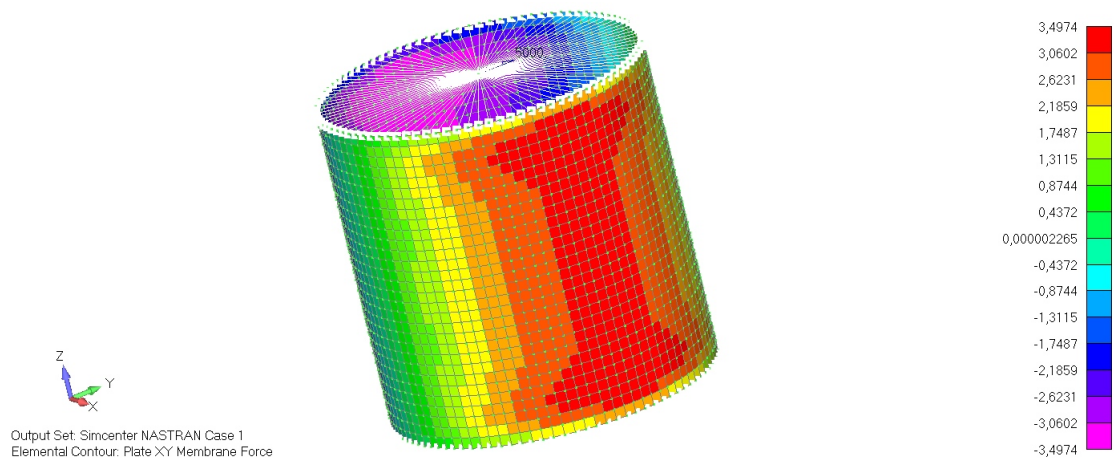


Figure A.5: FEMAP Shear line load ( $\zeta_{F_y}$ ) due to  $F_y$ .

---

# B. Appendix B

## B.1. Buckling Modes

### B.1.1. Reference laminate

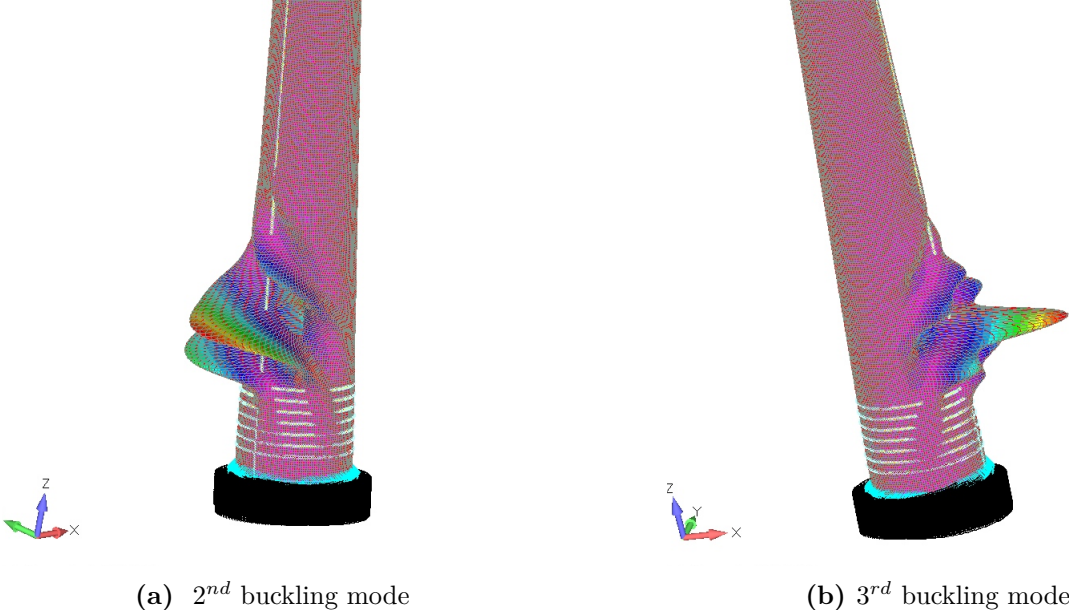


**Figure B.1:** Buckling modes of the FRP tower (Element size 20 mm)

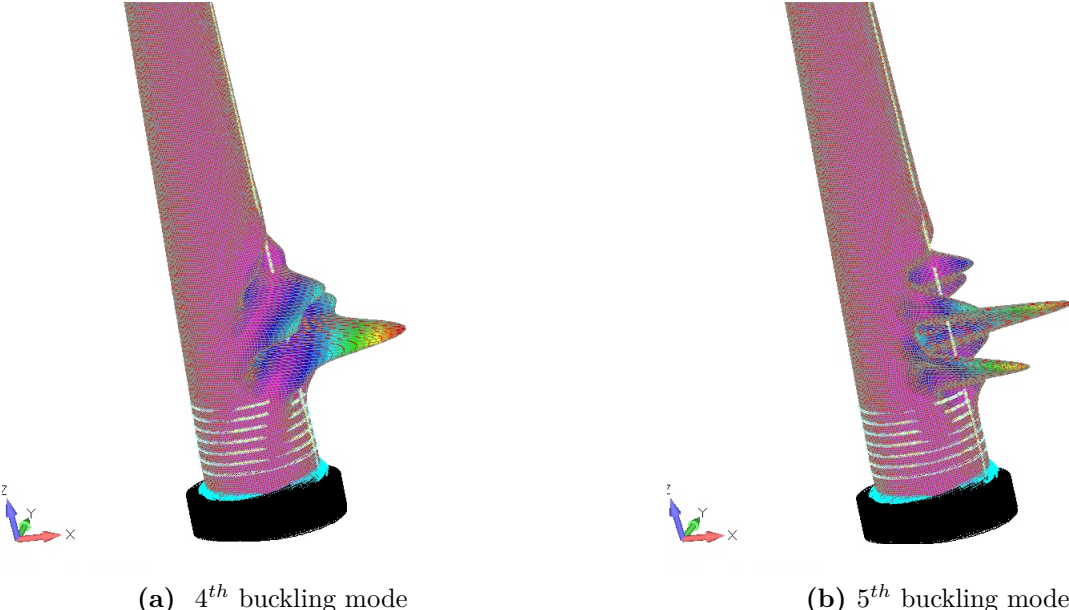


**Figure B.2:** Buckling modes of the FRP tower (Element size 20 mm)

---

---

B.1.2. 4th Optimized laminate

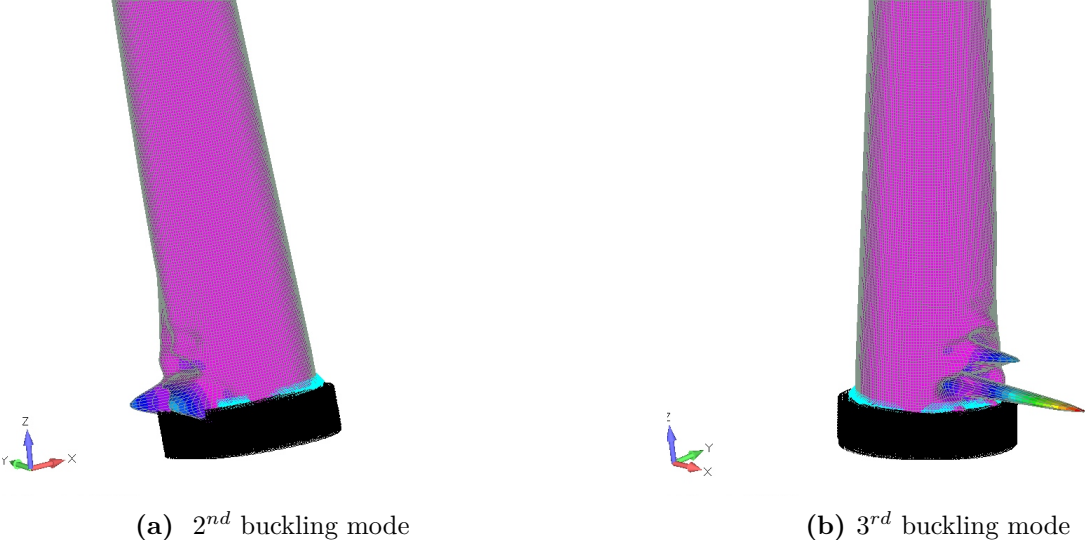


**Figure B.3:** Buckling modes of the optimized FRP tower (Element size 20 mm)

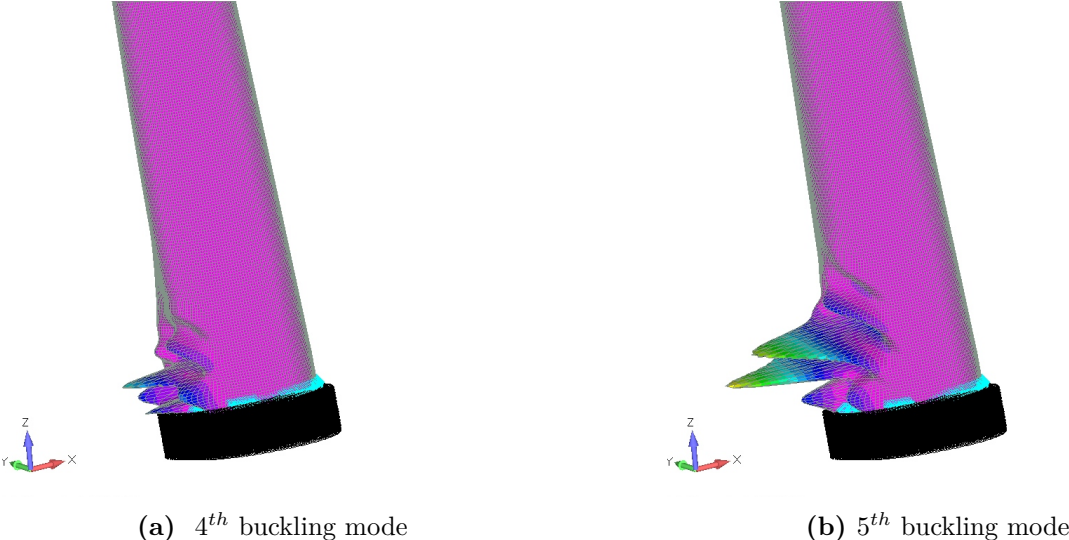


**Figure B.4:** Buckling modes of the optimized FRP tower (Element size 20 mm)

---

---

# C. Appendix C

## C.1. Mode shapes (Eigenmodes)

### C.1.1. Reference laminate

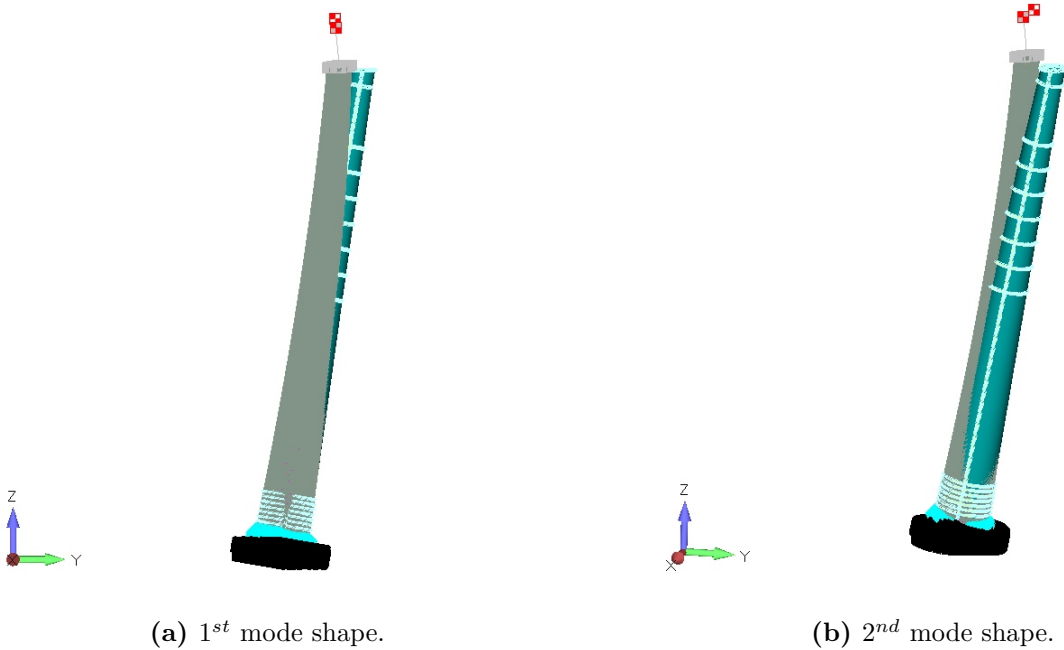


Figure C.1: Mode shapes the FRP tower in FEMAP.

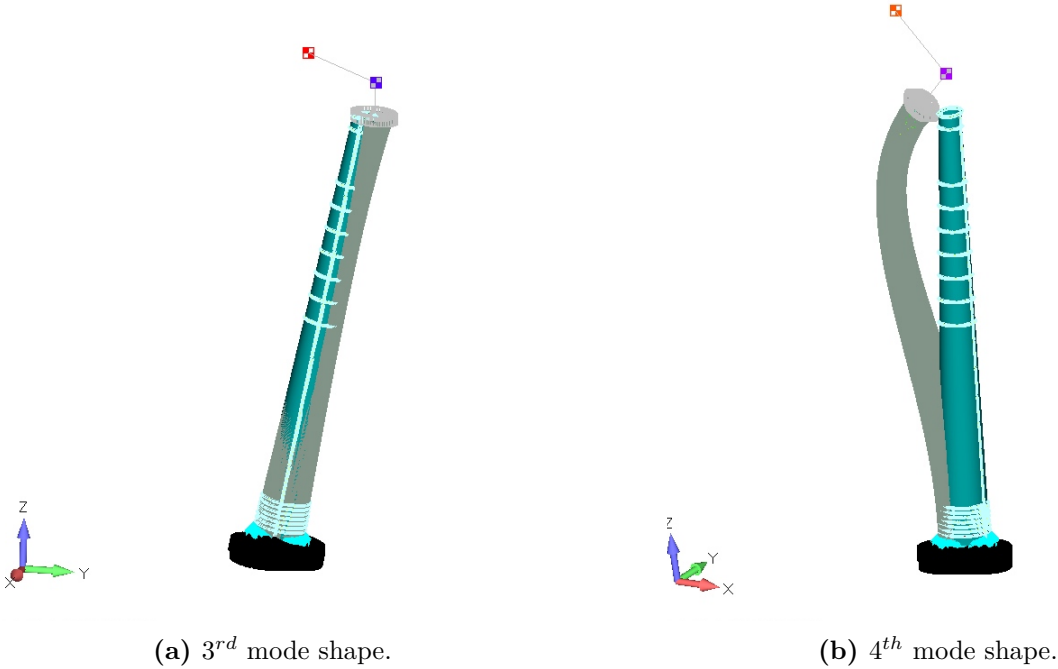
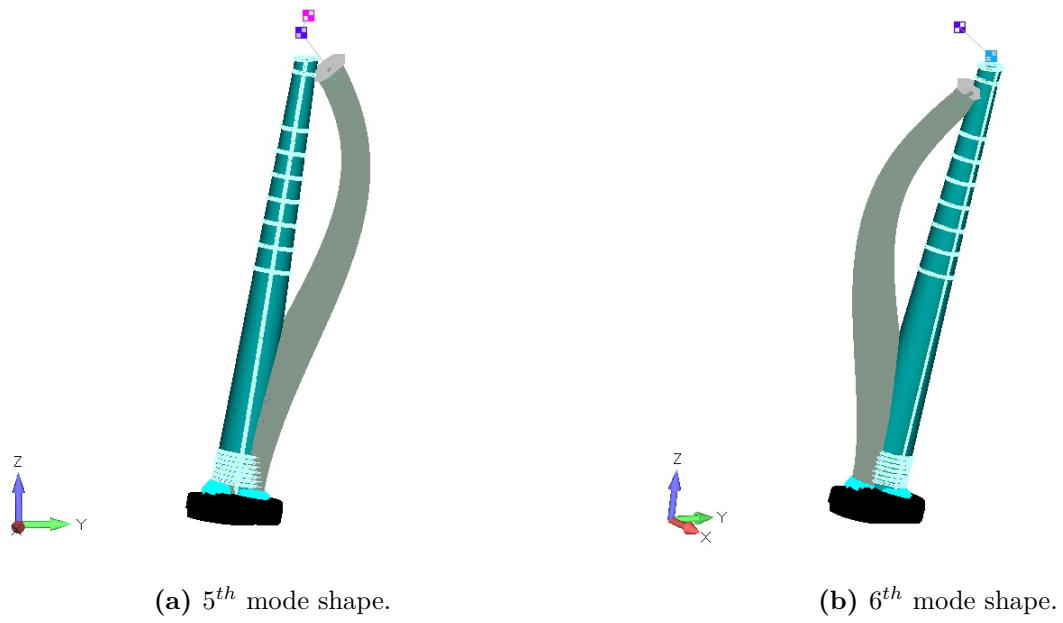


Figure C.2: Mode shapes the FRP tower in FEMAP.

---





**Figure C.3:** Mode shapes the FRP tower in FEMAP.

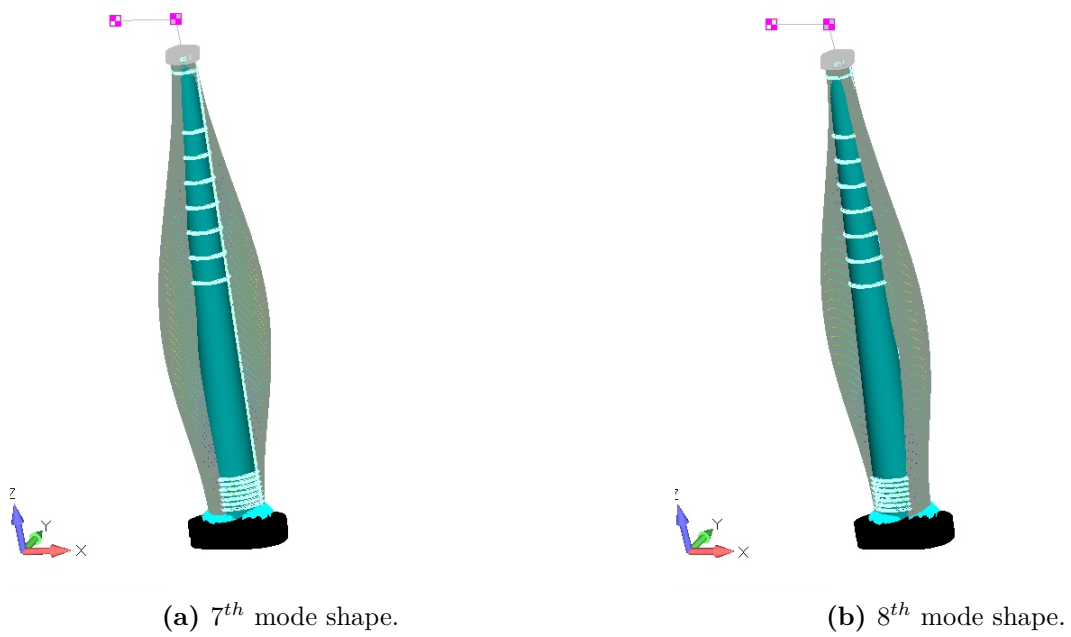


**Figure C.4:** Mode shapes the FRP tower in FEMAP.

---

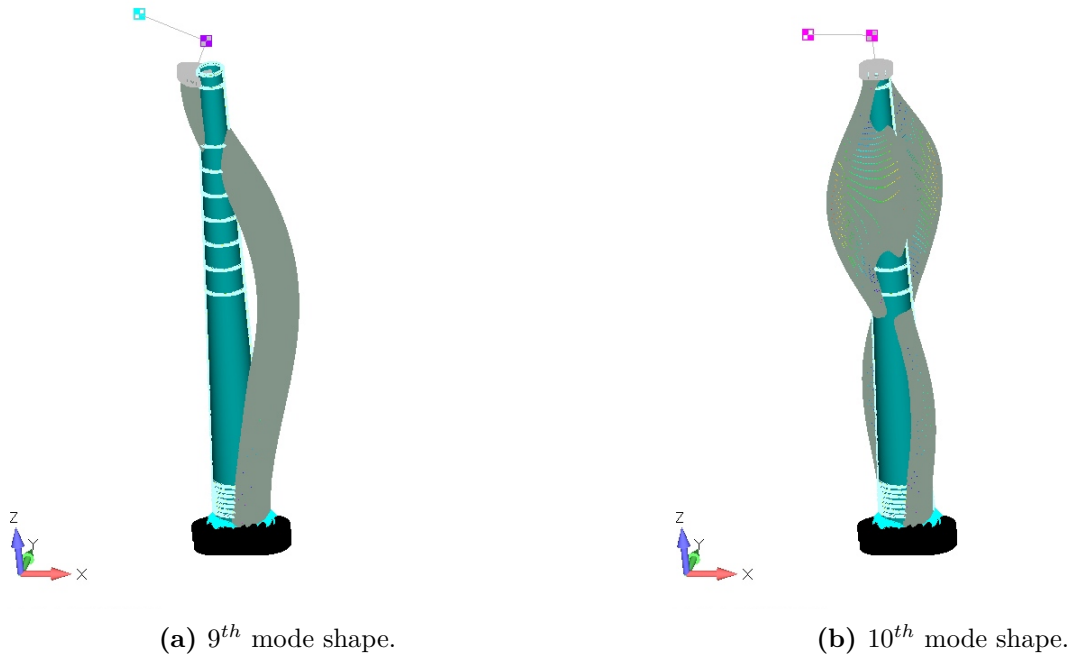


**Figure C.5:** Mode shapes the FRP tower in FEMAP.

### C.1.2. 4th Optimized laminate

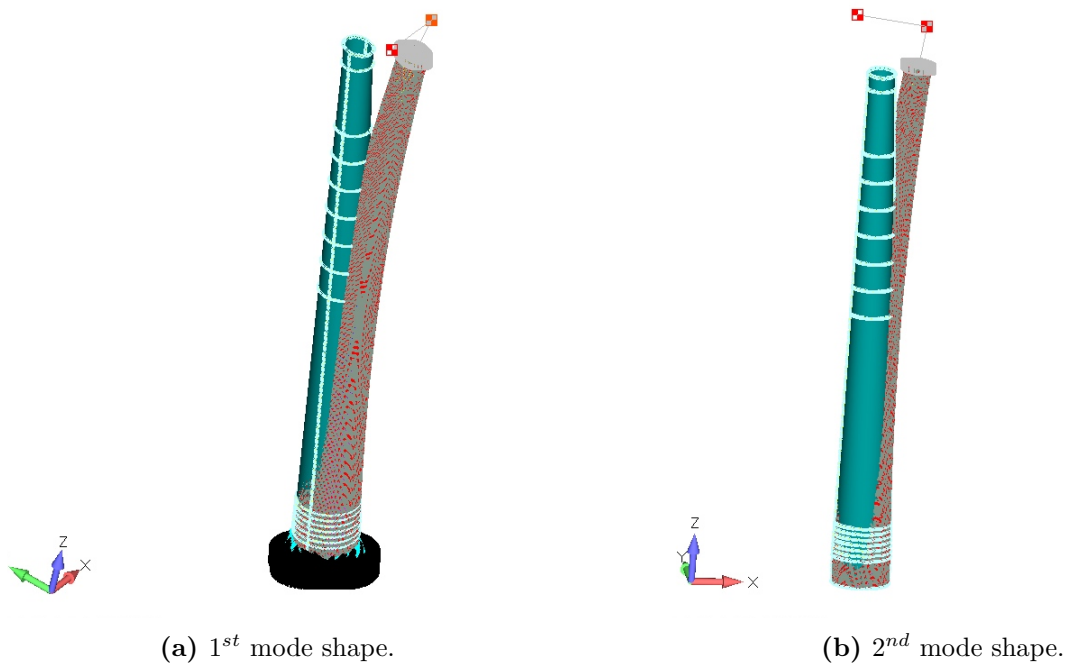
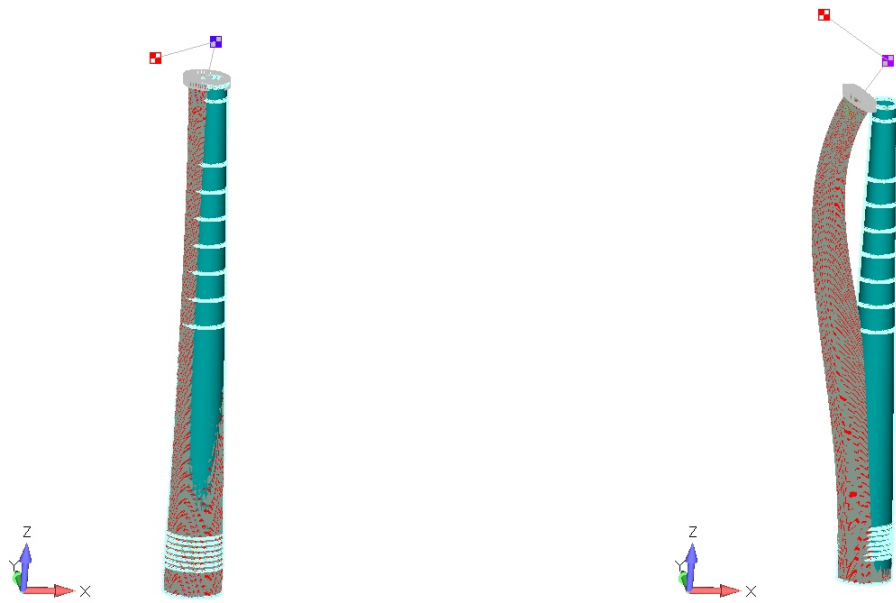


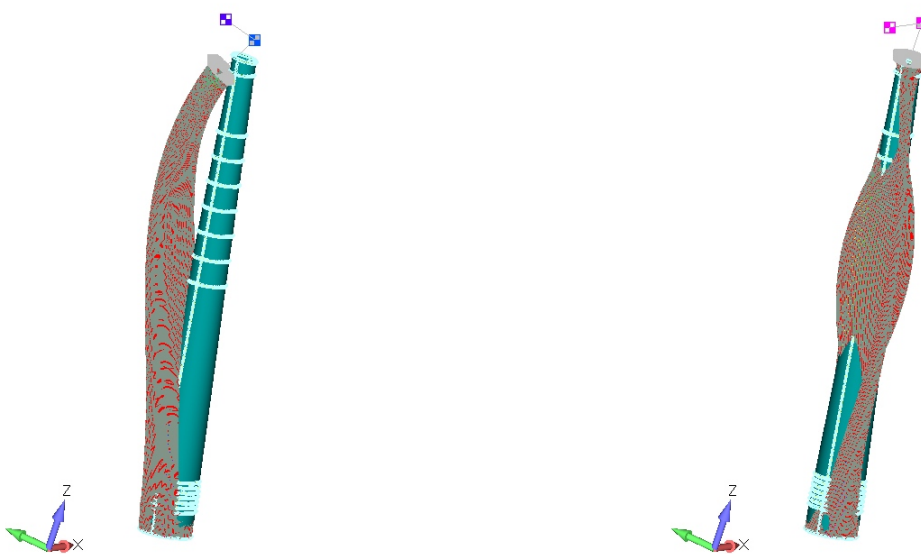
**Figure C.6:** Mode shapes the optimized FRP tower in FEMAP.



(a) 3<sup>rd</sup> mode shape.

(b) 4<sup>th</sup> mode shape.

**Figure C.7:** Mode shapes the optimized FRP tower in FEMAP.

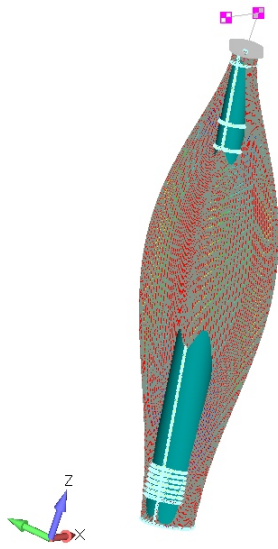


(a) 5<sup>th</sup> mode shape.

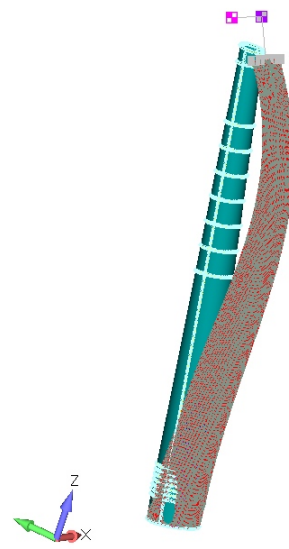
(b) 6<sup>th</sup> mode shape.

**Figure C.8:** Mode shapes the optimized FRP tower in FEMAP.

---

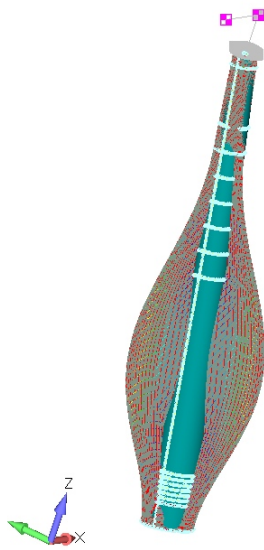


(a) 7<sup>th</sup> mode shape.

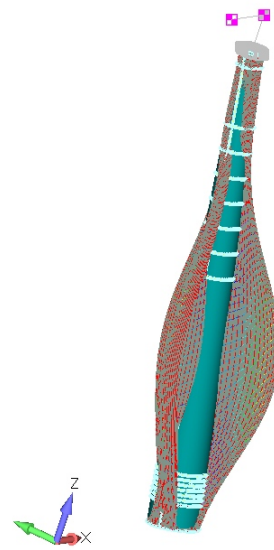


(b) 8<sup>th</sup> mode shape.

**Figure C.9:** Mode shapes the optimized FRP tower in FEMAP.



(a) 9<sup>th</sup> mode shape.



(b) 10<sup>th</sup> mode shape.

**Figure C.10:** Mode shapes the optimized FRP tower in FEMAP.